Doctoral theses at NTNU, 2021:406

Ingrid Framås Syversen

Applications of advanced MRI methods in cancer and neuroimaging

Doctoral thesis

NTNU
Norwegian University of Science and Technology
Thesis for the Degree of
Philosophiae Doctor
Faculty of Medicine and Health Sciences
Kavli Institute for Systems Neuroscience

NTNU
Norwegian University of
Science and Technology

Ingrid Framås Syversen

Applications of advanced MRI methods in cancer and neuroimaging

Thesis for the Degree of Philosophiae Doctor

Trondheim, December 2021

Norwegian University of Science and Technology
Faculty of Medicine and Health Sciences
Kavli Institute for Systems Neuroscience

NTNU
Norwegian University of
Science and Technology

NTNU
Norwegian University of Science and Technology

Thesis for the Degree of Philosophiae Doctor

Faculty of Medicine and Health Sciences
Kavli Institute for Systems Neuroscience

ISBN 978-82-326-5507-6 (printed ver.)
ISBN 978-82-326-6923-3 (electronic ver.)
ISSN 1503-8181 (printed ver.)
ISSN 2703-8084 (online ver.)

Doctoral theses at NTNU, 2021:406

Printed by NTNU Grafisk senter

Sammendrag

Anvendelser av avanserte MR-metoder i kreft- og nevroavbildning

Magnetisk resonansavbildning (MR) er en svært nyttig og allsidig ikke-invasiv medisinsk bildemodalitet. I denne oppgaven ble avanserte MR-metoder innen kreft- og nevroavbildning undersøkt. Nærmere bestemt fokuserte vi på utvikling og anvendelse av avansert diffusjonsvektet avbildning (DWI), diffusjonstensoravbildning (DTI) og funksjonell MR (fMRI) i prostatakreft og i den entorhinale korteksen i hjernen.

Prostatakreft er en av de vanligste kreftformene blant menn, og MR-avbildning er en viktig del av diagnostiseringen. Det er imidlertid fortsatt behov for bedre verktøy for å skille mellom kreftformer med høy og lav risiko. Den såkalte 'tilsynelatende' diffusjonskoeffisienten (ADC) fra konvensjonell DWI er mye brukt, men er en grov forenkling av den underliggende mikrostrukturen til vevet. I artikkel I i denne oppgaven utvikler og anvender vi derfor en ADC- og T_2-avhengig to-komponent modell basert på kombinert T_2-DWI, for å undersøke om den har potensial for diagnostikk av prostatakreft. Vi fant ut at denne modellen var i stand til å skille mellom tumor og normalt prostatavev, og viste noe korrelasjon med tumoraggressivitet. Våre funn indikerer dermed at den ADC- og T_2-avhengige to-komponentmodellen har potensial for diagnostisering og karakterisering av prostatakreft.

Den entorhinale korteksen (EC) er en del av hjernen som er involvert i kognitive prosesser som minnedannelse, romlig navigasjon og tidsoppfatning. Den kan i hovedsak deles inn i to underregioner, medial (MEC) og lateral (LEC) EC, som har både forskjellige funksjonelle egenskaper og tilkoblinger til andre hjerneregioner. Selv om MEC og LEC har blitt mye studert hos andre dyr som for eksempel rotter, vet man fortsatt ikke nøyaktig hvor disse ligger i den menneskelige hjernen. Et par tidligere fMRI-studier som undersøkte dette fant funksjonelle forskjeller mellom posteromedial (pmEC) og anterolateral (alEC) EC, men det er

usikkerhet knyttet til hvilke metoder som bør brukes for å identifisere disse underregionene hos mennesker. I artikkel II bruker vi derfor DTI og såkalt sannsynlighetsbasert traktografi for å dele inn den menneskelige EC basert på strukturelle tilkoblinger til andre hjerneområder som er kjent for å være koblet til enten MEC eller LEC. Videre, i artikkel III, hadde vi som mål å utvide denne analysen til en kohort med både DTI- og fMRI-data, for å direkte sammenligne resultatene fra å bruke strukturelle og funksjonelle koblinger for å dele inn EC. Både DTI- og fMRI-resultatene fra de to artiklene støtter opp under inndelingen av den menneskelige EC inn i pmEC og alEC, selv om det var noen små forskjeller fra tidligere studier. Korrekt lokalisering av MEC og LEC i den menneskelige hjernen har betydning for forskning innen både kognitiv nevrovitenskap og for studier på sykdommer som Alzheimers, som starter i EC-området.

Til sammen viser forskningen i denne oppgaven hvordan avansert DWI og DTI kan brukes til å modellere forskjellige typer vev. Den viser også at DTI og fMRI er i stand til å beskrive lignende tilkoblinger mellom hjerneområder. Både kreft og nevroavbildning er svært relevante fagområder for anvendelse av disse avanserte MR-metodene, som kan få økt betydning innen kreft- og demensdiagnostikk i fremtiden.

Kandidat: Ingrid Framås Syversen
Institutt: Kavliinstitutt for nevrovitenskap
Veiledere: Christian F. Doeller, Pål Erik Goa og Tobias Navarro Schröder
Finansieringskilde: Fakultet for medisin og helsevitenskap, NTNU

Ovennevnte avhandling er funnet verdig til å forsvares offentlig
for graden ph.d. i medisinsk teknologi.
Disputas finner sted digitalt onsdag 15. desember 2021, kl. 12.15.

Summary

Magnetic resonance imaging (MRI) is a powerful and versatile non-invasive medical imaging modality. In this thesis, advanced MRI methods in cancer and neuroimaging were investigated. More specifically, we focus on the development and application of advanced diffusion-weighted imaging (DWI), diffusion tensor imaging (DTI) and functional MRI (fMRI) in prostate cancer and the entorhinal cortex of the brain.

Prostate cancer is one of the most common types of cancer among men worldwide, and MRI is essential in detection and staging of the disease. However, improved tools are needed to distinguish between low-risk and high-risk cancer, and the widely used mono-exponential apparent diffusion coefficient (ADC) derived from DWI is a crude simplification of the underlying tissue microstructure. In paper I of this thesis, we therefore develop and apply an ADC- and T_2-dependent two-component model based on combined T_2-DWI, in order to investigate its diagnostic potential in prostate cancer. We found that signal fractions of a slow diffusion component estimated from this model were able to significantly discriminate between tumor and normal prostate tissue, and showed a fair correlation with tumor aggressiveness. Our findings thus indicate that the ADC- and T_2-dependent two-component model shows potential for diagnosis and characterization of prostate cancer, although it only performed similarly, and not better than more conventional diffusion models.

The entorhinal cortex (EC) is a part of the hippocampal formation of the brain involved in cognitive processes such as memory formation, spatial navigation and time perception. It can be divided into two main subregions—medial (MEC) and lateral (LEC) EC—which differ in both functional properties and connectivity to other regions, and these have been widely studied and defined in rodents. Despite previous attempts to localize the human homologues of the subregions using fMRI, where they were identified as posteromedial (pmEC) and anterolateral (alEC) EC, uncertainty remains about the choice of imaging modality and

seed regions for connectivity analysis. In paper II, we therefore use DTI and probabilistic tractography to segment the human EC based on differential connectivity to other brain regions known to project selectively to MEC or LEC. Furthermore, in paper III, we aimed to extend this analysis to a cohort with both DTI and resting-state fMRI data, in order to directly compare the results from using structural and functional connectivity to segment the EC. Both the DTI and fMRI results from the two papers support the subdivision of the human EC into pmEC and alEC, although with a larger medial-lateral component than in the previous fMRI studies. We also showed that the segmentation results using DTI are relatively reproducible across cohorts and acquisition protocols. Correctly delineating the human homologues of MEC and LEC has importance not only for research in systems and cognitive neuroscience, but also for translational studies on neurodegenerative processes such as Alzheimer's disease, which starts in the EC and transentorhinal area.

In conclusion, the research in this thesis demonstrates how advanced DWI and DTI can be used to model different types of tissue. It also shows that DTI and fMRI are able to similarly describe connectivity between brain regions. Both cancer and neuroimaging are highly relevant disciplines for applications of these advanced MRI methods, which might gain increased importance in diagnosis and management of cancer and dementia in the future.

Acknowledgements

The work in this thesis was performed at the Kavli Institute for Systems Neuroscience, the Department of Physics and also in collaboration with the MR Cancer Group at the Norwegian University of Science and Technology in the period 2018-2021.

I would like to express my gratitude to my supervisors Christian Doeller, Pål Erik Goa and Tobias Navarro Schröder for giving me the opportunity to work on these interesting projects. Thank you for your invaluable guidance, support and encouragement. My projects did not always go as planned, but you helped me find alternative solutions. I would also like to thank all my co-authors on the papers. A special thanks goes to Tone Bathen and Mattijs Elschot for their advice on the prostate cancer project, to Menno Witter for sharing his knowledge in neuroanatomy, and to Daniel Reznik for helping out with the fMRI analyses. In addition, I want to acknowledge the Digital Life prostate cancer study and the Human Connectome Project for letting me use their MRI data.

I am also grateful to have worked with such great colleagues, both in the Biophysics section and in the Doeller group. Thank you for all the interesting discussions, and fun social events and lunches. My PhD years would not have been the same without you. I have learned so much, both about science and life in general.

Last but not least, I would like to thank my friends, family and Marius for always being supportive.

Trondheim, July 2021

Ingrid Framås Syversen

List of papers

Paper I

Exploring the diagnostic potential of adding T2 dependence in diffusion-weighted MR imaging of the prostate

Ingrid Framås Syversen, Mattijs Elschot, Elise Sandsmark, Helena Bertilsson, Tone Frost Bathen, Pål Erik Goa

PLOS ONE 2021;16(5):e0252387. doi: 10.1371/journal.pone.0252387

Paper II

Structural connectivity-based segmentation of the human entorhinal cortex

Ingrid Framås Syversen, Menno P. Witter, Asgeir Kobro-Flatmoen, Pål Erik Goa, Tobias Navarro Schröder, Christian F. Doeller

As submitted to NeuroImage

Revised version published in: NeuroImage 2021;245:118723. doi: 10.1016/j.neuroimage.2021.118723

Paper III

Investigating structural and functional connectivity of human entorhinal subregions using DTI and fMRI

Ingrid Framås Syversen, Daniel Reznik, Tobias Navarro Schröder, Christian F. Doeller

Manuscript

Abbreviations

ADC Apparent diffusion coefficient

alEC Anterolateral entorhinal cortex

AP Anterior-posterior

BOLD Blood-oxygenation-level-dependent

BPH Benign prostatic hyperplasia

dCA1pSub Distal CA1 + proximal subiculum

DCE Dynamic contrast-enhanced imaging

deoxy-Hb Deoxygenated hemoglobin

DTI Diffusion tensor imaging

DWI Diffusion-weighted imaging

EC Entorhinal cortex

EPI Echo-planar imaging

FA Fractional anisotropy

fMRI Functional magnetic resonance imaging

fODF Fiber orientation distribution function

GRE Gradient-echo

ICA Independent component analysis

LEC Lateral entorhinal cortex

MEC Medial entorhinal cortex

ML Medial-lateral

MRI Magnetic resonance imaging

MTL Medial temporal lobe

OFC Orbitofrontal cortex

oxy-Hb Oxygenated hemoglobin

PA Posterior-anterior

PHC Parahippocampal cortex

PI-RADS Prostate Imaging-Reporting and Data System

pmEC Posteromedial entorhinal cortex

PRC Perirhinal cortex

PZ Peripheral zone

RF Radiofrequency

ROC Receiver operating characteristics

ROI Region of interest

rs-fMRI Resting-state functional magnetic resonance imaging

RSC Retrosplenial cortex

RSI Restriction spectrum imaging

SE Spin-echo

SNR Signal-to-noise ratio

T_2-DWI T_2- and diffusion-weighted imaging

TE Echo time

TR Repetition time

TZ Transition zone

Contents

Chapter 1

Introduction

Magnetic resonance imaging (MRI) has become an invaluable tool in medical imaging due to its versatility and non-invasiveness [1–3]. Since its invention in the 1970s [4–6], technological developments in both hardware and software have moved the boundaries for possible applications of this powerful imaging modality. Today, it is widely used for both clinical and research purposes and across a range of disciplines. This thesis will focus on applications of advanced MRI methods in cancer and neuroimaging. More specifically, we will look into prostate cancer and the entorhinal cortex of the human brain, using diffusion-weighted and functional MRI. Research in both of these fields is important in a global health perspective, as cancer and dementia are among the most common causes of death [7–9].

1.1 Magnetic resonance imaging

MRI is based on the principles of magnetic resonance of nuclear spins [1–3, 10–13]. The most frequently used nucleus in MRI is the proton, due to its abundance in biological tissue, but also other atoms with uneven mass numbers have these magnetic properties. To acquire an MR image, so-called MR sequences are performed, where different combinations of radiofrequency (RF) pulses and magnetic field gradients are applied to sample the k-space of an object. The contrast in the resulting image—which is obtained by Fourier transforming the recorded k-space—is governed by different relaxation processes and magnetic susceptibility effects, but also by more advanced mechanisms such as diffusion and blood flow. A thorough introduction to the basic principles of MRI can be found in textbooks such as [1–3].

1.1.1 Diffusion-weighted MRI

Diffusion is the random movement of molecules in a medium due to thermal energy [14]. In biological tissue, the diffusion of water molecules depends on the structure of the tissue. This water movement can be probed using diffusion-weighted imaging (DWI), enabling extraction of information about the underlying tissue microstructure and function [2, 15]. Example applications are in cancer imaging to characterize tumors, and in neuroimaging to identify white matter tracts.

In order to make an MR sequence diffusion-weighted, a pair of diffusion-sensitizing gradients can be added to a spin-echo (SE) sequence (Figure 1.1a) [3, 16]. Applying a gradient will dephase the spins, and if we then wait a certain diffusion time Δ before applying a reversed gradient to rephase the spins, some of them will have moved in the meantime due to diffusion. Because they now have a different position than during the first diffusion gradient, they will experience a different field strength, and the signal will not be perfectly refocused (Figure 1.1b-d). The presence of diffusion therefore reduces the MR signal. Thus, the more the water molecules have diffused, the lower the signal. This signal reduction is exponential and is given by

$$SI = SI_0 e^{-b \cdot ADC} \tag{1.1}$$

where SI is the measured signal intensity, SI_0 is the signal intensity in the absence of diffusion-weighting, b is the so-called b-value and ADC is the apparent diffusion coefficient. The b-value is the degree of diffusion weighting in the image, and is determined by

$$b = \gamma^2 G^2 \delta^2 \left(\Delta - \frac{\delta}{3} \right) \tag{1.2}$$

where γ is the gyromagnetic ratio of the nucleus, G is the diffusion gradient strength and δ is the duration of the gradient. The ADC of the tissue can then be determined by acquiring diffusion-weighted images at two or more b-values.

1.1.1.1 Biophysics of water diffusion in biological tissue

The diffusion of water molecules in the body is in many cases not free, but hindered or restricted by different structures and barriers in the tissue [17]. This is why the diffusion measured with DWI is not the true diffusivity of single water molecules, but rather an appar-

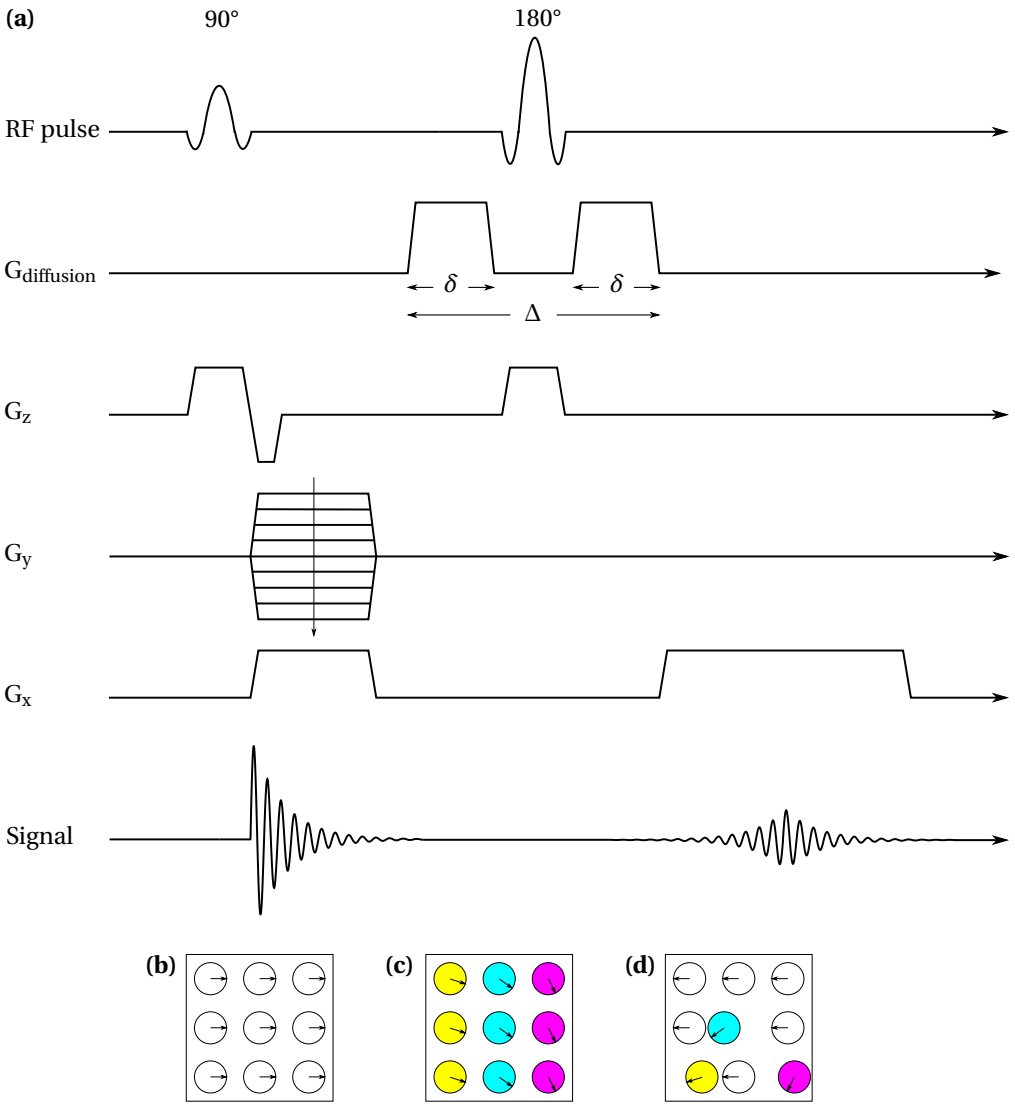

Figure 1.1: Schematic illustration of the principles of a diffusion-weighted sequence. **(a)** After excitation, two diffusion gradients ($G_{diffusion}$) are added on each side of a 180° pulse to make the spin-echo sequence sensitive to diffusion. They are each applied for a duration δ, with the time Δ between them. G_x, G_y and G_z denote the gradients applied in the x-, y- and z-direction, respectively. **(b)** All spins have the same phase immediately after excitation. **(c)** When the first diffusion gradient has been applied, the phase of the spins is dependent on their position. **(d)** The signal is rephased after the second diffusion gradient. However, if some of the spins have diffused and changed position between the gradients, they will not be perfectly rephased and the resulting signal will be lower than if there were no diffusion.

ent diffusion coefficient (ADC) of the tissue dependent on its underlying microstructure. In those cases where there are no obstacles for the water molecules and the diffusion is truly free (Figure 1.2a,d,e), the diffusion is a Gaussian process and the mean squared 3D displacement of a molecule is given by

$$\langle r^2 \rangle = 6Dt \tag{1.3}$$

where t is the time and D is the diffusivity or diffusion coefficient (unit: mm^2/s) [14]. The net displacement of the water molecules will increase linearly with time, and the measured ADC is independent of the diffusion time of the DWI sequence. However, if the water molecules are hindered by structures in the tissue such as macromolecules, fibers and cells (Figure 1.2b,d,e), the net displacement will be lower than in the free diffusion case and depends on the geometry of the obstacles. The measured ADC is also in this case independent of the diffusion time, except for very short time windows where the water molecule does not diffuse far enough to encounter any hindrances. In other cases, the diffusion might be restricted, for

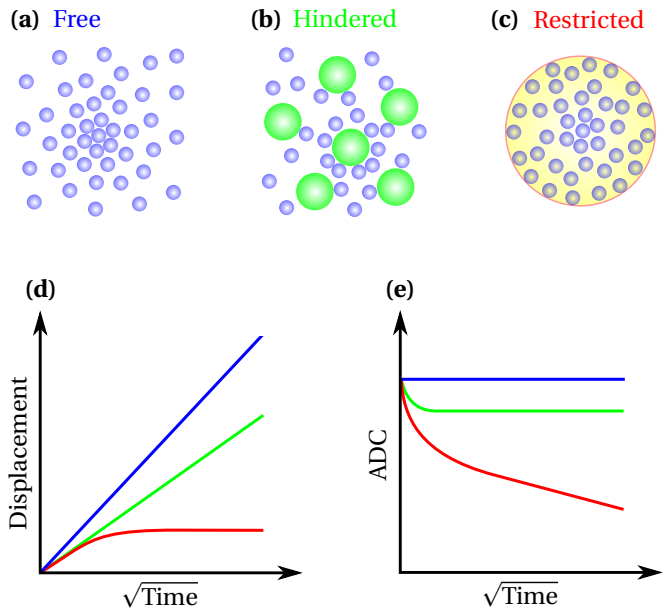

Figure 1.2: Illustration of free, hindered and restricted diffusion. **(a)** Free diffusion: Water molecules (small blue circles) diffusing freely in matter. **(b)** Hindered diffusion: The diffusion of the water molecules is hindered by different structures (green circles) in the tissue, e.g. macromolecules or fibers. **(c)** Restricted diffusion: The diffusion of water molecules inside a cell (big yellow circle) is restricted by the cell membrane. **(d)** The net displacement of a water molecule as a function of time for free (blue line), hindered (green line) and restricted (red line) diffusion. **(e)** The ADC evolution over time for free, hindered and restricted diffusion.

example if the water molecules are trapped inside a an enclosed compartment such as a cell (Figure 1.2c,d,e). This will limit the maximal possible net displacement so that it is no longer linear, and this is therefore a non-Gaussian diffusion process. Consequently, the measured ADC will decrease with increasing diffusion times [18].

Because the diffusion mechanisms of the tissue within a single voxel might be a mixture of free, hindered and restricted diffusion, more advanced diffusion models are needed to characterize this. Although Equation 1.1 often is a decent approximation when using b-values in the clinical range, the diffusion signal clearly deviates from a mono-exponential decay when using very high b-values (> 1000-1500 s/mm^2) [19]. While some of the more advanced diffusion models try to mathematically characterize this deviation, other models describe the signal as composed of several water components, each with its own mono-exponential ADC [18, 20, 21]. One example is the bi-exponential model, where the signal is modeled as coming from two separate tissue components with different signal fraction contributions: one component with slow diffusion and one component with fast diffusion [22, 23]. The "slow" component is thought to represent the restricted diffusion within cells, whereas the "fast" component represents extracellular water. Thus,

$$\frac{SI}{SI_0} = SF_{slow}\exp\big(-b\cdot ADC_{slow}\big) + SF_{fast}\exp\big(-b\cdot ADC_{fast}\big), \tag{1.4}$$

where SF_{slow} and SF_{fast} are the signal fractions of the slow and fast component, respectively, and $SF_{slow}+SF_{fast}=1$. These signal fractions have shown promise as imaging biomarkers in tumor detection and characterization [22–24]. In addition, more complex restriction spectrum imaging (RSI) models with even more diffusion components have been investigated, representing a similar multi-exponential signal decay [25–27].

1.1.1.2 Diffusion tensor imaging

In addition to being restricted to different compartments, the diffusion can also be restricted along certain directions, which can be measured using diffusion tensor imaging (DTI). This is an expansion of conventional DWI, where diffusion anisotropy—that is, diffusion with directional dependence—is exploited to trace the paths of the water molecules [3, 28, 29]. By measuring the diffusion along at least six independent directions, a diffusion tensor $\overline{D}$ can be reconstructed:

$$\overline{D} = \begin{bmatrix} D_{xx} & D_{xy} & D_{xz} \\ D_{xy} & D_{yy} & D_{yz} \\ D_{xz} & D_{yz} & D_{zz} \end{bmatrix} \tag{1.5}$$

The subscripts x, y and z denote combinations of diffusion in different directions. This diffusion tensor can then be used to for example calculating the fractional anisotropy (FA)—a scalar between 0 and 1 that describes the degree of anisotropy, where 0 means that the diffusion is completely isotropic (equal diffusion in all directions) and 1 means that the diffusion is infinitely anisotropic (diffusion in one direction only). One example of anisotropic diffusion is within the myelinated fiber tracts of the brain, where the water can diffuse more freely along the direction of the fibers than across them. By creating an FA map of the brain, it is possible to visualize this anisotropy and hence the major white matter pathways of the brain.

1.1.2 Functional MRI

Until now, we have focused on MR techniques for imaging and providing information about the anatomy and structure of the tissue. However, it is also possible to use MRI to obtain an indirect measure of brain function—so-called functional[1] MRI (fMRI) [2, 30–32]. This imaging technique is based on the principles of neurovascular coupling, which means that the blood flow and blood oxygenation in the brain are dependent on neuronal activity. It has become a valuable tool in human neuroscience research, but is also used clinically in for example neurosurgical planning [33, 34].

The crucial contrast mechanism in fMRI is the blood-oxygenation-level-dependent (BOLD) response following increased brain activity [35, 36]. Oxygen is transported in the blood attached to hemoglobin (Hb) molecules, which can be oxygenated (oxy-Hb) or deoxygenated (deoxy-Hb). While oxy-Hb is weakly diamagnetic, deoxy-Hb is strongly paramagnetic and will disturb the local magnetic field, thus decreasing the transverse relaxation times of the nearby tissue [37]. Therefore, if the level of oxy-Hb compared to deoxy-Hb changes over time, there will be signal fluctuations that can be detected with fMRI. This BOLD response following a brief stimulus can be characterized by the hemodynamic response function (Figure

[1] Note that the term "functional MRI" is sometimes also used for all other types of MRI than pure anatomical imaging, including DWI and dynamic contrast-enhanced MRI. Here, we will use "fMRI" only for BOLD functional imaging.

1.3a) [38, 39]: A transient energy demand due to neuronal activity first results in increased levels of deoxy-Hb, reducing the detected signal. Then, because of the increased need for glucose and oxygen, there will be an increase in both blood flow and blood volume in order to supply more oxy-Hb, which gives a peak in the detected BOLD signal. The signal will at last decrease to a slightly lower level than the initial signal, before it gradually rises to the baseline again. The BOLD contrast is governed by both T_2 (spin-spin relaxation) and T_2' (susceptibility-induced intravoxel dephasing) transverse relaxation, and is therefore most often detected with T_2*-weighted imaging, for example using a gradient-echo (GRE) sequence (Figure 1.3b) [3, 40]. Several image volumes are usually acquired over a period of time to measure fluctuations in the BOLD signal.

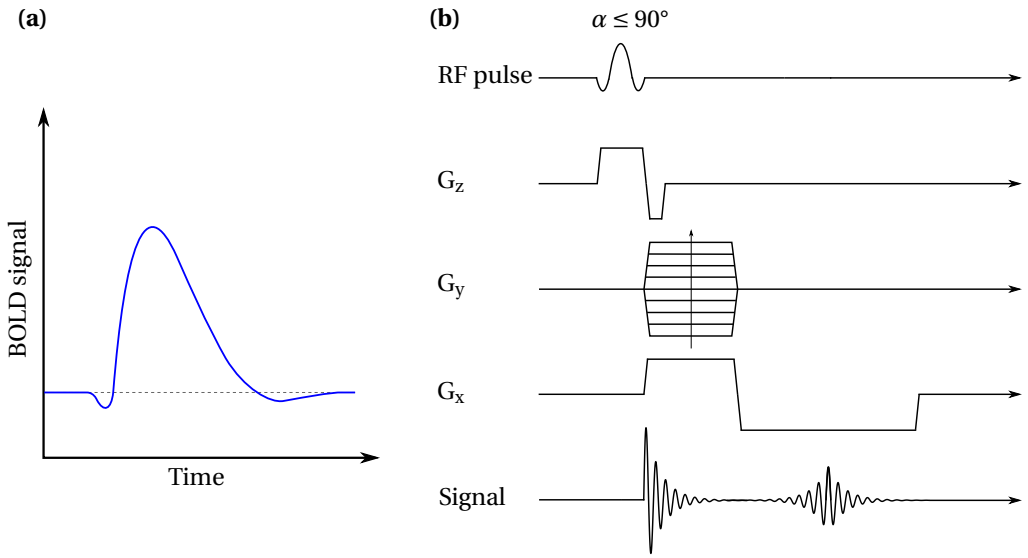

Figure 1.3: Illustration of the hemodynamic BOLD response and a gradient-echo sequence used for fMRI. **(a)** The BOLD response after a stimulus: First there is an initial dip, followed by the BOLD signal peak. At last, there is a post-stimulus undershoot before the signal gradually restores to the baseline level. **(b)** In a gradient-echo sequence, the read-out gradient G_x is reversed after the initial application in order to refocus the signal for detection.

1.1.2.1 fMRI in practice

It is important to note that fMRI only provides an indirect measure of brain activity, and that the data must be carefully acquired, preprocessed, analyzed and interpreted to get valid results. The neurovascular coupling mechanisms are still not fully quantitatively understood,

and there is not a 1:1 linear relationship between neuronal activation and BOLD response [39]. Furthermore, the BOLD signal is relatively weak, although it increases with increasing field strength [40]. Appropriate acquisition and preprocessing protocols are crucial for minimizing noise and other non-neural sources of signal variation. The actual design of the fMRI experiment and the choice of analysis approach depend on the clinical or research question in mind (see Section 1.3.2.1). It is therefore clear that expertise in fMRI methods, statistics and neuroanatomy is important to perform such investigations in order to avoid invalid conclusions. Nevertheless, fMRI activation patterns have been qualitatively confirmed by other modalities [41, 42], and it is a powerful tool when applied and interpreted correctly.

1.1.3 Echo-planar imaging

Since the contrast in DWI is based on the movement of water molecules in the tissue, it is also highly sensitive to other sources of motion [2, 43]. This also applies to fMRI, where motion can give rise to fluctuations in the signal intensity that can interfere with the underlying BOLD signal. The MR sequences for these applications should therefore be as short as possible in order to reduce the impact of motion on the acquisition. In the sequences presented so far, only one line in k-space is acquired per repetition time (TR), and the length of the acquisition therefore scales with N×TR where N is the number of k-space lines in the image (Figure 1.4b). However, there exist sequences that are able to acquire several lines in k-space after one excitation, potentially shortening the acquisition time by N-fold. One of these is echo-planar imaging (EPI), which has become the workhorse in many DWI and fMRI applications.

The reason why EPI is able to acquire an image volume in such a short time, is because it utilizes rapid switching of gradients in order to acquire several lines in k-space successively (Figure 1.4a,c) [3, 44]. To traverse the k-space, the frequency encoding or read-out gradient G_x is applied to move along k_x, while the phase encoding gradient G_y is applied to move along k_y. Thus, when applying successive reversed read-out gradients with short phase encoding gradient blips between them, the k-space is sampled in a raster-like pattern. This principle can be applied to a number of different sequences, for example an SE DWI sequence or a GRE fMRI sequence.

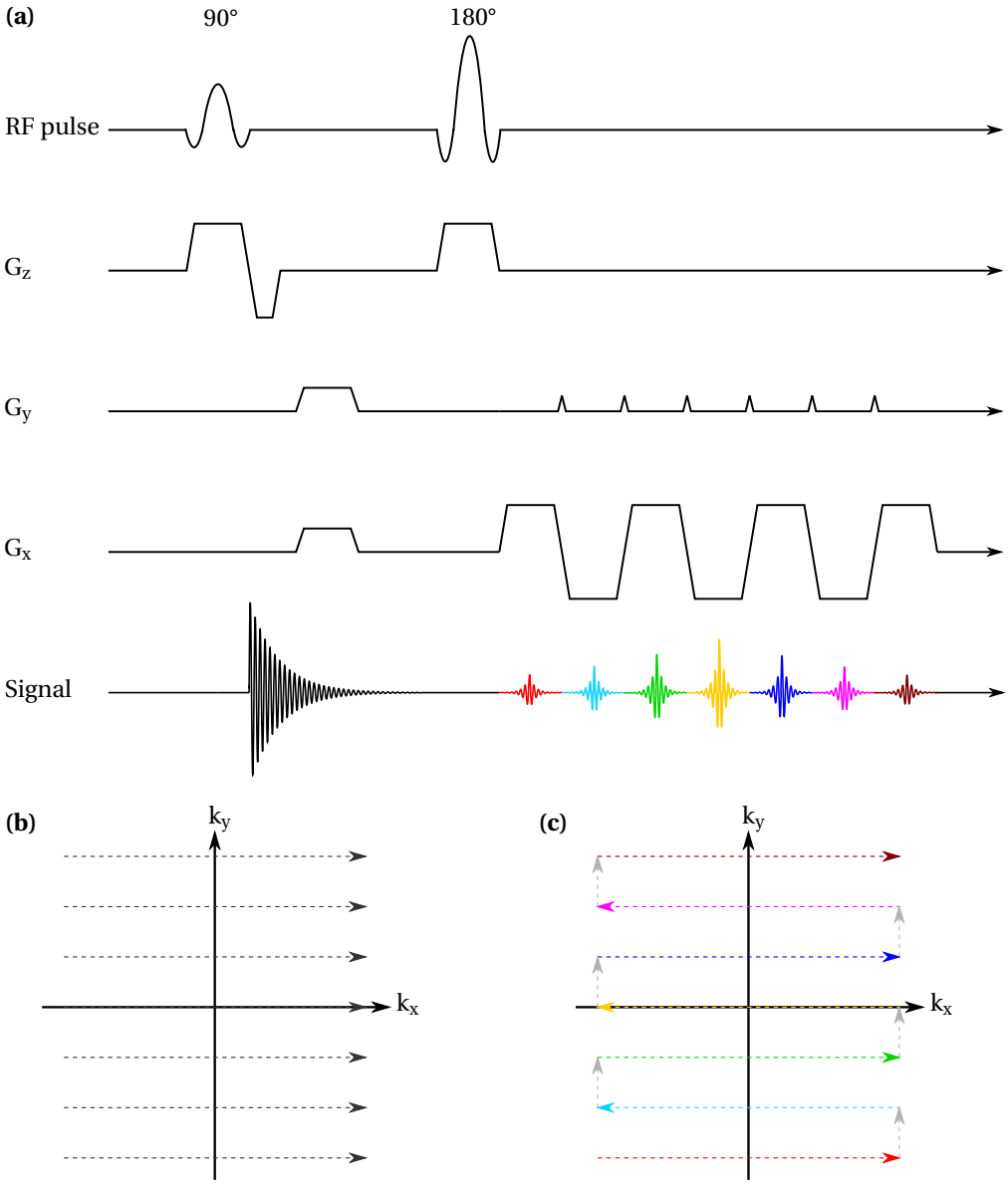

Figure 1.4: Schematic illustration of an SE-EPI sequence and k-space traversal for different types of sequences. **(a)** An EPI sequence is characterized by rapid reversals of the read-out gradient (G_x), with short phase encoding blips (G_y) in between. **(b)** In a traditional MR sequence (e.g. as shown in Figures 1.1a, 1.3b), only one line in k-space is sampled per TR. **(c)** The gradient switching in EPI enables raster-like sampling of several k-space lines per TR.

1.1.3.1 EPI artifacts

Although EPI overcomes many of the challenges related to motion during scanning, it is inherently prone to a number of other image artifacts [2]. In sequences used for DWI and fMRI, some of the most common ones are Eddy current artifacts, ghosting, geometric distortions and signal loss.

The EPI artifacts are to a large extent caused by the way the sequence traverses the k-space [3]. Because of rapid gradient switching, an additional current is introduced, which alters the net magnetic gradient. This leads to Eddy current artifacts in the images, visible as scaling, shearing and translation of voxels. For DWI, this is especially prominent due to the added diffusion gradients. These currents can also create delays causing the spins to refocus at a later stage. Combined with the fact that every other line in k-space is sampled in the reverse direction, this can lead to ghosting where structures in the image are periodically repeated. The latter two types of EPI artifacts, geometric distortions and signal loss, are related to magnetic susceptibility effects. EPI has a very low bandwidth in the phase encoding direction, meaning that the frequency difference from one voxel to the next is very small. Therefore, even small inhomogeneities in the local magnetic field will misplace the signal in the resulting image, and the resulting geometric distortion appears as stretching or compression of the imaged object in the phase encoding direction (Figure 1.5). This effect is especially prominent near boundaries between low and high susceptibility, for example air-tissue or bone-tissue interfaces. Furthermore, the susceptibility variations can cause signal loss due to intravoxel dephasing. The sensitivity to magnetic susceptibility effects generally increases with increasing field strength (due to faster T_2* dephasing) [40]. Geometric distortions often increase with increasing spatial resolution (due to the longer duration of the read-out), but on the other hand there is a trade-off because decreasing the voxel size can mitigate signal loss (due to less intravoxel dephasing) [45]. Although there exist several different acquisition, reconstruction and post-processing correction methods to mitigate these artifacts [2, 3, 46–49], they are often not perfect and the image quality is still the main limitation of EPI compared to more conventional MRI sequences.

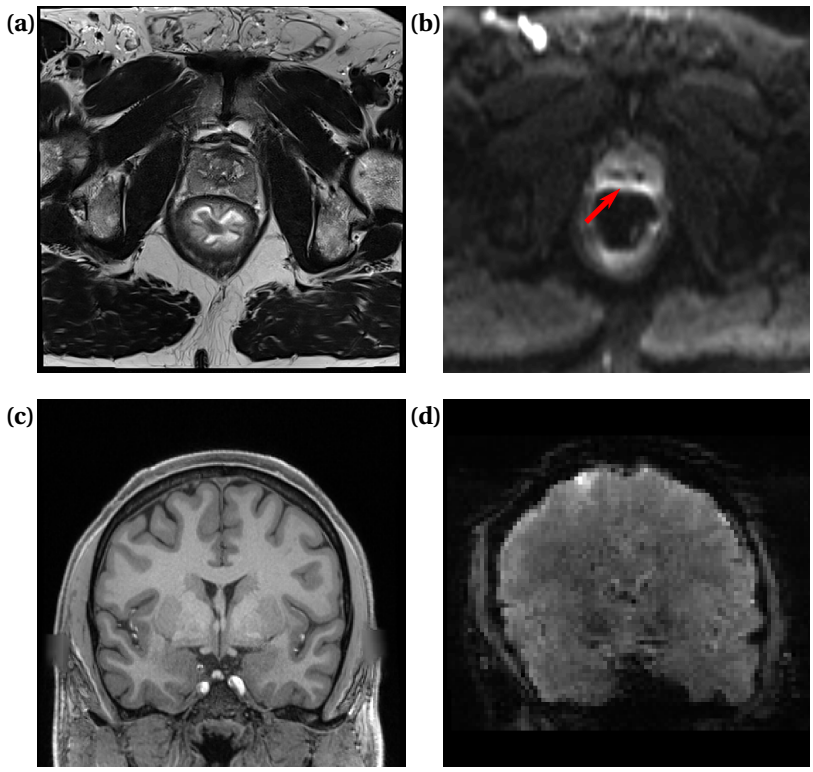

Figure 1.5: Examples of EPI artifacts. **(a)** Axial slice of a T_2-weighted and **(b)** an SE-EPI DWI image (b = 800 s/mm^2) of the prostate, with posterior-anterior (top to bottom in the image) phase encoding direction. Air in the rectum causes geometric distortions and increased signal intensity near the prostate border (red arrow). **(c)** Coronal slice of a T_1-weighted and **(b)** a GRE-EPI fMRI image of the brain, with left-right (right to left in the image) phase encoding direction. The whole brain is heavily distorted and skewed.

1.2 Cancer

Cancer is the general term for a group of diseases characterized by rapid and uncontrolled cell proliferation, and is the second leading cause of death globally [7, 50]. It is caused by genetic mutations of the cells, either arising spontaneously during cell division or caused by external factors damaging the DNA, transforming them into "immortal" cancer cells [51, 52]. The cancer cells can grow in solid tumors or be disseminated in body fluids. Furthermore, they can invade other tissues or spread to other parts of the body. There are many different types of cancer, and they are characterized both by what type of cells and from which organ they originate from. However, cancer is a very heterogeneous disease and the same type of diagnosis can have highly different outcome prognoses. There is still a need for earlier diagnosis, better risk prediction and more efficient treatments of cancer.

1.2.1 Prostate cancer

Prostate cancer is one of the most common types of cancer among men worldwide [53]. 27% of the cancer diagnoses among men in Norway are prostate cancers, and approximately one in eight men will develop prostate cancer by the age of 75 [54]. They are usually so-called adenocarcinomas, developing from the glandular cells of the prostate [55]. The prostate can be divided into four main zones (Figure 1.6)—the peripheral zone (PZ), transition zone (TZ), central zone (CZ) and anterior fibromuscular stroma (AFMS) [56]. The PZ is the largest area, and 70-80% of the cancers originate there, compared to 20-25% in the TZ and CZ [57, 58]. Prostate cancers are often slow-growing and asymptomatic at the time of diagnosis, and symptoms like pain or difficulties urinating are usually a sign that the cancer is advanced or has spread to other parts of the body [59, 60].

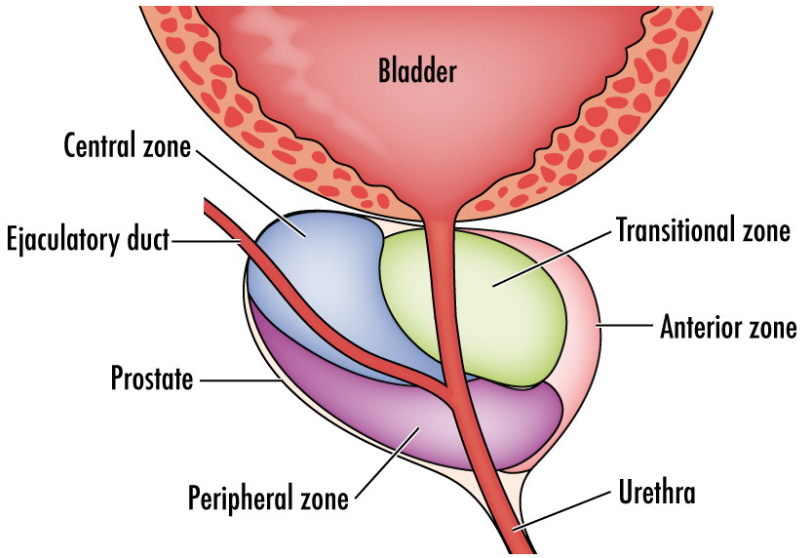

Figure 1.6: Illustration of the anatomy of the prostate (sagittal view). The prostate gland is located inferior to the bladder, and encapsulates the urethra and the ejaculatory duct. It consists of the peripheral zone (PZ, purple), transition zone (TZ, green), central zone (CZ, blue) and anterior fibromuscular stroma (AFMS, bright red/pink). Reproduced with permission from [61].

To diagnose and stage prostate cancer, a combination of clinical examination, prostate-specific antigen (PSA) measurements, imaging and biopsy is the standard in Norway [59, 60]. The biopsy is often targeted using ultrasound or MR images. The prostate cancer diagnosis is determined from the biopsy, and staged according to the Gleason grading system (Table 1.1) [62, 63]. Appropriate treatment is then decided based on the risk, together with other factors

Table 1.1: Gleason grading system for prostate cancer risk groups based on histopathological assessment. The new Gleason Grade Group system was designed to provide a better representation of the actual risk than the old Gleason scores, although both of them are often used together.

Risk group	Gleason score	Gleason Grade Group
Low (or very low)	≤ 6	1
Intermediate (favorable)	7 (3+4)	2
Intermediate (unfavorable)	7 (4+3)	3
High	8	4
Very high	9-10	5

such as the age, health condition and the personal preferences of the patient. Available treatment types include prostatectomy, radiotherapy, chemotherapy, hormone treatment and active surveillance. However, it can be difficult to determine the tumor aggressiveness and optimal treatment accurately, and both over- and undertreatment remain a major challenge in prostate cancer management [64, 65].

1.2.2 MRI in prostate cancer

MRI is often performed before a biopsy when there is suspicion of prostate cancer, in order to detect and characterize possible lesions and determine the locations of targeted biopsies [59, 60, 66, 67]. Such a diagnostic protocol usually consists of T_2-weighted imaging and DWI (Figure 1.7), and sometimes also dynamic contrast-enhanced imaging (DCE), according to the Prostate Imaging-Reporting and Data System (PI-RADS) [68]. This set of standardized guidelines assists the radiologist in predicting the probability that a cancer is clinically sig-

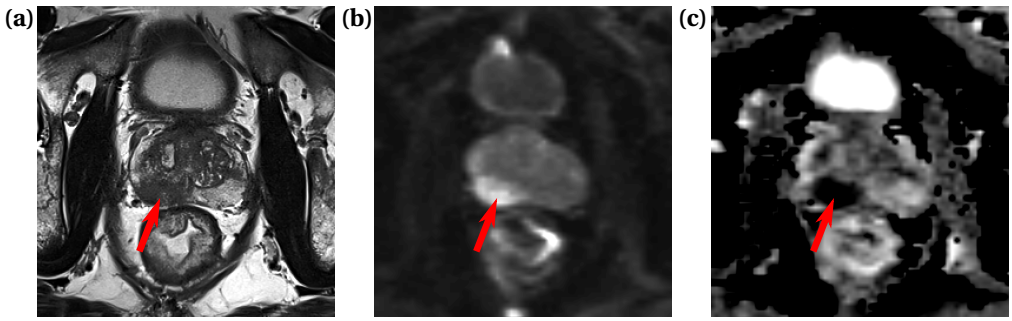

Figure 1.7: Examples of MR images used for prostate cancer diagnostics. Axial view of a **(a)** T_2-weighted image, **(b)** DWI image (b = 800 s/mm^2) and **(c)** ADC map of the prostate. The red arrows denote a PZ lesion scored as PI-RADS 5.

Table 1.2: PI-RADS scores for radiological assessment of the likelihood of clinically significant prostate cancer. The score is determined using a combination of T_2-weighted imaging, DWI and DCE.

Likelihood of clinically significant cancer	**PI-RADS score**
Very low	1
Low	2
Intermediate	3
High	4
Very high	5

nificant (Table 1.2). While DWI is the dominant factor for determining the PI-RADS score for PZ cancers, T_2-weighted imaging is predominantly used for cancers in the TZ, and in certain cases DCE is used for support.

1.2.2.1 DWI and mono-exponential ADC

Prostate cancer is often visible on diffusion-weighed images as focal areas with high signal intensity, with correspondingly low mono-exponential ADC ($\leq$ 1000 $\mu m^2/s$) [68]. The low ADC is commonly interpreted as abnormally restricted diffusion due to densely packed cancer cells in the tumor [69, 70]. To create these ADC maps, DWI is usually performed along three orthogonal directions at two different b-values. The so-called trace-weighted images—that is, the geometric mean of the images from the three directions—are then used to calculate the mono-exponential ADC (Equation 1.1) [3].

However, although DWI and ADC maps generally perform well at detecting prostate cancer, there are some limitations to the method. Firstly, even though ADCs have been shown to correlate with histopathological Gleason scores, there is considerable overlap between risk groups [70, 71]. The accuracy of distinguishing between low-risk and high-risk cancer is variable, which can make it challenging to select the appropriate treatment [72–74]. Benign prostatic hyperplasia (BPH) also shows a low ADC and can in some cases be mistaken as malignant [75]. Furthermore, the actual ADCs calculated depend on the sequence parameters and vary between sites and vendors, making it difficult to use standardized ADC thresholds [76]. Another important limitation is that the mono-exponential ADC model is an over-simplification that does not correctly represent the heterogeneity of the underlying tissue microstructure [77]. Although tumors have densely packed cancer cells, they can also have concomitant edema and necrosis with increased ADC, which can disguise the reduced

ADC from the restricted water within the cells [78, 79]. A bi-exponential model or RSI might therefore be better approximations of this heterogeneous tissue diffusion and have shown promise in prostate cancer characterization [22, 23, 27]. However, the tissue components of these models in reality have additional dependencies to those described in Equation 1.4.

1.2.2.2 ADC- and T_2-dependent two-component model

In addition to different ADCs, tissue components can also have different T_2-values. These can be modeled similarly to the ADC components using bi-exponential modeling on images with different echo times (TEs), although it is unclear whether the identified components have a one-to-one correspondence where the same subpopulations of water molecules are isolated by the ADC vs. T_2 bi-exponential models [77, 80]. Traditionally, ADCs and T_2 values have been assumed to be independent of each other, but previous work suggests an interdependence of these values in biological tissue [81, 82]. What has been known, however, is the T_2 shine-through effect, characterized by hyperintense signal in DWI caused by tissue with long T_2. In clinical imaging, this is usually considered an inconvenience that is attempted to be eliminated [83]. Nevertheless, this principle could in theory be used to actively tune the diffusion signal from the water molecules based on their T_2 values, but this has not been widely explored. In DWI there is a trade-off when it comes to the TE used in the sequence: while a shorter TE yields more signal and less T_2 shine-through, a longer TE has also been shown to provide a better tumor conspicuity [84]. By varying the TE of the sequence, signal from diffusion components with distinct T_2 values can potentially be isolated.

In the prostate, the interdependence between T_2 and ADC has been shown to be different for tumor, normal tissue and BPH [84–86]. This relationship could potentially be exploited for prostate cancer diagnosis. By performing DWI using a set of different b-values and TEs, it would in theory be possible to isolate the signal from subvoxel populations of water molecules with specific paired T_2 values and ADCs associated with different components of the prostate tissue. This combined T_2- and diffusion-weighted imaging (T_2-DWI) approach provides a matrix of signal values for each voxel that can be used for model fitting. A three-component model using this imaging technique has been suggested, with the purpose of distinguishing the prostate tissue components epithelium, stroma and lumen [87]. However, during clinical diagnostic imaging protocols, a relatively short acquisition time is crucial. Also, very complex models might be too computationally demanding in a clinical

setting. A model with only two components might therefore be easier to implement in the diagnostic pathway. The components are similar to those in the ADC-based bi-exponential model, with a fast component representing water in the glandular lumen with long T_2 and a high ADC, and a slow component representing water inside the cells with a shorter T_2 and lower ADC (Figure 1.8). This two-component model is obtained by adding TE dependence to Equation 1.4, so that the signal fractions are also dependent on the exponential T_2 decay:

$$\frac{SI}{SI_0} = SF_{slow} \exp\left(-\frac{TE}{T_{2,slow}}\right) \exp\left(-b \cdot ADC_{slow}\right) + SF_{fast} \exp\left(-\frac{TE}{T_{2,fast}}\right) \exp\left(-b \cdot ADC_{fast}\right). \tag{1.6}$$

(a) "Slow" component:
→ Low ADC
→ Short T_2

(b) "Fast" component:
→ High ADC
→ Long T_2

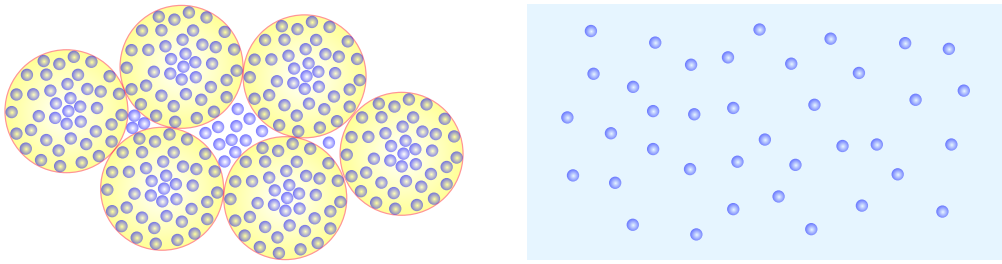

Figure 1.8: Illustration of the slow and fast diffusion components of the ADC- and T_2-dependent two-component model. **(a)** While the slow component represents water molecules restricted by cell membranes, **(b)** the fast component represents water in the glandular lumen.

1.3 Neuroimaging

Neuroimaging is the art of imaging the anatomy or the function of the brain [33, 88]. There exist a variety of different techniques used to image the brain either directly or indirectly, for example MRI, computed tomography (CT), positron emission tomography (PET), single-photon emission computed tomography (SPECT), magnetoencephalography (MEG) and electroencephalography (EEG). They can be used in clinical diagnostics or disease management for head trauma, stroke, brain tumors and neurodegenerative diseases, among others, and advanced methods are also used for neurosurgical planning. Another important application of neuroimaging is in research.

1.3.1 Neuroscience research

In neuroscience, the goal is to study and understand the structure and function of the nervous system, where the brain is the most central organ [89]. It is made up of billions of neurons, which are highly interconnected to operate this highly complex network. The cerebrum of the brain is separated into two hemispheres that can be subdivided into four main lobes (Figure 1.9). Each hemisphere has an outer layer of gray matter—the cerebral cortex—which mainly consists of neuronal cell bodies, and an inner core of white matter, which mainly consists of bundles of myelinated axons—so-called fiber 'tracts' that enable communication between brain regions.

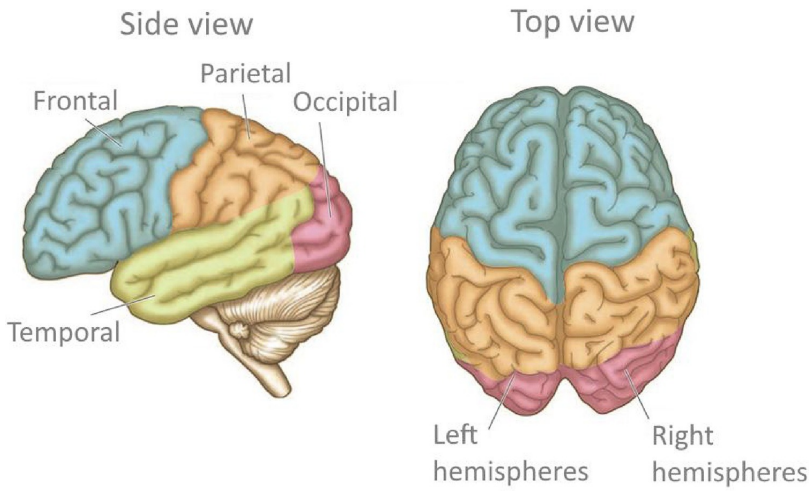

Figure 1.9: Illustration of brain lobes and hemispheres of the cerebrum. The frontal, parietal, occipital and temporal lobes are shown from a side view (left), and the left and right hemispheres are shown from a top view (right). Reproduced with permission from [90].

Neuroscience research is a highly interdisciplinary field and can be categorized into several different subdisciplines, although they also often tend to merge together. Some examples are systems neuroscience, which studies the structure and function of neural circuits and systems [91]; cognitive neuroscience, which studies how cognitive functions are produced by neural circuity [92]; and translational neuroscience, where neuroscience is translated and applied for development of clinical applications and treatments for nervous system disorders [93]. There is a wide variety of methods and approaches that can be used to investigate the brain [88, 89]. While a lot of the current knowledge in neuroscience has been obtained through basic research in animals [94], for example in rodents and non-human primates,

human neuroscience research is more limited by ethical constraints on invasive procedures. Therefore, neuroimaging has become the essential tool to investigate the human brain *in vivo*. However, even though the increasing sophistication of available methods have enhanced our understanding of this enormously complex organ, there are still many unanswered questions.

1.3.1.1 Entorhinal cortex

The entorhinal cortex (EC) is a part of the hippocampal formation located in the medial temporal lobe (MTL) of the brain (Figure 1.10). It is central in episodic memory encoding, spatial navigation and time perception [95–99], and it processes and relays information between the neocortex and the hippocampus [100–102]. The EC can be divided into two main subregions, 'medial' (MEC) and 'lateral' (LEC) entorhinal cortex, which differ in both functional properties and connectivity to other regions [103–105]. Roughly speaking, the MEC mainly supports allocentric processing of space [106–109], while LEC mainly supports processing of objects and time [98, 108, 110, 111], although this traditional view is to some degree a simplification [112, 113]. Both the location and the function of the MEC and LEC have been identified and widely studied in rodents and non-human primates. However, the human homologues of these regions and their exact locations have not been studied at the same level of detail. Although there have been previous fMRI studies which suggest that the homologue subregions are located posteromedially (pmEC) and anterolaterally (alEC) in the EC, respectively [114, 115], it remains unclear whether the results could be affected by the nature of the imaging modality or the choice of brain regions used to identify the MEC and LEC homologues—particularly in light of new findings from rodents which have substantially revised the classical model of EC connectivity [112]. Identifying these subregions is important for functional and cognitive studies of the EC and also for research on neurodegenerative diseases such as Alzheimer's, which is the most common form of dementia and originates in the EC and transentorhinal area [8, 116, 117].

1.3.2 MRI in neuroscience

MRI has become an essential tool in human neuroscience research, due to its non-invasiveness, versatility and superior soft tissue contrast [88, 89, 119]. Depending on the type of research, MRI studies can include scanning of both patients and/or healthy volunteer participants.

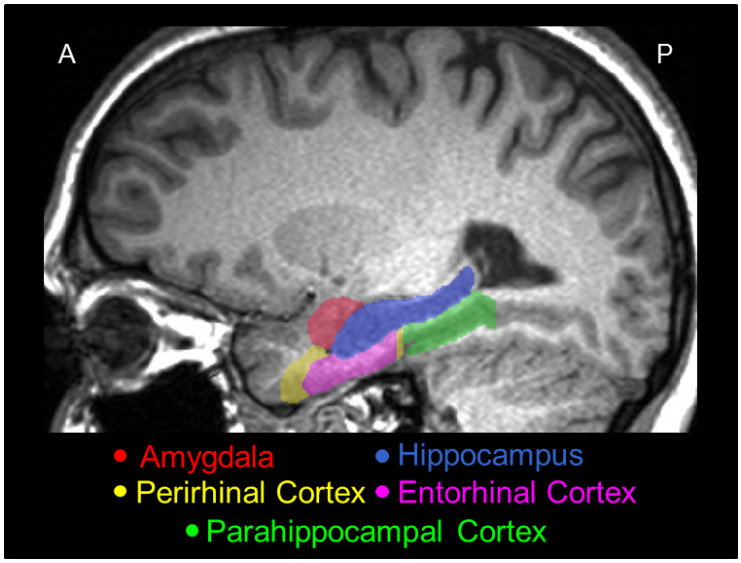

Figure 1.10: Sagittal slice of a structural MR image showing the medial temporal lobe, with delineations of the entorhinal cortex (pink), hippocampus (blue), perirhinal cortex (yellow), parahippocampal cortex (green) and amygdala (red). A = anterior, P = posterior. Reproduced with permission from [118].

There are several types of MRI that are frequently used to investigate the brain, ranging from "standard" structural imaging to more advanced functional and modeling approaches, often also in combination. The actual choice of methods will depend on the particular research question in mind. Following the recent years' rapid development in both hardware and computational power, a new world of possibilities have opened up, enabling novel MRI methods and neuroscientific advances that were previously inaccessible.

1.3.2.1 fMRI and functional connectivity

One of the most widely used types of MRI in neuroscience is functional MRI [120, 121]. As explained in Section 1.1.2, fMRI exploits the fluctuation in BOLD signal over time in order to indirectly measure brain activity. There are several possible investigation approaches available. For example, in task-based fMRI, the participants undergo various tasks in order to detect the locations and patterns of brain activity during the task. The nature of such a task can range from simple visual stimuli to highly complex navigation and memory paradigms, seeking to identify which brain regions are involved in certain cognitive processes and how they are involved. In resting-state fMRI (rs-fMRI), on the other hand, the participants do not perform any tasks, but are instead scanned at rest over a period of time with a BOLD-

sensitive sequence. While various forms of data- and process-related modeling approaches are often used in task-based fMRI, most rs-fMRI analyses are considered model-free or data-driven.

Resting-state fMRI can be used to investigate functional connectivity, i.e. to identify brain regions and networks that share functional properties [121, 122]. This is done by quantifying temporal correlations of voxels and regions in the brain, assuming that functionally connected regions show correlated activity. The BOLD signal in these resting-state networks is characterized by low-frequency variations over time [123]. However, it is important to preprocess, analyze and interpret the rs-fMRI data carefully, because signal fluctuations can arise from other sources than the BOLD response. It is especially important to mitigate and be aware of scanner noise and physiological sources of noise such as heart rate, respiration and head motion. Appropriate preprocessing of the data is therefore crucial. It is also important to be aware of practical considerations of the actual data acquisition, such as participant instructions (e.g. "think about nothing"; eyes closed vs. eyes open, fixation), acquisition length, and temporal and spatial resolution [122, 124]. Then, for the functional connectivity analysis itself, various methods can be used. One example is independent component analysis (ICA), a data-driven approach where mathematical algorithms are used to decompose the signal into separate frequency components that are statistically independent of each other [121, 122]. Another example is seed-based analysis, where a region of interest (ROI) is defined and the temporal correlation between this ROI and the rest of the voxels in the brain is calculated (Figure 1.11). Although this approach requires an a priori hypothesis on which seed regions to investigate, it is a relatively simple and powerful method to detect functionally connected regions. Previous work has shown that seed-based analysis and ICA yield similar functional connectivity networks [122].

Despite the growing interest in rs-fMRI over the years, it has not been without controversy [124]. There have been questions about the sources of the resting-state fluctuations, negative correlations, and whether correlation really implies connectivity. Direct measures using implanted electrodes and calcium imaging in monkeys and mice have, however, confirmed that these low-frequency BOLD fluctuations correspond to actual neuronal activity [125, 126]. Furthermore, functional connectivity estimates have been shown to be stable across studies, although reliability and reproducibility vary [122]. A number of resting-state

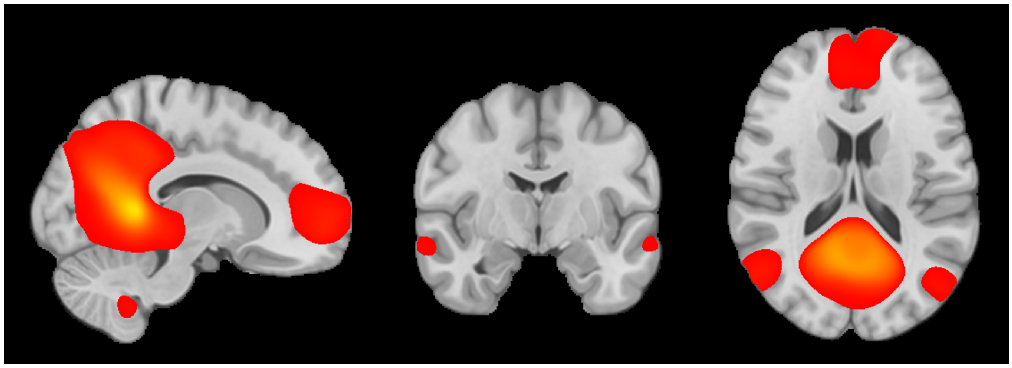

Figure 1.11: Example of a functional connectivity map overlaid on a structural MR image, obtained by using a retrosplenial cortex ROI (bright yellow area) as seed in temporal correlation analysis of rs-fMRI data. The resulting functionally connected areas, denoted by the red-yellow color map, are part of the so-called default mode network.

networks have been identified, such as the default mode network, salience network, auditory network, visual network, sensorimotor network and dorsal attention network, among others [121]. However, one limitation of these functional connectivity measures is that they do not provide information about directionality or causality of the connections, in addition to that there might be dynamic changes in functional connectivity over time [40, 127]. Also, note that while functional connectivity indicates that the brain regions are involved in the same functional processes, and function generally is constrained by anatomy, it does not necessarily mean that the regions are *directly* connected with brain fibers [122, 127]. Alternative methods are needed in order to examine such direct anatomical connections. Nevertheless, rs-fMRI is a robust and useful method for characterizing large-scale brain systems, which can be obtained relatively fast and easy.

1.3.2.2 DTI and structural connectivity

Another important imaging modality in neuroscience is diffusion tensor imaging (DTI) [129]. As mentioned in Section 1.1.1.2, FA maps can be used to visualize the major white matter pathways of the brain (Figure 1.12a). However, in order to reconstruct the fiber tracts in a more detailed manner and investigate structural connectivity between specific brain regions, so-called tractography can be performed [129–131]. For this purpose, a minimum of 30-60 unique diffusion directions should be acquired to reduce the uncertainty in the estimated fiber directions. There exist two main groups of approaches: deterministic and

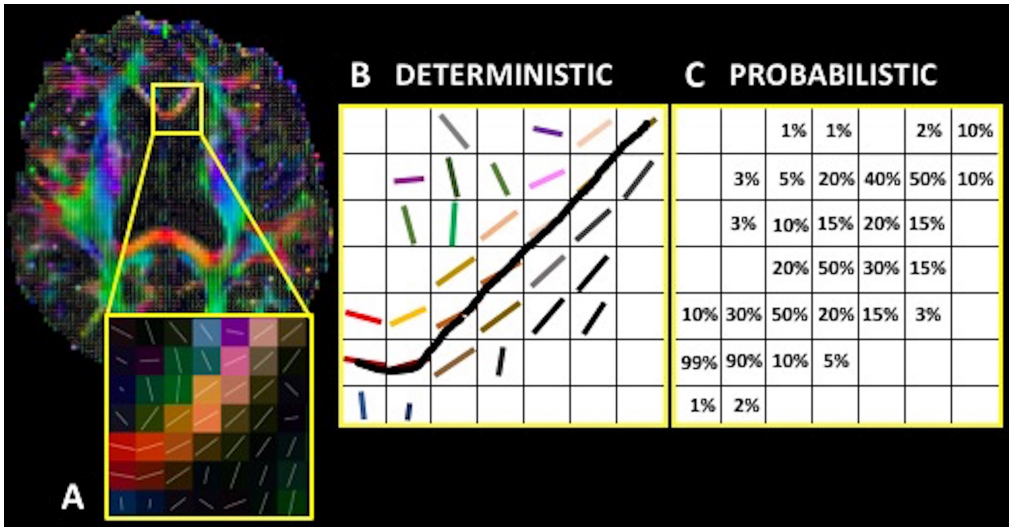

Figure 1.12: Deterministic vs. probabilistic tractography approaches. **(a)** Color-coded FA map obtained from DTI, showing the degree and direction of the diffusion anisotropy. Red color denotes principal diffusion direction left↔right, green denotes anterior↔posterior, and blue denotes superior↔inferior. **(b)** In deterministic tractography, only one single fiber direction is represented per voxel, and the modeled tracts follow these principal directions. **(c)** In probabilistic tractography, connectivity paths are generated based on a probability distribution of diffusion directions for each voxel. Reproduced with permission from [128].

probabilistic tractography. In deterministic tractography, single tracts are reconstructed by following the principal direction of the diffusion tensor from voxel to voxel (Figures 1.12b, 1.13a). However, this is a "winner takes all" approach where only one fiber direction is considered per voxel, and it does not take into account that each voxel can contain fibers dispersed in several different directions. Probabilistic tractography, on the other hand, handles this by estimating a fiber orientation distribution function (fODF) with several possible path directions for each voxel [132–135].

The fODFs for probabilistic tractography can be modeled in several different ways. One widely used is the "ball and stick" model, where the diffusion signal is split into isotropic components (multi-shell "balls" with different diffusivities), and infinitely anisotropic components for each fiber orientation ("sticks") [132, 133]. Another approach is the "ball and zeppelin" model, which is slightly different, but still models the diffusion signal as separate isotropic and anisotropic components [135]. In both these types of models, the signal S within a voxel when applying the k^{th} diffusion gradient is a weighted sum of attenuated sig-

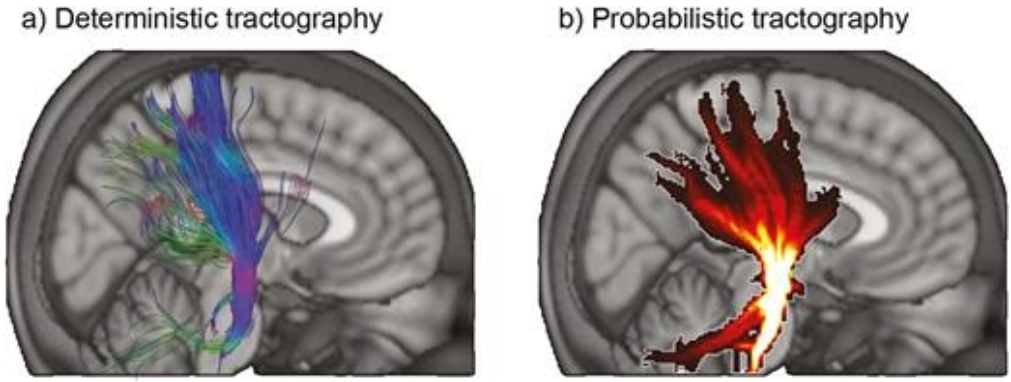

Figure 1.13: Structural connectivity path representations from deterministic vs. probabilistic tractography. **(a)** In deterministic tractography, single tracts are reconstructed. **(b)** The connectivity paths in probabilistic tractography are represented as a probability map of the existence of a tract in each voxel (brighter color means higher probability). Reproduced with permission from [136].

nal fractions f from the isotropic partial volume component E^{PV} and the anisotropic component E^{AN}:

$$S(\theta_k,\phi_k)/S_0 = S_k/S_0 = (1-f_{AN})E_k^{PV} + f_{AN}E_k^{AN}, \tag{1.7}$$

where θ and ϕ denote the angles of the diffusion gradient direction, S_0 is the non-diffusion-weighted signal, and $0 \leq f_{AN} \leq 1$. The underlying idea is then that the measured anisotropic diffusion signal S^{AN} can be considered as the spherical convolution of the fODF F and an impulse response function R:

$$S^{AN}(\theta,\phi) = F(\theta,\phi) \otimes R(\theta,\phi). \tag{1.8}$$

The main difference between the "ball and stick" and "ball and zeppelin" models is that the latter gives a width to the deconvolution kernel when determining the fODF. This can suppress false positive fiber crossings, and also performs better at detecting crossing fibers in areas of low anisotropy.

After estimating voxel-wise fODFs for the whole brain, structural connectivity paths are created by drawing a sample from the fODF and following that direction to the next voxel [132, 133]. This is performed iteratively in order to build up a probability map of the paths, which

instead of depicting single tracts provides a confidence measure of the existence of a tract in that voxel (Figures 1.12c, 1.13b). The advantage of this approach over deterministic tractography is the possibility to model smaller tracts and crossing fibers. However, it is still important to interpret the results carefully, as there is currently no 'gold standard' for validating human tractography results. Estimated connection probabilities also depend on factors such as paths lengths and seed ROI sizes, and do not provide any information about the directions of projections. Nevertheless, DTI tractography is a powerful tool and currently the best alternative for *in vivo* comparison of structural connectivity with functional connectivity measures from fMRI.

Chapter 2

Aims of the thesis

The overall aim of this thesis was to apply advanced MRI methods to research areas in cancer and neuroscience. More specifically, the key goal was to develop and investigate DWI and fMRI methods in prostate cancer and the entorhinal cortex of the brain.

The main objectives of the research presented in this thesis were:

1. To develop and investigate the diagnostic potential of an ADC- and T_2-dependent two-component model in prostate cancer, based on combined T_2-DWI (Paper I).

2. To use DTI and probabilistic tractography to investigate structural connectivity between the EC and associated brain regions, in order to identify human homologues of MEC and LEC based on differential connectivity following new insights from rodent anatomy (Paper II).

3. To investigate reproducibility of DTI results in the EC, and to use both DTI and fMRI to compare structural and functional connectivity between the EC and associated regions, in order to identify human homologues of MEC and LEC based on differential combined connectivity (Paper III).

Chapter 3

Summary of papers

3.1 Paper I

Exploring the diagnostic potential of adding T2 dependence in diffusion-weighted MR imaging of the prostate

The purpose of this paper was to investigate the diagnostic potential of signal fractions estimated from an ADC- and T_2-dependent two-component model using combined T_2- and diffusion-weighted imaging (T_2-DWI).

76 patients, of which 62 had post-MRI biopsy-confirmed prostate cancer and 14 with BPH, underwent combined T_2-DWI at 3T following prostate cancer suspicion. The acquisition protocol consisted of two TEs of 55 and 73 ms and two b-values of 50 and 700 s/mm^2, providing a set of four measurements per voxel. The patients were split into a training and test set, and the data from the training set were used to globally optimize the T_2 values of the slow and fast components of the two-component model. Literature ADCs of 0.3 and 2.6 μm^2/ms were used throughout the analyses for the slow and fast components, respectively. The resulting fixed T_2 values and ADCs of the components were then used to estimate the signal fraction of the slow component for the test set patients in tumor, BPH and normal tissue ROIs. For comparison, the slow component of a pure ADC-dependent bi-exponential model was also calculated, in addition to the mono-exponential ADC.

The optimal T_2 values for the two-component model were found to be 45 and 180 ms for the slow and fast components, respectively. All three analyzed models showed a signifi-

cant difference between PZ tumors and normal tissue, while no significant differences were found between non-PZ tumors and BPH. Receiver operating characteristics (ROC) analysis also showed a very good diagnostic performance of all models in separating between tumor and normal tissue voxels, although the two-component model yielded slightly higher sensitivity, specificity and area under the ROC curve than the two other models. Spearman correlation between calculated tumor values and Gleason Grade Group for all three models was fair, but not significant. However, the bi-exponential model and mono-exponential ADC showed slightly higher correlations than the two-component model.

In conclusion, signal fraction estimates from an ADC- and T_2-dependent two-component model based on combined T_2-DWI can differentiate between tumor and normal prostate tissue, and show potential for prostate cancer diagnosis. The model performed similarly to conventional diffusion models.

3.2 Paper II

Structural connectivity-based segmentation of the human entorhinal cortex

The goal of this paper was to use DTI and probabilistic tractography to segment the EC into the human homologues of MEC and LEC. For years, the accepted model of EC connectivity was centered around the idea of two dual streams of information via MEC and LEC and the parahippocampal and perirhinal cortices, respectively, but new insights from rodent anatomy has led to revisions of this traditional view. Furthermore, previous attempts to identify the subregions were based on fMRI.

Structural and diffusion MRI data from 35 healthy adults were obtained from the MGH-USC Human Connectome Project. DTI data were acquired at 3T with b-values of 0, 1000, 3000, 5000 and 10,000 s/mm^2. ROIs of the EC, presubiculum, distal CA1 + proximal subiculum (dCA1pSub), retrosplenial cortex (RSC) and posterolateral orbitofrontal cortex (OFC) were obtained using automated cortical parcellation. Probabilistic tractography was run between the EC and the other ROIs in order to create maps of connectivity. These structural connectivity maps were then used to segment the EC into the MEC and LEC homologues, by performing voxel-wise hard segmentation based on which other ROI show the

strongest connectivity with that voxel. MEC was defined as being more strongly connected with presubiculum and RSC, whereas LEC was defined as being more strongly connected with dCA1pSub and OFC. The resulting degree of posterior-anterior (PA) and medial-lateral (ML) orientation of the border between the EC subregions was calculated as a percentage between 0 and 100%, depending on the angle between the center of gravity vectors from MEC to LEC and a pure PA or ML vector.

All ROIs showed clear structural connectivity paths to the EC, where presubiculum and RSC were more strongly connected with medial and posterior EC, while dCA1pSub and OFC were more strongly connected with lateral and anterior EC. Using EC connectivity with different combinations of other ROIs all showed a segmentation into posteromedial (pmEC) and anterolateral (alEC) EC, such that the border between them was oriented both towards the PA and ML axes. Different seed ROIs resulted in varying degrees of PA and ML orientation of the border between the subregions, with a larger variation along the ML than PA axis. However, all DTI segmentation approaches showed a higher degree of ML orientation of the border and a correspondingly lower degree of PA orientation than previous fMRI studies attempting to subdivide the EC.

In conclusion, the DTI results from this paper support the subdivision of the human MEC and LEC homologues into pmEC and alEC, in line with previous fMRI studies. However, there are some differences between the results from the different modalities and seed regions regarding the degree of orientation of the subregion border along the PA and ML axes.

3.3 Paper III

Investigating structural and functional connectivity of human entorhinal subregions using DTI and fMRI

The main purpose of this paper was to investigate and compare structural and functional connectivity between the EC and associated brain regions, and use this to predict the locations of the human homologues of MEC and LEC. Furthermore, we also wanted to investigate the reproducibility of segmentation results obtained from the previous DTI study.

Structural, diffusion and functional MRI data from 103 healthy adults were obtained from the WU-Minn Human Connectome Project. 3T and 7T data were acquired with b-values of 0, 1000, 2000, 3000 s/mm^2 and 0, 1000, 2000 s/mm^2, respectively. 7T resting-state fMRI data were acquired in runs of 16 minutes, separately with posterior-anterior and anterior-posterior phase encoding directions. The same ROIs were used as in paper II, and the MEC and LEC connectivity definitions were also the same. Probabilistic tractography was run on the DTI data to create EC maps of structural connectivity with the other ROIs, and seed-based functional connectivity analysis was run on the rs-fMRI data to create EC maps of functional connectivity for with other ROIs. MEC and LEC homologue segmentation was performed separately for the modalities using different combinations of seed ROIs, and both with separate and combined field strength (for DTI) and phase encoding direction (for fMRI). The degree of PA and ML subdivision was calculated for all the different segmentation approaches. Resulting MEC and LEC ROIs from the DTI analysis were then used as seeds for functional connectivity analysis, and resulting MEC and LEC ROIs from the rs-fMRI analysis were used as seeds for tractography.

Structural and functional connectivity maps showed similar patterns of connectivity with the other ROIs within the EC. While presubiculum and RSC were more strongly connected with posterior and medial EC, dCA1pSub and OFC were more strongly connected with anterior and lateral EC. Using DTI and rs-fMRI to segment the EC subregions resulted in similar locations of the MEC and LEC homologues, namely posteromedial and anterolateral EC, respectively. The modalities also yielded similar orientations of the subregion border along the PA axis, but had a larger variation along the ML axis. The DTI-based segmentation results were similar to the previous DTI study. Furthermore, tractography and functional connectivity analyses performed on MEC and LEC homologues defined from the opposite modality showed differential, but similar functional and structural connectivity patterns.

In conclusion, both DTI and fMRI subdivide the human EC into pmEC and alEC, although with slight differences along the PA and ML axes. The resulting EC subregions show differential connectivity to other brain regions, but the structural and functional connectivity patterns are similar. Segmentation results from using DTI were found to be relatively reproducible across studies.

Chapter 4

Discussion

4.1 Main findings

4.1.1 Paper I

ADC + T_2-dependent two-component model has potential for prostate cancer diagnosis

The aim of paper I was to develop and investigate the diagnostic potential of the ADC- and T_2-dependent two-component model, and we showed that the signal fraction of the slow component of the model was able to significantly discriminate between tumor and normal prostate tissue. Furthermore, the signal fraction had a fair correlation with tumor aggressiveness, although not significant. However, when we compared it with the bi-exponential model and mono-exponential ADC, all three performed similarly. Our two-component model thus shows promise for prostate cancer diagnosis, but does not at this stage show notable benefits over the conventional models.

Although all three compared models performed similarly, the bi-exponential model and mono-exponential ADC showed almost equal numerical results throughout the analyses, whereas the two-component model showed slightly different results than the two others. An emerging question is therefore: Does the added T_2 dependence of the two-component model provide more or other information about the underlying tissue microstructure than the conventional models? While the mono-exponential ADC only represents the mean diffusion of the tissue, both the bi-exponential and the two-component models represent a slow and a fast diffusion component—intracellular and extracellular water, respectively. Because both these models used the same ADCs of the components in these analyses, a plausible inter-

pretation is that the added T_2 dependence of the components in the two-component model would further tune and "filter" the diffusion signal of the components. While a high b-value will attenuate water with high ADC and thus emphasize the signal from the component with low ADC (which is also characterized by short T_2), a longer TE will on the contrary emphasize the signal with a longer T_2 (which is also characterized by higher ADC). If the slow components of the two models truly represent exclusively intracellular water, this would mean that the slow component of the two-component model represents a sub-population of water molecules compared to the slow component of the bi-exponential model. However, this is still a simplification and it is more likely that the components represent mixtures of water populations. Neither the intracellular nor the extracellular water have the exact same ADC and T_2 values throughout the whole prostate. When comparing the ADCs and T_2 values from the two-component model with values calculated for a similar three-component model representing the prostate tissue components epithelium, stroma and lumen [87], our slow component appears to be approximately equivalent to the epithelium, while our fast component might be a mixture of stroma and lumen.

4.1.2 Papers II & III

Both DTI and fMRI subdivide the human EC into posteromedial and anterolateral parts

The main aims of paper II and III were to use DTI and rs-fMRI to predict the locations of the human homologues of MEC and LEC following new insights from rodent anatomy, and our results from both modalities suggest that these are located posteromedially (pmEC) and anterolaterally (alEC) in the EC, respectively. This is in line with the findings from previous fMRI studies [114, 115]. Although there were slight quantitative differences between our structural and functional connectivity-based results in how the border between the subregions was oriented, they showed qualitatively similar patterns of connectivity within the EC. The resulting subregions also showed differential patterns of connections to the rest of the brain that were similar across structural and functional connectivity. Furthermore, comparing the results from the two papers showed that the DTI results were relatively reproducible across different acquisition protocols and cohorts of participants. For the fMRI results, however, we cannot make any claims about reproducibility as different seed regions were investigated across studies, although the resulting pmEC and alEC locations were qualitatively similar.

In addition to predicting the locations of pmEC and alEC, it would also be interesting to describe the nature of the border between them—i.e. if there is a sharp or more gradient-like border. While there is a very sharp, cytoarchitectonically and projection-defined border between MEC and LEC in rodents, the non-human primate EC is suggested to have a topographical connectivity gradient along a rostrolateral to caudomedial axis which does not adhere to any distinct cytoarchitectonic division [137–139]. One might therefore assume that also the human EC has such a gradient along the anterolateral to posteromedial axis. The reason for this difference between rodents and primates might be that primates integrate together the information processed in the MEC and LEC to a larger extent—combining aspects of space, object and time processing—although this is just speculation. Other relevant factors could be that rodents have poorer vision that primates, and their prefrontal cortex is also smaller and less differentiated [140, 141]. Although we provide a probability map of the confidence of MEC and LEC homologue locations in paper III which shows a gradual "transition" between the two subregions, this should not be directly interpreted as an actual gradient between them, and defining this was out of the scope of our work. Future studies should address this question by investigating both structural and functional connectivity to even more brain regions in detail, in order to map the topography of connections that might project only to subparts of MEC and LEC.

4.2 Methodological considerations

4.2.1 Paper I

We chose to develop and apply a two-component model to the data acquired from combined T_2-DWI. A simpler approach for this type of data would be to merely calculate the change in ADC and T_2 as a function of changing TE and b-value, respectively. Some of the previous studies using combined T_2-DWI primarily investigated this, and found that there were differences in how these changed in tumor, BPH and normal prostate tissue [84–86]. More specifically, there appears to be a natural pattern in how these values behave that is somehow disrupted in tumors. This is in line with our results from supplementary analyses in the paper, at least for PZ tumors. On the other hand, we could have moved in the opposite direction and applied a more complex model. In our study, however, we were limited by the amount of data available for model fitting, with only 2×2 measurements per voxel. Further-

more, our goal with this paper was to investigate a model which might be a more accurate representation of the tissue microstructure than the mono-exponential ADC and include T_2 dependence, but still simple enough to be feasible in a clinical setting. The total acquisition time of the combined T_2-DWI protocol was just above 3 minutes, which is in the same order of magnitude as a clinical DWI scan. In comparison, acquisition times for RSI or a combined T_2-DWI scan with 3×3 measurements can be in the range from 5 to 15 minutes [27, 84, 87].

Because of limitations in the available data points compared to the number of free variables of the two-component model, we adapted the ADCs of the components from a bi-exponential model [21]. These were then used to globally optimize the T_2 values of the components. Ideally, with a larger number of data points, we would globally optimize the ADCs and T_2 values together, in order to find the values that would best fit our data and represent two optimal ADC- and T_2-dependent components of the prostate tissue. Although we already represent two components with ADCs and T_2 values of 0.3 μm^2/ms and 45 ms and 2.6 μm^2/ms and 180 ms, respectively, these might not be the optimal components for our specific research question, and the residuals of the model fitting could possibly have been reduced with more specifically optimized ADCs and T_2 values. As we hypothesize our slow component to be restricted water within tumor cells, the optimal ADC and T_2 value for this component should be closely matched with the actual physical values of these cells, in order for our two-component model to be maximally sensitive to them.

The limitation in available data points is also the most important limitation of the paper. However, as already mentioned, there is a trade-off between the amount of data and clinical feasibility. One possible workaround could be to acquire a wide range of TEs and b-values for research purposes, and then use all this data to optimize the ADCs and T_2 values of the two components. This will give the opportunity to find values that are specifically optimized for the ADC- and T_2-dependent two-component model, and the improved fitting stability provided by the additional data will increase the confidence of these values. The optimized ADCs and T_2 values could then be applied to the two-component model in a clinical setting. Choosing the appropriate b-values and TEs of the clinical sequence will also be important for maximizing the sensitivity to the ADCs and T_2 values of the components, and b-values higher than those used in our current T_2-DWI protocol might be needed. Although the clinical T_2-DWI acquisition would again be limited by the number of data points, the gained

accuracy from the optimized parameter values might weigh up for the possible loss in fitting quality. This approach would allow for an improved evaluation of the diagnostic potential of the two-component model, which would be interesting especially in terms of any potential for predicting tumor aggressiveness.

One possible source of bias in our paper was that the diffusion times of the acquisition also varied with TE. For TE = 55 ms, δ = 11.6 ms and Δ = 23.9 ms, while for TE = 73 ms, δ = 20.6 ms and Δ = 32.9 ms. This was an unfortunate effect of using two separate standard vendor DWI sequences for acquisition of the two TEs, and the mitigation for this would be to use a designated combined T_2-DWI sequence with fixed δ and Δ. However, this raises an important question: How much of the observed signal behavior depends on variation in TE, and how much is because of varying diffusion times? While the TE tunes the signal according to the T_2 of the tissue, the Δ can directly affect the measured ADC, especially in cases where the time scale corresponds with the length scale of microstructures in the tissue. In one of the previous combined T_2-DWI studies in prostate cancer, they also report varying Δ with TE, but they do not explicitly investigate the effect of this [84]. Another important question is: What is the shortest Δ that can be used to detect the restricted diffusion within the cancer cells? If Δ is too short, most of the water molecules do not interact with the cell membrane, and the measured diffusion will not appear restricted. One study investigated the effect of varying Δ for constant b-values in a glioma xenograft model in mice, and found that the water molecules started approaching this truly restricted diffusion regime at Δ = 40 ms [18]. However, this is highly dependent on the type of cells and their size and intracellular diffusivity. Other studies performing advanced diffusion modeling in the prostate have reported using Δ in the range 25-78 ms [22, 27, 84]—although many studies do not report it at all. Future studies should more rigorously investigate the differential effects of varying both TE and Δ in combined ADC- and T_2-dependent diffusion models.

4.2.2 Papers II & III

We chose to use probabilistic tractography for examination of DTI structural connectivity, as seeding the tractography from the EC to the other ROIs would then create probability maps of connectivity. Another possible approach is deterministic tractography. However, this would only allow for the mapping of one possible tract per seed voxel in the EC ROI, thus not providing the same broad distribution of paths. A great benefit of probabilistic tractogra-

phy is that this technique is able to detect also smaller, splitting and crossing paths because more than one fiber direction is possible per voxel, and it is more robust in the presence of noise—in deterministic tractography it can be difficult to move past a noisy voxel. On the contrary, any erroneous paths will tend to disperse quickly due to the probabilistic nature of the method. The confidence of the paths estimated will increase with the number of sampled paths per seed voxel. We did not perform a rigorous investigation on what number of samples would be required to get robust results, but rather chose a relatively high number of 250,000, which is considerably higher than a selection of other tractography-based segmentation studies which used 5,000-100,000 samples [142–145]. Both the estimation of the whole-brain fODFs and running the tractography with such a high number of samples were highly time-consuming processes, but this was mitigated by eventually running the computations on a graphics processing unit (GPU) [146, 147].

In this work, we used three different DTI datasets with different acquisition parameters and properties. For paper II, DTI data were acquired on a customized 3T scanner with very high gradient performance (maximum gradient strength 300 mT/m), enabling an ultra-high maximum b-value of 10,000 s/mm^2 (256 directions) [148, 149]. A high gradient strength is essential to achieve such high b-values in practice without too much T_2 signal loss caused by long TEs, and it has also been shown to increase detection of complex fiber structures at constant b-value. Furthermore, the ability to reliably resolve more than one fiber direction in each voxel is strongly dependent on the number of gradient directions—as many as 84-112 might be needed for this, dependent on the b-value [150]—and to detect three fiber orientations, the b-value should not be lower than 3000 s/mm^2 [133]. The spatial resolution of this dataset was 1.5 mm isotropic. The DTI data in paper III were acquired on scanners with lower gradient performance—although still better than most conventional scanners—with a maximum gradient strength of 100 mT/m and 70 mT/m for 3T and 7T, respectively [151]. The b-values were also lower than in paper II, but with a higher spatial resolution: At 3T, maximum b-value was 3000 s/mm^2 (90 directions × 2) with 1.25 mm isotropic resolution, while at 7T, maximum b-value was 2000 s/mm^2 (65 directions × 2) with 1.05 mm isotropic resolution. These datasets acquired at the two field strengths therefore have slightly different properties. The 3T data have a higher maximum b-value and angular resolution, and thus have a higher ability to resolve crossing fibers. On the other hand, the 7T data have a higher spatial resolution which is less prone to partial volume effects. Using both of these in com-

bination could therefore potentially provide more information about the underlying white matter microstructure. Although we performed tractography for the field strengths separately and then merged the connectivity maps for the final analyses, there also exist frameworks for data fusion where the DTI analysis is performed on the joint dataset, in order to fully exploit the benefits of their complementary features [135]. The field strength in itself is also an important difference between the two datasets. Although 7T has a higher baseline signal-to-noise ratio (SNR) than 3T, the T_2 is shorter at 7T, so with the relatively long TEs used in DTI together with a smaller voxel size most of the SNR benefit from the increase in field strength is lost. In addition, the SE-EPI sequences used for DTI is vulnerable to B_1^+ transmit inhomogeneities at 7T leading to signal and contrast variations across the brain. This signal reduction is especially prominent for the MTL, and for the DTI data in paper III we actually found the SNR measures in the EC to be lower for 7T than for 3T. All in all, the DTI datasets used across the two papers have different strengths and weaknesses. The 3T DTI dataset used in paper II has a higher maximum b-value, gradient strength and number of gradient directions. The DTI data used in paper III, on the other hand, have a higher spatial resolution and also a considerably higher sample size. Nevertheless, all three DTI datasets are of very high quality, and showed similar results for the MEC and LEC segmentation.

For the rs-fMRI analyses, seed-based functional connectivity analysis was performed. This was considered to be the suitable approach as we wanted to investigate the structural connectivity seeded from pre-defined ROIs, and it is relatively straightforward to implement. There exist other, more complex analysis methods and models to investigate resting-state structural connectivity, e.g. ICA, graph theory or the so-called ConGrads approach [115, 121, 152]. However, performing a more complex analysis does not necessarily mean that the results will be better, and both ICA and seed-based analysis have been shown to detect similar resting-state networks [122]. An important point is also that we wanted the functional connectivity analysis to resemble the principles of the DTI structural connectivity analysis in order to enable inter-modality comparisons between seed ROIs, and the seed-based approach was therefore an appropriate choice.

Because both the DTI and rs-fMRI data were acquired using EPI sequences, reduced image quality and artifacts is a limitation to this work. The MTL is generally a difficult area to image using EPI, and this is especially pronounced for fMRI, where gradient-echo EPI

sequences are normally used [153, 154]. The EC is particularly prone to artifacts such as geometric distortions and signal dropout due to its spatial proximity to air cavities. There are several possible mitigations for these problems, but unfortunately the images acquired in the Human Connectome Project were not specifically optimized for the MTL. However, the data were already distortion corrected in the preprocessing pipeline, although this is not able to recover all the signal loss. The data quality is therefore the major limitation of our rs-fMRI analyses. Among sequence parameters that can be tuned to optimize image quality in the EC are phase encoding direction, TE, TR, various acquisition acceleration techniques, spatial resolution, shimming, bandwidth, and also the choice of head coil [45, 155–159]. Unfortunately, tweaking the parameters to improve one aspect of the data quality can enhance other artifacts. To increase SNR and sensitivity to the BOLD signal, field strength can be increased from 3T to 7T, although this will also increase the amount of geometric distortions and signal loss. The participants investigated in paper III actually had both 3T and 7T rs-fMRI data available, but we chose to use only the 7T data because the SNR and functional connectivity measures of the EC in the 3T data were not sufficient for our research question. The 7T rs-fMRI data were acquired in runs with both PA and AP phase encoding, and they showed almost opposite patterns of signal loss and SNR reductions in anterior and posterior parts of the EC, respectively. We chose to average the final functional connectivity analyses across both phase encoding directions to try to even out these effects.

Susceptibility-related artifacts are an issue also for DTI data, but not as bad as for fMRI since spin-echo EPI sequences are normally used. Could a possible mitigation for severe signal loss and artifacts in fMRI of the MTL therefore be to replace the gradient-echo sequence with spin-echo? At first thought this might seem counter-intuitive, as the BOLD effect leads to increased intravoxel dephasing that is usually detected with T_2*-weighted imaging, and one would think that using SE sequences will also then compromise the BOLD sensitivity. This is partly true, but there are two sides to this story, as briefly touched upon in Section 1.1.2. The BOLD contrast is governed by two mechanisms of transverse relaxation—both T_2' and T_2 [40, 160–162]. The T_2' intravoxel dephasing effect is most prominent near larger vessels, and increases linearly with increasing field strength. However, there is also a T_2 effect due to diffusion of spins through microgradients caused by the deoxy-Hb-induced local susceptibility inhomogeneities. This mechanism is most prominent near capillaries, resulting in a T_2-weighted BOLD contrast that is more localized to tissue than to larger veins. Further-

more, this effect is proportional to the square of the magnetic field strength, so that while the T_2' and T_2 effects are comparable at 3T, the T_2 effect is actually dominant at 7T. At ultra-high field strengths, it might therefore be beneficial to use SE sequences to isolate and exploit this effect [163, 164]. This is basically like a micro-"diffusion-weighted" fMRI sequence—only without external diffusion gradients, because the local susceptibility inhomogeneities act as small intrinsic diffusion gradients! The resulting potential increase in functional spatial resolution could be particularly beneficial for characterization of the EC subregions. However, such an approach is not without challenges, which is one of the reasons that SE fMRI is not widely used today [165]. Firstly, the challenges with B_1^+ inhomogeneities of SE sequences at 7T would have to be addressed [166]. Secondly, introducing the 180° RF pulse would also increase the specific absorption rates (SAR). One way to mitigate the SAR deposition could be to reduce the flip angles or to adjust and reduce the slice package to only image the MTL and the hippocampal formation, and then to only investigate local functional connectivity. This would be helpful to improve the temporal resolution as well, because SE requires longer TEs and thus longer TRs, so that some kind of acquisition acceleration approach might be needed [167]. Nevertheless, despite its challenges, 7T SE-EPI would be an interesting approach for improving fMRI data quality in the EC.

For delineation of ROIs used for the connectivity analyses, we used automated cortical parcellation. This was first and foremost because with the high total number of participants it would have been an extremely time-consuming task to do manual delineation of all ROIs. Also, it would require anatomical skills beyond the level of an MRI physicist, although there exist protocols to guide such manual segmentations [168]. The number of participants included in this work would probably then have been much lower, compromising the statistical power of the results. However, when defining the ROIs in MNI space, some of them were manually adjusted if needed. All ROIs were also masked by ROIs from the individual participants' automated parcellation in order to increase anatomical accuracy. Nevertheless, even though the segmentations from FreeSurfer have been found to be relatively reliable [169], there is still some uncertainty associated with these ROI placements. This would primarily be problematic for the DTI analyses, where paths are seeded on a voxel-by-voxel level. Although it is unlikely that the probabilistic tractography would detect a significant number of white matter tracts in e.g. air voxels, voxels might be classified as the wrong cortical region. For example, we cannot rule out that some of the edge voxels in the EC ROIs for some

of the participants might also contain parts of the adjacent parahippocampal and perirhinal cortices. Small inaccuracies in the ROIs could also in theory affect the fMRI analyses, but is less problematic because of the spatial smoothing of the data and averaging across seed ROIs before the functional connectivity estimation. At last, the fact that some of the ROIs were located relatively close to each other could have introduced a bias to parts of the connectivity results. In tractography, the connectivity probability is dependent on the length of the paths, among others. We set a minimum path length of 5 mm to prevent "false" short-range connections, although the apparent connectivity between EC and presubiculum and dCA1pSub would still be stronger than between EC and RSC and OFC. For rs-fMRI, spatial autocorrelation could be a problem when the ROIs are located very close to each other. This is difficult to prevent when using presubiculum and dCA1pSub to define the EC subregions, but this is the reason we also chose to use RSC and OFC for comparison. The two different pairs of seed ROIs yielded qualitatively similar results although there were some quantitative differences in the degree of PA and ML orientation of the border between the subregions. A combination of these pairs of ROIs was therefore used for the final segmentations.

We developed a novel method for estimating the "degree" of posterior-anterior (PA) and medial-lateral (ML) orientation of the border between the MEC and LEC segmentations. Because our segmentation results appeared be qualitatively more ML subdivided than the previous fMRI studies, we wanted to somehow quantify the difference in subdivision along the PA and ML axes. This was determined by first calculating the center of gravity of the MEC and LEC, and the vector between these centers of gravity. Then, the angle between this vector and a pure PA or ML vector was calculated. The degree of PA and ML orientation of the border was then defined from 0 to 100%, such that an angle of 0° corresponds to a 100% PA or ML orientation, whereas an angle of 90° corresponds to 0% (i.e. perpendicular to that axis). Although this method could yield imprecise results if the shapes of the segmentations were very irregular, the calculated degrees of PA and ML orientation of the borders generally showed good agreement with the visual appearance of the segmentations. An alternative method could have been to split the EC into posterior/anterior and medial/lateral halves and calculate the percentage overlap between these and the MEC and LEC segmentations, but we think that our approach provides a better representation of how the subregions are oriented in space with respect to each other.

4.3 General discussion

4.3.1 Advanced diffusion models in prostate cancer

Applying advanced diffusion models to DWI of prostate cancer is an interesting field of research which is both scientifically and clinically relevant. Because of the non-invasiveness of MRI, the potential of imaging the microstructure is intriguing and might be an alternative to biopsies in the future—or at least to more confidently determine whether a biopsy is necessary. Beyond the traditional mono-exponential ADC, the bi-exponential and RSI models have received most attention, in addition to alternatives such as diffusion kurtosis imaging [22, 23, 170, 171]. For example in RSI, a range of different number of components have been investigated, with different signal components arising from e.g. intracellular restricted water, hindered diffusion in extracellular extravascular space, free diffusion of water, and pseudo-diffusional flow effects, among others [27]. Although these only depend on ADCs and not on T_2 values, they have shown promising results in studies. However, many of these also have the "problem" of long acquisition times and data-intensive analyses. When already investigating advanced diffusion models at this complexity level, T_2 dependence and other possible dependencies should therefore be considered as well.

As already mentioned, increasing the number of TEs and b-values acquired could be a way to strengthen the ADC- and T_2-dependent two-component model, as the behavior of ADCs and T_2 values as a function of TE and b-value might be non-linear, but these additional data points can also be used to extend the model. In our two-component model, we assume that the prostate tissue can be represented with only two components: one component with low ADC and short T_2, and one component with high ADC and long T_2. However, previous studies suggest that there is also a fraction of the signal that has low ADC and relatively long T_2 in prostate tumors [84, 85]. This might reflect extracellular water that is restricted by densely packed cancer cells, or water inside cell nuclei. As tumor cells have an elevated nuclear signal fraction compared to healthy cells [172], isolating the signal with low ADC and relatively long T_2 might be an interesting approach to combined T_2-DWI. This could be done by extending the two-component model with a nuclear signal fraction using different ADCs and T_2 values for the nucleus and the cytosol [173]. Another approach that is comparable to RSI is to increase the number of components identified with combined T_2-DWI-based models, even beyond the previously investigated three-component model [87]. In one study where

they examined a range of different numbers of RSI components they found that four components gave the best model fit, and a similar comparison could be carried out using ADC- and T_2-dependent multi-component models. Either way, using T_2-dependence in diffusion modeling of the prostate is an approach that might provide additional information about the underlying tissue microstructure, and further investigation is warranted.

Although applying more and more complex models for cancer diagnosis is intriguing, many of these face challenges when it comes to clinical feasibility because of extensive acquisition times and data-intensive analyses. However, this does not mean that we should stop developing and investigating such models. They contribute to our understanding of tissue microstructure and cancer biology, and how these relate to the MRI parameters. This gained information can then be extracted to optimize and create simplified clinically relevant protocols for cancer diagnosis. Also, in the future, technical advances in hardware and software might enable widespread direct clinical application of these advanced models.

4.3.2 Structural and functional connectivity of the brain

An important question when investigating DTI and rs-fMRI together is how structural and functional connectivity correlate with each other, and whether they can be directly compared at all. Both the acquisition and analysis principles of the two approaches are very different—in addition to their underlying mechanisms. Although the EC segmentation results from using both modalities were qualitatively similar to each other in paper III, a limited number of seed regions were examined, and this can therefore not be automatically generalized to be valid for all connections across the brain. Furthermore, the measured connectivity might be different from the underlying true connectivity. Combinations of DTI and fMRI have been used both for clinical and research purposes. Clinical applications include neurosurgical planning and investigation of tumors, trauma and dementia [174–177], but these usually focus on the complementary information provided by the two modalities rather than comparing the structural and functional connectivity directly. In neuroscience research, however, DTI and fMRI have been used to investigate their relationship both qualitatively and quantitatively.

Neuroimaging studies have indicated that there generally is a correlation between structural and functional connectivity, but there are some important differences [127, 178–180]. It has

been shown that low values of functional connectivity are not found when there is strong structural connectivity, whereas strong functional connectivity commonly exist between regions without *direct* structural connectivity [181, 182]. Thus, the relationship between structural and functional connectivity is robust when direct structural connections are present, but functional connectivity strengths can still vary over a wide range in the absence of direct structural connections. Strong functional connectivity in these cases might be mediated by indirect structural connections or inter-regional distance. This is consistent with our results from paper III where we seeded structural and functional connectivity analyses from the MEC and LEC segmentations: The structural connections were largely preserved in the functional connectivity maps, but the functional connections were more extensive. However, note that the appearance of these maps depends on the selected thresholding level, and that structural connectivity from probabilistic tractography is inherently weakened with increasing distance. Functional connectivity analysis, on the other hand, is sensitive to also the long-range correlations. Furthermore, the EC connectivity patterns with the other ROIs were similar for both modalities, and this can then be explained by the fact that we already had established the structural connectivity between the EC and the other ROIs in paper II (in addition to studies in other species), and that significant functional connectivity therefore also should be present. However, while structural connectivity is highly stable over time, functional connectivity can substantially reconfigure—it is dynamic. Although rs-fMRI experiments have been shown to yield stable functional connectivity networks in as little as five minutes, there is still variability between scanning sessions and participants [122, 182]. There have also been attempts to model the relationship between functional and structural connectivity mathematically [183, 184], but because of the aforementioned reasons this is a highly complex task. Other approaches include joint connectivity analyses on fused DTI and fMRI data [185–188]. At last, a relatively simple and widely used application of combined DTI and fMRI that should be mentioned is to define a seed ROI for structural connectivity analysis from functional connectivity analysis, or vice versa [188–190].

When comparing structural and functional connectivity, it is also important to be aware of their definitions. The definition of *structural connectivity* is generally agreed upon: The existence of white matter tracts between two brain regions [127]. *Functional connectivity*, on the other hand, has been subject to more controversy [191]. In fMRI analyses, it is usually defined as regions with temporal correlation of brain activity [192]. However, this defini-

tion does not necessarily mean that there is any kind of communication or transfer of information between the regions. Does correlation actually equal connectivity? Furthermore, neither structural nor functional connectivity provide any information about the directionality of the connections or causal relationships. A third type of connectivity describes this, namely *effective connectivity* [127, 192]. This is defined as the influence one neural system exerts over another, either directly or indirectly, and can be considered as a special case of functional connectivity. One suggested method for estimating effective connectivity is with the use of covariances with or without time shifts [193]. Although our results in paper III showed a relatively good agreement between structural and functional connectivity of the EC, it is possible that effective connectivity would have been a more suitable approach for our research question than functional connectivity. This is dependent on whether the connectivity relationship between the EC and the associated regions is best described by synchronized patterns of activity, or if they influence each other in a more sequential or hierarchical manner.

Finally, can "connectivity strength" really be quantified at all in order to directly compare structural and functional connectivity? As previously mentioned, structural connectivity is a relative measure that depends on a number of factors including path lengths, seed ROI sizes, number of possible path directions per voxel, and acquisition parameters. Functional connectivity also depends on the acquisition, data quality and preprocessing. Even though strong structural and functional connectivity strengths have been correlated, it is important to keep these limitations in mind when interpreting the results. In paper II, we did not impose any assumptions about the structural connectivity strengths, but only normalized the connectivity maps by their maximum value. The resulting MEC and LEC segmentations therefore had unequal sizes. In paper III, on the other hand, we normalized all the connectivity maps such that the resulting MEC and LEC segmentations always had the same size. Not much is known about whether this is actually the case in humans, but we chose to do this to try to counterbalance apparent functional connectivity differences caused by spatial proximity and SNR variations of the brain regions. It is therefore important to realize that our results represent relative and not absolute measures of connectivity strength. Nevertheless, they provide information about the intrinsic structural and functional connectivity patterns of the EC.

4.3.3 Applications of advanced MRI methods across disciplines

Until now, we have discussed the MRI methods for cancer and neuroimaging separately. Different clinical and research fields often also use different advanced applications of MRI. For example, although simple DWI is not only used for cancer imaging, but also routinely used for e.g. stroke and head trauma, DTI is on the other hand not widely used clinically outside the brain. Furthermore, there is a variability between the types of MRI used for different types of cancer. Can different disciplines learn more from each other in the future?

The prostate contains glandular tissue, which means there is a diffusion anisotropy that can be mapped with DTI. Different studies have shown a variety of higher, lower or unchanged FA values in prostate cancer, and its significance therefore remains controversial [194]. Although concomitant edema can decrease the FA values, they can also be increased by compression of tracts by the tumor. However, another interesting approach is to perform actual tractography of the glandular tracts. It is reasonable to expect that the normal glandular pattern is somehow disrupted in tumors, and this has also been shown in a few studies [195, 196]. What might seem counter-intuitive, though, is that the fiber tract density actually has been found to be higher in cancer than in normal tissue. A suggested explanation for this is an increased amount of neuronal fibers in prostate cancers [197, 198], and tractography is usually not designed to differentiate between different types of tracts. Maybe including TE and diffusion time dependence in fODF models can aid such specificity? Another application to tractography in the prostate could be instead of detecting significant, solid tumors, to use slight changes in the anisotropy profiles of the tracts for detecting pre-tumorous cancer cells that are sparsely distributed in normal tissue. Not only might these cause perturbations of the glandular fiber pattern, they might also cause intra-glandular blockages past which the water molecules cannot diffuse.

For rather obvious reasons, rs-fMRI cannot be directly applied to the prostate, but there are still some principles that can be adapted for cancer imaging. The sequence used in fMRI is normally a T_2*-weighted sequence which is sensitive to oxygenation effects of the blood. Because tumors are often characterized by abnormal vasculature, haemorrhages and hypoxia, which is a lack of oxygen, this preponderance of deoxy-Hb can be detected by T_2*-weighted imaging, either with or without contrast agent enhancement. However, hypoxic tumors will probably already have progressed to a size where they are detectable with other

imaging modalities, but it could provide additional information about tumor aggressiveness. Hypoxia is usually associated with more aggressive cancers that are less responsive to treatment. The use of T_2*-weighted dynamic susceptibility contrast (DSC) MRI for prediction of treatment response and patient prognosis has already been investigated in rectal cancer, with promising results [199, 200].

Different types of MRI are often used for diagnosis of different types of cancer. As mentioned in Section 1.2.2, T_2-weighted imaging and DWI constitute the backbone of a diagnostic protocol for prostate cancer—DCE can also be included but usually has less of an importance [68]. In breast cancer, on the other hand, the standard is to use T_2-weighted imaging and DCE, whereas DWI is not routinely used [201]. This of course has to do with the different microstructure of prostate and breast tissue and tumors, although advanced diffusion models also have shown promise in the breast [202, 203]. Cancer is a highly diverse group of diseases, therefore also requiring different MRI methods [70]. Nevertheless, DWI is very versatile, and advanced diffusion modeling can be tailored to characterize a variety of tissue compositions. Different numbers of tissue components and choice of b-values, TEs and diffusion times can be used to design an appropriate model. DTI is also a possible application for cancers in tissue with highly directionally arranged structures, e.g. in muscle [204]. As noted in Section 4.3.1, however, such advanced models might not be clinically feasible at the current stage, but this could change in the future.

If we shift our focus over to the identification of the human homologues of MEC and LEC, advanced diffusion modeling of the gray matter tissue could potentially provide additional information about the cellular microstructure. There are cytoarchitectonic differences throughout the human EC [205], and although there might not be a sharp border between the subregions, it would be interesting to use high-resolution advanced DWI to characterize a possible gradient between them. The ADC- and T_2-based two-component could be applied for this, or a similar model with even more components.

There is also a potential for extending the principles related to TE and diffusion time dependence to DTI and advanced diffusion models for tractography. In fact, the co-dependent relationship of ADCs and T_2 values was actually first described in DWI and DTI of the brain and nervous system [81, 82, 206]. While water inside the axons has a long T_2 and highly

anisotropic diffusion, water within the myelin sheath has a short T_2 and lower diffusion anisotropy. An fODF model with both ADC and T_2 dependence, based on similar principles as our two-component model for the prostate, could therefore be used to more accurately extract the signal fraction and anisotropic diffusion of the axon component. This might improve fiber tracking and possibly also tract specificity.

4.4 Implications and impact

The findings of this work first and foremost have implications for research in prostate cancer and neuroscience, but might have potential clinical value in the future. There are immense ongoing research efforts in these fields, in order to ultimately improve the understanding of and clinical care in cancer and neurodegenerative diseases.

The results from paper I show the potential of using an ADC- and T_2-dependent two-component model based on combined T_2-DWI for prostate cancer diagnosis. Although the model performed similarly, but not notably better than more conventional models at this stage, further improvements might change this. Our results can be used as a starting point for other researchers to further improve both the imaging protocol and parameters of the two-component model. There is hope that this added T_2 dependence of advanced diffusion modeling can provide more information about the underlying tissue microstructure in prostate cancer. In the future, this understanding might aid characterization of tumor aggressiveness and treatment stratification.

The locations of the human homologues of MEC and LEC predicted in paper II and III using both DTI and fMRI support and strengthen the previously suggested subdivision into pmEC and alEC, although with a larger medial-lateral component. Correctly delineating these subregions is of importance not only for research in systems neuroscience, but also for cognitive neuroscience research on memory formation, spatial navigation and time processing—e.g. to disentangle cognitive functions such as processing of space vs. time. Furthermore, it can aid translational studies on neurodegenerative processes such as Alzheimer's disease, which starts in the EC and transentorhinal area. Knowing the locations of the human EC subregions will be important for investigation of how MEC and LEC are differentially affected in early Alzheimer's.

Both cancer and dementia are huge global health care problems, and will probably keep increasing in the future as the population grows older. While cancer is already one of the leading causes of death, the incidence of dementia is expected to rise sharply in the future—in 2015, dementia affected 47 million people worldwide, but this is predicted to increase to 132 million by 2050 [7–9]. Basic research in these fields is crucial to know more about the diseases. Advanced MRI methods have the potential to serve as a powerful and non-invasive tool for improving their detection and diagnosis, and enhance understanding in order to potentially find new treatments or cures.

Chapter 5

Conclusions and future perspectives

In this work, the aim was to develop and apply advanced MRI methods to research areas in cancer and neuroscience. The papers included in this thesis focus on how advanced DWI and fMRI can be used in characterization of prostate cancer and the entorhinal cortex.

First, we showed that a novel ADC- and T_2-dependent two-component model based on combined T_2-DWI is able to differentiate between tumor and normal prostate tissue, and has a fair correlation with tumor aggressiveness. Although it only performed similarly, and not significantly better than an only ADC-based bi-exponential model and mono-exponential ADC, it shows promise for diagnosis and characterization of prostate cancer and should be further investigated using a wider range of b-values, TEs and diffusion times.

We then applied DTI and rs-fMRI together with known anatomical connections from other species, in order to segment the EC into the human homologues of MEC and LEC. Our results showed that the human EC can be subdivided into posteromedial (pmEC) and anterolateral (alEC) parts. This is similar to the findings from previous fMRI studies, although with more of a medial-lateral orientation of the border between the subregions. We also showed that using structural and functional connectivity from the same seed regions both resulted in qualitatively similar segmentation results and connectivity patterns within the EC. Furthermore, we found the DTI results to be relatively reproducible across participant cohorts and acquisition protocols.

In conclusion, the research in this thesis demonstrates how advanced DWI can be used to model different types of tissue, by incorporating different parameters describing the T_2 re-

laxation, diffusivity and diffusion anisotropy of the underlying microstructure. It also shows that measures of structural connectivity derived from DTI and functional connectivity from fMRI are able to similarly describe relationships between brain regions. It is evident that both cancer and neuroimaging are highly relevant disciplines for applications of advanced MRI methods.

In the future, we can expect that the use of such advanced MRI methods will be facilitated and enhanced by improvements in both hardware and software. The dependence on T_2 relaxation and diffusion times will probably receive more attention in advanced diffusion modeling, also in DTI. Furthermore, as part of ongoing efforts to map the human brain connectome, we will get a better understanding of structural and functional connectivity, and how these measures derived from DTI and fMRI relate to each other. Even though many advanced MRI methods are currently limited to research use and are not widely used in the clinic, this can change in the future. Technological advances that will potentially be of importance include moving to higher field strengths, applying new motion correction techniques, and increased use of machine learning and artificial intelligence. This of course also introduces new challenges, but the MRI research community has previously shown the ability to overcome these. In the last 20 years there have been improvements in MRI methods that seemed impossible at the time, so who knows where the next 20 years will take us? We have still not reached the limit of what is possible with this powerful and versatile modality, but the development and application of advanced MRI methods will lead us closer.

Bibliography

[1] R. W. Brown, Y.-C. N. Cheng, E. M. Haacke, M. R. Thompson, and R. Venkatesan, *Magnetic Resonance Imaging: Physical Principles and Sequence Design*, 2nd ed. Wiley-Blackwell, 2014.

[2] C. Westbrook and J. Talbot, *MRI in Practice*, 5th ed. Wiley-Blackwell, 2018.

[3] M. A. Bernstein, K. F. King, and Z. J. Zhou, *Handbook of MRI pulse sequences*. Elsevier Academic Press, 2004.

[4] P. C. Lauterbur, "Image formation by induced local interactions: Examples employing nuclear magnetic resonance," *Nature*, vol. 242, no. 5394, pp. 190–191, 1973.

[5] P. Mansfield and P. K. Grannell, "NMR 'diffraction' in solids?" *Journal of Physics C: Solid State Physics*, vol. 6, no. 22, pp. L422–L426, 1973.

[6] R. Damadian, "Tumor detection by nuclear magnetic resonance," *Science*, vol. 171, no. 3976, pp. 1151–1153, 1971.

[7] H. Wang, M. Naghavi, C. Allen, R. M. Barber, Z. A. Bhutta, A. Carter, D. C. Casey, F. J. Charlson, A. Z. Chen, M. M. Coates, M. Coggeshall, L. Dandona, D. J. Dicker, H. E. Erskine, A. J. Ferrari, C. Fitzmaurice, K. Foreman, M. H. Forouzanfar, M. S. Fraser, N. Fullman, P. W. Gething, E. M. Goldberg, N. Graetz, J. A. Haagsma, S. I. Hay, C. Huynh, C. O. Johnson, N. J. Kassebaum, Y. Kinfu, X. R. Kulikoff, M. Kutz, H. H. Kyu, H. J. Larson, J. Leung, X. Liang, S. S. Lim, M. Lind, R. Lozano, N. Marquez, G. A. Mensah, J. Mikesell, A. H. Mokdad, M. D. Mooney, G. Nguyen, E. Nsoesie, D. M. Pigott, C. Pinho, G. A. Roth, J. A. Salomon, L. Sandar, N. Silpakit, A. Sligar, R. J. D. Sorensen, J. Stanaway, C. Steiner, S. Teeple, B. A. Thomas, C. Troeger, A. VanderZanden, S. E. Vollset, V. Wanga, H. A. Whiteford, T. Wolock, L. Zoeckler, K. H. Abate, C. Abbafati, K. M. Abbas, F. Abd-Allah, S. F. Abera, D. M. X. Abreu, L. J. Abu-Raddad, G. Y. Abyu, T. Achoki, A. L. Adelekan,

Z. Ademi, A. K. Adou, J. C. Adsuar, K. A. Afanvi, A. Afshin, E. E. Agardh, A. Agarwal, A. Agrawal, A. A. Kiadaliri, O. N. Ajala, A. S. Akanda, R. O. Akinyemi, T. F. Akinyemiju, N. Akseer, F. H. A. Lami, S. Alabed, Z. Al-Aly, K. Alam, N. K. M. Alam, D. Alasfoor, S. F. Aldhahri, R. W. Aldridge, M. A. Alegretti, A. V. Aleman, Z. A. Alemu, L. T. Alexander *et al.*, "Global, regional, and national life expectancy, all-cause mortality, and cause-specific mortality for 249 causes of death, 1980–2015: a systematic analysis for the Global Burden of Disease Study 2015," *The Lancet*, vol. 388, no. 10053, pp. 1459–1544, 2016.

[8] World Health Organization, "Global action plan on the public health response to dementia 2017-2025," Report, 2017. [Online]. Available: https://www.who.int/publications/i/item/global-action-plan-on-the-public-health-response-to-dementia-2017---2025

[9] Folkehelseinstituttet, "Dødsårsaksregisteret," Report, 2020. [Online]. Available: http://statistikkbank.fhi.no/dar/

[10] W. Gerlach and O. Stern, "Über die richtungsquantelung im magnetfeld," *Annalen der Physik*, vol. 379, no. 16, pp. 673–699, 1924.

[11] I. I. Rabi, J. R. Zacharias, S. Millman, and P. Kusch, "A new method of measuring nuclear magnetic moment," *Physical Review*, vol. 53, no. 4, pp. 318–318, 1938.

[12] F. Bloch, "Nuclear induction," *Physical Review*, vol. 70, no. 7-8, pp. 460–474, 1946.

[13] E. M. Purcell, H. C. Torrey, and R. V. Pound, "Resonance absorption by nuclear magnetic moments in a solid," *Physical Review*, vol. 69, no. 1-2, pp. 37–38, 1946.

[14] A. Einstein, "Über die von der molekularkinetischen theorie der wärme geforderte bewegung von in ruhenden flüssigkeiten suspendierten teilchen," *Annalen der Physik*, vol. 322, no. 8, pp. 549–560, 1905.

[15] H. Y. Carr and E. M. Purcell, "Effects of diffusion on free precession in nuclear magnetic resonance experiments," *Physical Review*, vol. 94, no. 3, pp. 630–638, 1954.

[16] E. O. Stejskal and J. E. Tanner, "Spin diffusion measurements: Spin echoes in the presence of a time-dependent field gradient," *The Journal of Chemical Physics*, vol. 42, no. 1, pp. 288–292, 1965.

[17] D. L. Bihan, "Molecular diffusion, tissue microdynamics and microstructure," *NMR in Biomedicine*, vol. 8, no. 7, pp. 375–386, 1995.

[18] T. R. Hope, N. S. White, J. Kuperman, Y. Chao, G. Yamin, H. Bartch, N. M. Schenker-Ahmed, R. Rakow-Penner, R. Bussell, N. Nomura, S. Kesari, A. Bjørnerud, and A. M. Dale, "Demonstration of non-Gaussian restricted diffusion in tumor cells using diffusion time-dependent diffusion-weighted magnetic resonance imaging contrast," *Front Oncol*, vol. 6, p. 179, 2016.

[19] Y. Assaf and Y. Cohen, "Non-mono-exponential attenuation of water and N-acetyl aspartate signals due to diffusion in brain tissue," *J Magn Reson*, vol. 131, no. 1, pp. 69–85, 1998.

[20] J. H. Jensen, J. A. Helpern, A. Ramani, H. Lu, and K. Kaczynski, "Diffusional kurtosis imaging: the quantification of non-gaussian water diffusion by means of magnetic resonance imaging," *Magn Reson Med*, vol. 53, no. 6, pp. 1432–40, 2005.

[21] R. A. Karunamuni, J. Kuperman, T. M. Seibert, N. Schenker, R. Rakow-Penner, V. S. Sundar, J. R. Teruel, P. E. Goa, D. S. Karow, A. M. Dale, and N. S. White, "Relationship between kurtosis and bi-exponential characterization of high b-value diffusion-weighted imaging: application to prostate cancer," *Acta Radiol*, vol. 59, no. 12, pp. 1523–1529, 2018.

[22] R. V. Mulkern, A. S. Barnes, S. J. Haker, Y. P. Hung, F. J. Rybicki, S. E. Maier, and C. M. Tempany, "Biexponential characterization of prostate tissue water diffusion decay curves over an extended b-factor range," *Magn Reson Imaging*, vol. 24, no. 5, pp. 563–8, 2006.

[23] H. Shinmoto, K. Oshio, A. Tanimoto, N. Higuchi, S. Okuda, S. Kuribayashi, and R. V. Mulkern, "Biexponential apparent diffusion coefficients in prostate cancer," *Magn Reson Imaging*, vol. 27, no. 3, pp. 355–9, 2009.

[24] L. Egnell, I. Vidić, N. P. Jerome, A. M. Bofin, T. F. Bathen, and P. E. Goa, "Stromal collagen content in breast tumors correlates with in vivo diffusion-weighted imaging: a comparison of multi b-value DWI with histologic specimen from benign and malignant breast lesions," *J Magn Reson Imaging*, vol. 51, no. 6, pp. 1868–1878, 2020.

[25] N. S. White, T. B. Leergaard, H. D'Arceuil, J. G. Bjaalie, and A. M. Dale, "Probing tissue microstructure with restriction spectrum imaging: Histological and theoretical validation," *Hum Brain Mapp*, vol. 34, no. 2, pp. 327–46, 2013.

[26] N. S. White, C. R. McDonald, N. Farid, J. Kuperman, D. Karow, N. M. Schenker-Ahmed, H. Bartsch, R. Rakow-Penner, D. Holland, A. Shabaik, A. Bjørnerud, T. Hope, J. Hattangadi-Gluth, M. Liss, J. K. Parsons, C. C. Chen, S. Raman, D. Margolis, R. E. Reiter, L. Marks, S. Kesari, A. J. Mundt, C. J. Kane, B. S. Carter, W. G. Bradley, and A. M. Dale, "Diffusion-weighted imaging in cancer: Physical foundations and applications of restriction spectrum imaging," *Cancer Research*, vol. 74, no. 17, pp. 4638–4652, 2014.

[27] C. C. Conlin, C. H. Feng, A. E. Rodriguez-Soto, R. A. Karunamuni, J. M. Kuperman, D. Holland, R. Rakow-Penner, M. E. Hahn, T. M. Seibert, and A. M. Dale, "Improved characterization of diffusion in normal and cancerous prostate tissue through optimization of multicompartmental signal models," *Journal of Magnetic Resonance Imaging*, vol. 53, no. 2, pp. 628–639, 2021.

[28] P. J. Basser, J. Mattiello, and D. LeBihan, "MR diffusion tensor spectroscopy and imaging," *Biophys J*, vol. 66, no. 1, pp. 259–67, 1994.

[29] C. Pierpaoli, P. Jezzard, P. J. Basser, A. Barnett, and G. Di Chiro, "Diffusion tensor MR imaging of the human brain," *Radiology*, vol. 201, no. 3, pp. 637–48, 1996.

[30] S. Ogawa, D. W. Tank, R. Menon, J. M. Ellermann, S. G. Kim, H. Merkle, and K. Ugurbil, "Intrinsic signal changes accompanying sensory stimulation: functional brain mapping with magnetic resonance imaging," *Proceedings of the National Academy of Sciences*, vol. 89, no. 13, pp. 5951–5955, 1992.

[31] K. K. Kwong, J. W. Belliveau, D. A. Chesler, I. E. Goldberg, R. M. Weisskoff, B. P. Poncelet, D. N. Kennedy, B. E. Hoppel, M. S. Cohen, and R. Turner, "Dynamic magnetic resonance imaging of human brain activity during primary sensory stimulation," *Proceedings of the National Academy of Sciences*, vol. 89, no. 12, pp. 5675–5679, 1992.

[32] P. A. Bandettini, E. C. Wong, R. S. Hinks, R. S. Tikofsky, and J. S. Hyde, "Time course EPI of human brain function during task activation," *Magnetic Resonance in Medicine*, vol. 25, no. 2, pp. 390–397, 1992.

[33] K. J. Friston, "Modalities, modes, and models in functional neuroimaging," *Science*, vol. 326, no. 5951, pp. 399–403, 2009.

[34] P. M. Matthews, G. D. Honey, and E. T. Bullmore, "Applications of fMRI in translational medicine and clinical practice," *Nature Reviews Neuroscience*, vol. 7, no. 9, pp. 732–744, 2006.

[35] S. Ogawa, T.-M. Lee, A. S. Nayak, and P. Glynn, "Oxygenation-sensitive contrast in magnetic resonance image of rodent brain at high magnetic fields," *Magnetic Resonance in Medicine*, vol. 14, no. 1, pp. 68–78, 1990.

[36] S. Ogawa, T. M. Lee, A. R. Kay, and D. W. Tank, "Brain magnetic resonance imaging with contrast dependent on blood oxygenation," *Proceedings of the National Academy of Sciences*, vol. 87, no. 24, pp. 9868–9872, 1990.

[37] L. Pauling and C. D. Coryell, "The magnetic properties and structure of hemoglobin, oxyhemoglobin and carbonmonoxyhemoglobin," *Proceedings of the National Academy of Sciences*, vol. 22, no. 4, pp. 210–216, 1936.

[38] A. M. Blamire, S. Ogawa, K. Ugurbil, D. Rothman, G. McCarthy, J. M. Ellermann, F. Hyder, Z. Rattner, and R. G. Shulman, "Dynamic mapping of the human visual cortex by high-speed magnetic resonance imaging," *Proceedings of the National Academy of Sciences*, vol. 89, no. 22, pp. 11 069–11 073, 1992.

[39] R. B. Buxton, K. Uludağ, D. J. Dubowitz, and T. T. Liu, "Modeling the hemodynamic response to brain activation," *NeuroImage*, vol. 23, pp. S220–S233, 2004.

[40] J. E. Chen and G. H. Glover, "Functional magnetic resonance imaging methods," *Neuropsychology Review*, vol. 25, no. 3, pp. 289–313, 2015.

[41] M. J. Brookes, J. R. Hale, J. M. Zumer, C. M. Stevenson, S. T. Francis, G. R. Barnes, J. P. Owen, P. G. Morris, and S. S. Nagarajan, "Measuring functional connectivity using MEG: Methodology and comparison with fcMRI," *NeuroImage*, vol. 56, no. 3, pp. 1082–1104, 2011.

[42] E. Tagliazucchi, F. Von Wegner, A. Morzelewski, V. Brodbeck, and H. Laufs, "Dynamic BOLD functional connectivity in humans and its electrophysiological correlates," *Frontiers in Human Neuroscience*, vol. 6, no. 339, 2012.

[43] M. Stehling, R. Turner, and P. Mansfield, "Echo-planar imaging: magnetic resonance imaging in a fraction of a second," *Science*, vol. 254, no. 5028, pp. 43–50, 1991.

[44] P. Mansfield, "Multi-planar image formation using NMR spin echoes," *Journal of Physics C: Solid State Physics*, vol. 10, no. 3, pp. L55–L58, 1977.

[45] M. Nau, "Functional imaging of the human medial temporal lobe," 2020. [Online]. Available: https://doi.org/10.17605/OSF.IO/CQN4Z

[46] M. H. Buonocore and L. Gao, "Ghost artifact reduction for echo planar imaging using image phase correction," *Magnetic Resonance in Medicine*, vol. 38, no. 1, pp. 89–100, 1997.

[47] J. Zhuang, J. Hrabe, A. Kangarlu, D. Xu, R. Bansal, C. A. Branch, and B. S. Peterson, "Correction of eddy-current distortions in diffusion tensor images using the known directions and strengths of diffusion gradients," *Journal of Magnetic Resonance Imaging*, vol. 24, no. 5, pp. 1188–1193, 2006.

[48] G. Nketiah, K. M. Selnæs, E. Sandsmark, J. R. Teruel, B. Krüger-Stokke, H. Bertilsson, T. F. Bathen, and M. Elschot, "Geometric distortion correction in prostate diffusion-weighted MRI and its effect on quantitative apparent diffusion coefficient analysis," *Magnetic Resonance in Medicine*, vol. 79, no. 5, pp. 2524–2532, 2018.

[49] P. Jezzard, "Correction of geometric distortion in fMRI data," *NeuroImage*, vol. 62, no. 2, pp. 648–651, 2012.

[50] J. Hardin and G. Bertoni, *Becker's World of the cell*, 9th ed. Pearson, 2016.

[51] D. Hanahan and R. A. Weinberg, "The hallmarks of cancer," *Cell*, vol. 100, no. 1, pp. 57–70, 2000.

[52] D. Hanahan and R. Weinberg, "Hallmarks of cancer: The next generation," *Cell*, vol. 144, no. 5, pp. 646–674, 2011.

[53] H. Sung, J. Ferlay, R. L. Siegel, M. Laversanne, I. Soerjomataram, A. Jemal, and F. Bray, "Global cancer statistics 2020: GLOBOCAN estimates of incidence and mortality worldwide for 36 cancers in 185 countries," *CA: A Cancer Journal for Clinicians*, vol. 71, no. 3, pp. 209–249, 2021.

[54] Cancer Registry of Norway, "Cancer in Norway 2019 - cancer incidence, mortality, survival and prevalence in Norway," Report, 2020. [Online]. Available: https://www.kreftregisteret.no/globalassets/cancer-in-norway/2019/cin_report.pdf

[55] G. Wang, D. Zhao, D. J. Spring, and R. A. DePinho, "Genetics and biology of prostate cancer," *Genes & Development*, vol. 32, no. 17-18, pp. 1105–1140, 2018.

[56] J. E. McNeal, "The zonal anatomy of the prostate," *The Prostate*, vol. 2, no. 1, pp. 35–49, 1981.

[57] J. A. Sinnott, J. R. Rider, J. Carlsson, T. Gerke, S. Tyekucheva, K. L. Penney, H. D. Sesso, M. Loda, K. Fall, M. J. Stampfer, L. A. Mucci, Y. Pawitan, S.-O. Andersson, and O. Andrén, "Molecular differences in transition zone and peripheral zone prostate tumors," *Carcinogenesis*, vol. 36, no. 6, pp. 632–638, 2015.

[58] J. J. Lee, I. C. Thomas, R. Nolley, M. Ferrari, J. D. Brooks, and J. T. Leppert, "Biologic differences between peripheral and transition zone prostate cancer," *The Prostate*, vol. 75, no. 2, pp. 183–190, 2015.

[59] Helsedirektoratet, "Pakkeforløp for prostatakreft," Report, 2014. [Online]. Available: https://www.helsedirektoratet.no/pakkeforlop/prostatakreft

[60] Helsedirektoratet, "Nasjonalt handlingsprogram med retningslinjer for diagnostikk, behandling og oppfølging av prostatakreft," Report, 2015. [Online]. Available: https://www.helsedirektoratet.no/retningslinjer/prostatakreft-handlingsprogram

[61] M. Eylert and R. Persad, "Management of prostate cancer," *British Journal of Hospital Medicine*, vol. 73, no. 2, pp. 95–96, 2012.

[62] D. F. Gleason, "Classification of prostatic carcinomas," *Cancer Chemother Rep*, vol. 50, no. 3, pp. 125–8, 1966.

[63] J. I. Epstein, L. Egevad, M. B. Amin, B. Delahunt, J. R. Srigley, P. A. Humphrey, and C. the Grading, "The 2014 International Society of Urological Pathology (ISUP) consensus conference on Gleason grading of prostatic carcinoma: Definition of grading patterns and proposal for a new grading system," *The American Journal of Surgical Pathology*, vol. 40, no. 2, 2016.

[64] S. Loeb, M. A. Bjurlin, J. Nicholson, T. L. Tammela, D. F. Penson, H. B. Carter, P. Carroll, and R. Etzioni, "Overdiagnosis and overtreatment of prostate cancer," *European Urology*, vol. 65, no. 6, pp. 1046–1055, 2014.

[65] V. Narayan, S. Jiang, and C. A. Warlick, "Early stage cancer in older adults: Prostate—avoiding overtreatment and undertreatment," *The Cancer Journal*, vol. 23, no. 4, 2017.

[66] Y. Mazaheri, A. Shukla-Dave, A. Muellner, and H. Hricak, "MRI of the prostate: clinical relevance and emerging applications," *J Magn Reson Imaging*, vol. 33, no. 2, pp. 258–274, 2011.

[67] C. M. Moore, N. L. Robertson, N. Arsanious, T. Middleton, A. Villers, L. Klotz, S. S. Taneja, and M. Emberton, "Image-guided prostate biopsy using magnetic resonance imaging–derived targets: A systematic review," *European Urology*, vol. 63, no. 1, pp. 125–140, 2013.

[68] J. O. Barentsz, J. C. Weinreb, S. Verma, H. C. Thoeny, C. M. Tempany, F. Shtern, A. R. Padhani, D. Margolis, K. J. Macura, M. A. Haider, F. Cornud, and P. L. Choyke, "Synopsis of the PI-RADS v2 guidelines for multiparametric prostate magnetic resonance imaging and recommendations for use," *Eur Urol*, vol. 69, no. 1, pp. 41–9, 2016.

[69] B. Issa, "In vivo measurement of the apparent diffusion coefficient in normal and malignant prostatic tissues using echo-planar imaging," *J Magn Reson Imaging*, vol. 16, no. 2, pp. 196–200, 2002.

[70] A. Surov, H. J. Meyer, and A. Wienke, "Correlation between apparent diffusion coefficient (ADC) and cellularity is different in several tumors: a meta-analysis," *Oncotarget*, vol. 8, no. 35, pp. 59 492–59 499, 2017.

[71] S. Verma, A. Rajesh, H. Morales, L. Lemen, G. Bills, M. Delworth, K. Gaitonde, J. Ying, R. Samartunga, and M. Lamba, "Assessment of aggressiveness of prostate cancer: correlation of apparent diffusion coefficient with histologic grade after radical prostatectomy," *AJR Am J Roentgenol*, vol. 196, no. 2, pp. 374–81, 2011.

[72] J. J. Fütterer, A. Briganti, P. De Visschere, M. Emberton, G. Giannarini, A. Kirkham, S. S. Taneja, H. Thoeny, G. Villeirs, and A. Villers, "Can clinically significant prostate cancer

be detected with multiparametric magnetic resonance imaging? a systematic review of the literature," *Eur Urol*, vol. 68, no. 6, pp. 1045–53, 2015.

[73] T. Kobus, P. C. Vos, T. Hambrock, M. De Rooij, C. A. Hulsbergen-Van de Kaa, J. O. Barentsz, A. Heerschap, and T. W. Scheenen, "Prostate cancer aggressiveness: in vivo assessment of MR spectroscopy and diffusion-weighted imaging at 3 T," *Radiology*, vol. 265, no. 2, pp. 457–67, 2012.

[74] A. C. Westphalen, C. E. McCulloch, J. M. Anaokar, S. Arora, N. S. Barashi, J. O. Barentsz, T. K. Bathala, L. K. Bittencourt, M. T. Booker, V. G. Braxton, P. R. Carroll, D. D. Casalino, S. D. Chang, F. V. Coakley, R. Dhatt, S. C. Eberhardt, B. R. Foster, A. T. Froemming, J. J. Fütterer, D. M. Ganeshan, M. R. Gertner, L. M. Gettle, S. Ghai, R. T. Gupta, M. E. Hahn, R. Houshyar, C. Kim, C. K. Kim, C. Lall, D. J. A. Margolis, S. E. McRae, A. Oto, R. B. Parsons, N. U. Patel, P. A. Pinto, T. J. Polascik, B. Spilseth, J. B. Starcevich, V. S. Tammisetti, S. S. Taneja, B. Turkbey, S. Verma, J. F. Ward, C. A. Warlick, A. R. Weinberger, J. Yu, R. J. Zagoria, and A. B. Rosenkrantz, "Variability of the positive predictive value of PI-RADS for prostate MRI across 26 centers: experience of the Society of Abdominal Radiology prostate cancer disease-focused panel," *Radiology*, vol. 296, no. 1, pp. 76–84, 2020.

[75] C. M. Hoeks, T. Hambrock, D. Yakar, C. A. Hulsbergen-van de Kaa, T. Feuth, J. A. Witjes, J. J. Fütterer, and J. O. Barentsz, "Transition zone prostate cancer: detection and localization with 3-T multiparametric MR imaging," *Radiology*, vol. 266, no. 1, pp. 207–17, 2013.

[76] M. Sasaki, K. Yamada, Y. Watanabe, M. Matsui, M. Ida, S. Fujiwara, and E. Shibata, "Variability in absolute apparent diffusion coefficient values across different platforms may be substantial: A multivendor, multi-institutional comparison study," *Radiology*, vol. 249, no. 2, pp. 624–630, 2008.

[77] R. Bourne and E. Panagiotaki, "Limitations and prospects for diffusion-weighted MRI of the prostate," *Diagnostics (Basel)*, vol. 6, no. 2, p. 21, 2016.

[78] T. L. Chenevert, P. C. Sundgren, and B. D. Ross, "Diffusion imaging: Insight to cell status and cytoarchitecture," *Neuroimaging Clinics of North America*, vol. 16, no. 4, pp. 619–632, 2006.

[79] C. Nicholson, "Factors governing diffusing molecular signals in brain extracellular space," *Journal of Neural Transmission*, vol. 112, no. 1, pp. 29–44, 2005.

[80] T. H. Storas, K. I. Gjesdal, O. B. Gadmar, J. T. Geitung, and N. E. Klow, "Prostate magnetic resonance imaging: multiexponential T2 decay in prostate tissue," *J Magn Reson Imaging*, vol. 28, no. 5, pp. 1166–72, 2008.

[81] G. J. Stanisz and R. M. Henkelman, "Diffusional anisotropy of T2 components in bovine optic nerve," *Magnetic Resonance in Medicine*, vol. 40, no. 3, pp. 405–410, 1998.

[82] J. H. Burdette, A. D. Elster, and P. E. Ricci, "Acute cerebral infarction: quantification of spin-density and T2 shine-through phenomena on diffusion-weighted MR images," *Radiology*, vol. 212, no. 2, pp. 333–9, 1999.

[83] J. M. Provenzale, S. T. Engelter, J. R. Petrella, J. S. Smith, and J. R. MacFall, "Use of MR exponential diffusion-weighted images to eradicate T2 "shine-through" effect," *AJR Am J Roentgenol*, vol. 172, no. 2, pp. 537–9, 1999.

[84] S. Wang, Y. Peng, M. Medved, A. N. Yousuf, M. K. Ivancevic, I. Karademir, Y. Jiang, T. Antic, S. Sammet, A. Oto, and G. S. Karczmar, "Hybrid multidimensional T2 and diffusion-weighted MRI for prostate cancer detection," *J Magn Reson Imaging*, vol. 39, no. 4, pp. 781–8, 2014.

[85] M. Sadinski, G. Karczmar, Y. Peng, S. Wang, Y. Jiang, M. Medved, A. Yousuf, T. Antic, and A. Oto, "Pilot study of the use of hybrid multidimensional T2-weighted imaging-DWI for the diagnosis of prostate cancer and evaluation of Gleason score," *AJR Am J Roentgenol*, vol. 207, no. 3, pp. 592–8, 2016.

[86] X. Ma, H. Chen, and Y. Peng, "Hybrid T2-weighted and diffusion-weighted magnetic resonance imaging for differentiating prostate cancer from benign prostatic hyperplasia," *10th International Congress on Image and Signal Processing, BioMedical Engineering and Informatics*, pp. 1–5, 2017.

[87] A. Chatterjee, R. M. Bourne, S. Wang, A. Devaraj, A. J. Gallan, T. Antic, G. S. Karczmar, and A. Oto, "Diagnosis of prostate cancer with noninvasive estimation of prostate tissue composition by using hybrid multidimensional MR imaging: a feasibility study," *Radiology*, vol. 287, no. 3, pp. 864–873, 2018.

[88] P. C. Sanelli, P. W. Schaefer, and L. A. Loevner, *Neuroimaging: The Essentials*. Wolters Kluwer, 2016.

[89] A. Longstaff, *Neuroscience*, 3rd ed. CRC Press LLC, 2011.

[90] S. H. Lim, H. Nisar, K. W. Thee, and V. V. Yap, "A novel method for tracking and analysis of EEG activation across brain lobes," *Biomedical Signal Processing and Control*, vol. 40, pp. 488–504, 2018.

[91] G. Rizzolatti, M. Fabbri-Destro, F. Caruana, and P. Avanzini, "System neuroscience: Past, present, and future," *CNS Neuroscience & Therapeutics*, vol. 24, no. 8, pp. 685–693, 2018.

[92] T. D. Albright, E. R. Kandel, and M. I. Posner, "Cognitive neuroscience," *Current Opinion in Neurobiology*, vol. 10, no. 5, pp. 612–624, 2000.

[93] G. Di Fede, G. Giaccone, M. Salmona, and F. Tagliavini, "Translational research in Alzheimer's and prion diseases," *J Alzheimers Dis*, vol. 62, no. 3, pp. 1247–1259, 2018.

[94] W. Żakowski, "Animal use in neurobiological research," *Neuroscience*, vol. 433, pp. 1–10, 2020.

[95] W. A. Suzuki and H. Eichenbaum, "The neurophysiology of memory," *Annals of the New York Academy of Sciences*, vol. 911, no. 1, pp. 175–191, 2000.

[96] H. Eichenbaum, A. Yonelinas, and C. Ranganath, "The medial temporal lobe and recognition memory," *Annual Review of Neuroscience*, vol. 30, no. 1, pp. 123–152, 2007.

[97] E. Moser and M.-B. Moser, "Grid cells and neural coding in high-end cortices," *Neuron*, vol. 80, no. 3, pp. 765–774, 2013.

[98] A. Tsao, J. Sugar, L. Lu, C. Wang, J. J. Knierim, M.-B. Moser, and E. I. Moser, "Integrating time from experience in the lateral entorhinal cortex," *Nature*, vol. 561, no. 7721, pp. 57–62, 2018.

[99] A. Maass, H. Schütze, O. Speck, A. Yonelinas, C. Tempelmann, H.-J. Heinze, D. Berron, A. Cardenas-Blanco, K. H. Brodersen, K. Enno Stephan, and E. Düzel, "Laminar activity in the hippocampus and entorhinal cortex related to novelty and episodic encoding," *Nature Communications*, vol. 5, no. 1, p. 5547, 2014.

[100] G. Buzsáki, "The hippocampo-neocortical dialogue," *Cerebral Cortex*, vol. 6, no. 2, pp. 81–92, 1996.

[101] P. Lavenex and D. G. Amaral, "Hippocampal-neocortical interaction: A hierarchy of associativity," *Hippocampus*, vol. 10, no. 4, pp. 420–430, 2000.

[102] M. Muñoz and R. Insausti, "Cortical efferents of the entorhinal cortex and the adjacent parahippocampal region in the monkey (macaca fascicularis)," *European Journal of Neuroscience*, vol. 22, no. 6, pp. 1368–1388, 2005.

[103] K. M. Kerr, K. L. Agster, S. C. Furtak, and R. D. Burwell, "Functional neuroanatomy of the parahippocampal region: The lateral and medial entorhinal areas," *Hippocampus*, vol. 17, no. 9, pp. 697–708, 2007.

[104] C. B. Canto, F. G. Wouterlood, and M. P. Witter, "What does the anatomical organization of the entorhinal cortex tell us?" *Neural Plasticity*, vol. 2008, p. 381243, 2008.

[105] N. M. van Strien, N. L. M. Cappaert, and M. P. Witter, "The anatomy of memory: an interactive overview of the parahippocampal–hippocampal network," *Nature Reviews Neuroscience*, vol. 10, no. 4, pp. 272–282, 2009.

[106] M. Fyhn, S. Molden, M. P. Witter, E. I. Moser, and M.-B. Moser, "Spatial representation in the entorhinal cortex," *Science*, vol. 305, no. 5688, pp. 1258–1264, 2004.

[107] T. Hafting, M. Fyhn, S. Molden, M. B. Moser, and E. I. Moser, "Microstructure of a spatial map in the entorhinal cortex," *Nature*, vol. 436, no. 7052, pp. 801–6, 2005.

[108] J. J. Knierim, J. P. Neunuebel, and S. S. Deshmukh, "Functional correlates of the lateral and medial entorhinal cortex: objects, path integration and local-global reference frames," *Philos Trans R Soc Lond B Biol Sci*, vol. 369, no. 1635, p. 20130369, 2014.

[109] A. Høydal, E. R. Skytøen, S. O. Andersson, M. B. Moser, and E. I. Moser, "Object-vector coding in the medial entorhinal cortex," *Nature*, vol. 568, no. 7752, pp. 400–404, 2019.

[110] S. S. Deshmukh and J. J. Knierim, "Representation of non-spatial and spatial information in the lateral entorhinal cortex," *Front Behav Neurosci*, vol. 5, p. 69, 2011.

[111] A. Tsao, M. B. Moser, and E. I. Moser, "Traces of experience in the lateral entorhinal cortex," *Curr Biol*, vol. 23, no. 5, pp. 399–405, 2013.

[112] T. P. Doan, M. J. Lagartos-Donate, E. S. Nilssen, S. Ohara, and M. P. Witter, "Convergent projections from perirhinal and postrhinal cortices suggest a multisensory nature of lateral, but not medial, entorhinal cortex," *Cell Reports*, vol. 29, no. 3, pp. 617–627.e7, 2019.

[113] C.-C. Huang, E. T. Rolls, C.-C. H. Hsu, J. Feng, and C.-P. Lin, "Extensive cortical connectivity of the human hippocampal memory system: Beyond the "what" and "where" dual stream model," *Cerebral Cortex*, 2021.

[114] A. Maass, D. Berron, L. A. Libby, C. Ranganath, and E. Düzel, "Functional subregions of the human entorhinal cortex," *eLife*, vol. 4, p. e06426, 2015.

[115] T. Navarro Schröder, K. V. Haak, N. I. Zaragoza Jimenez, C. F. Beckmann, and C. F. Doeller, "Functional topography of the human entorhinal cortex," *eLife*, vol. 4, p. e06738, 2015.

[116] H. Braak and E. Braak, "The human entorhinal cortex: normal morphology and lamina-specific pathology in various diseases," *Neuroscience Research*, vol. 15, no. 1, pp. 6–31, 1992.

[117] J. N. Adams, A. Maass, T. M. Harrison, S. L. Baker, and W. J. Jagust, "Cortical tau deposition follows patterns of entorhinal functional connectivity in aging," *eLife*, vol. 8, p. e49132, 2019.

[118] M. Moore, Y. Hu, S. Woo, D. O'Hearn, A. D. Iordan, S. Dolcos, and F. Dolcos, "A comprehensive protocol for manual segmentation of the medial temporal lobe structures," *JoVE*, no. 89, p. e50991, 2014.

[119] J. P. Lerch, A. J. W. van der Kouwe, A. Raznahan, T. Paus, H. Johansen-Berg, K. L. Miller, S. M. Smith, B. Fischl, and S. N. Sotiropoulos, "Studying neuroanatomy using MRI," *Nature Neuroscience*, vol. 20, no. 3, pp. 314–326, 2017.

[120] N. K. Logothetis, "What we can do and what we cannot do with fMRI," *Nature*, vol. 453, no. 7197, pp. 869–878, 2008.

[121] K. Smitha, K. Akhil Raja, K. Arun, P. Rajesh, B. Thomas, T. Kapilamoorthy, and C. Kesavadas, "Resting state fMRI: A review on methods in resting state connectivity analysis and resting state networks," *The Neuroradiology Journal*, vol. 30, no. 4, pp. 305–317, 2017.

[122] K. R. Van Dijk, T. Hedden, A. Venkataraman, K. C. Evans, S. W. Lazar, and R. L. Buckner, "Intrinsic functional connectivity as a tool for human connectomics: theory, properties, and optimization," *J Neurophysiol*, vol. 103, no. 1, pp. 297–321, 2010.

[123] B. Biswal, F. Zerrin Yetkin, V. M. Haughton, and J. S. Hyde, "Functional connectivity in the motor cortex of resting human brain using echo-planar mri," *Magnetic Resonance in Medicine*, vol. 34, no. 4, pp. 537–541, 1995.

[124] D. Cole, S. Smith, and C. Beckmann, "Advances and pitfalls in the analysis and interpretation of resting-state FMRI data," *Frontiers in Systems Neuroscience*, vol. 4, no. 8, 2010.

[125] A. Shmuel and D. A. Leopold, "Neuronal correlates of spontaneous fluctuations in fMRI signals in monkey visual cortex: Implications for functional connectivity at rest," *Human Brain Mapping*, vol. 29, no. 7, pp. 751–761, 2008.

[126] Y. Ma, M. A. Shaik, M. G. Kozberg, S. H. Kim, J. P. Portes, D. Timerman, and E. M. C. Hillman, "Resting-state hemodynamics are spatiotemporally coupled to synchronized and symmetric neural activity in excitatory neurons," *Proceedings of the National Academy of Sciences*, vol. 113, no. 52, pp. E8463–E8471, 2016.

[127] E. Rykhlevskaia, G. Gratton, and M. Fabiani, "Combining structural and functional neuroimaging data for studying brain connectivity: A review," *Psychophysiology*, vol. 45, no. 2, pp. 173–187, 2008.

[128] J. Muller, M. Alizadeh, F. B. Mohamed, J. Riley, J. J. Pearce, B. Trieu, T.-W. Liang, V. Romo, A. Sharan, and C. Wu, "Clinically applicable delineation of the pallidal sensorimotor region in patients with advanced Parkinson's disease: study of probabilistic and deterministic tractography," *Journal of Neurosurgery JNS*, vol. 131, no. 5, pp. 1520–1531, 2019.

[129] S. Mori and J. Zhang, "Principles of diffusion tensor imaging and its applications to basic neuroscience research," *Neuron*, vol. 51, no. 5, pp. 527–39, 2006.

[130] S. Mori, B. J. Crain, V. P. Chacko, and P. C. van Zijl, "Three-dimensional tracking of axonal projections in the brain by magnetic resonance imaging," *Ann Neurol*, vol. 45, no. 2, pp. 265–9, 1999.

[131] B. Jeurissen, M. Descoteaux, S. Mori, and A. Leemans, "Diffusion MRI fiber tractography of the brain," *NMR in Biomedicine*, vol. 32, no. 4, p. e3785, 2019.

[132] T. E. Behrens, M. W. Woolrich, M. Jenkinson, H. Johansen-Berg, R. G. Nunes, S. Clare, P. M. Matthews, J. M. Brady, and S. M. Smith, "Characterization and propagation of uncertainty in diffusion-weighted MR imaging," *Magn Reson Med*, vol. 50, no. 5, pp. 1077–88, 2003.

[133] T. E. Behrens, H. Johansen-Berg, S. Jbabdi, M. F. Rushworth, and M. W. Woolrich, "Probabilistic diffusion tractography with multiple fibre orientations: What can we gain?" *Neuroimage*, vol. 34, no. 1, pp. 144–55, 2007.

[134] S. Jbabdi, S. N. Sotiropoulos, A. M. Savio, M. Graña, and T. E. Behrens, "Model-based analysis of multishell diffusion MR data for tractography: how to get over fitting problems," *Magn Reson Med*, vol. 68, no. 6, pp. 1846–55, 2012.

[135] S. N. Sotiropoulos, M. Hernández-Fernández, A. T. Vu, J. L. Andersson, S. Moeller, E. Yacoub, C. Lenglet, K. Ugurbil, T. E. J. Behrens, and S. Jbabdi, "Fusion in diffusion MRI for improved fibre orientation estimation: An application to the 3T and 7T data of the Human Connectome Project," *Neuroimage*, vol. 134, pp. 396–409, 2016.

[136] A. Hahn, R. Lanzenberger, and S. Kasper, "Making sense of connectivity," *International Journal of Neuropsychopharmacology*, vol. 22, no. 3, pp. 194–207, 2018.

[137] L. Kjonigsen, T. Leergaard, M. Witter, and J. Bjaalie, "Digital atlas of anatomical subdivisions and boundaries of the rat hippocampal region," *Frontiers in Neuroinformatics*, vol. 5, no. 2, 2011.

[138] M. P. Witter, *The perforant path: projections from the entorhinal cortex to the dentate gyrus*. Elsevier, 2007, vol. 163, pp. 43–61.

[139] M. P. Witter and D. G. Amaral, "The entorhinal cortex of the monkey: VI. organization of projections from the hippocampus, subiculum, presubiculum, and parasubiculum," *Journal of Comparative Neurology*, vol. 529, no. 4, pp. 828–852, 2021.

[140] G. T. Prusky and R. M. Douglas, "Characterization of mouse cortical spatial vision," *Vision Research*, vol. 44, no. 28, pp. 3411–3418, 2004.

[141] H. B. M. Uylings, H. J. Groenewegen, and B. Kolb, "Do rats have a prefrontal cortex?" *Behavioural Brain Research*, vol. 146, no. 1, pp. 3–17, 2003.

[142] A. Máté, D. Kis, A. Czigner, T. Fischer, L. Halász, and P. Barzó, "Connectivity-based segmentation of the brainstem by probabilistic tractography," *Brain Res*, vol. 1690, pp. 74–88, 2018.

[143] M. Ezra, O. K. Faull, S. Jbabdi, and K. T. Pattinson, "Connectivity-based segmentation of the periaqueductal gray matter in human with brainstem optimized diffusion MRI," *Hum Brain Mapp*, vol. 36, no. 9, pp. 3459–71, 2015.

[144] Z. M. Saygin, D. E. Osher, J. Augustinack, B. Fischl, and J. D. Gabrieli, "Connectivity-based segmentation of human amygdala nuclei using probabilistic tractography," *Neuroimage*, vol. 56, no. 3, pp. 1353–61, 2011.

[145] T. E. Behrens, H. Johansen-Berg, M. W. Woolrich, S. M. Smith, C. A. Wheeler-Kingshott, P. A. Boulby, G. J. Barker, E. L. Sillery, K. Sheehan, O. Ciccarelli, A. J. Thompson, J. M. Brady, and P. M. Matthews, "Non-invasive mapping of connections between human thalamus and cortex using diffusion imaging," *Nat Neurosci*, vol. 6, no. 7, pp. 750–7, 2003.

[146] M. Hernández, G. D. Guerrero, J. M. Cecilia, J. M. García, A. Inuggi, S. Jbabdi, T. E. Behrens, and S. N. Sotiropoulos, "Accelerating fibre orientation estimation from diffusion weighted magnetic resonance imaging using GPUs," *PLoS One*, vol. 8, no. 4, p. e61892, 2013.

[147] M. Hernandez-Fernandez, I. Reguly, S. Jbabdi, M. Giles, S. Smith, and S. N. Sotiropoulos, "Using GPUs to accelerate computational diffusion MRI: From microstructure estimation to tractography and connectomes," *Neuroimage*, vol. 188, pp. 598–615, 2019.

[148] K. Setsompop, R. Kimmlingen, E. Eberlein, T. Witzel, J. Cohen-Adad, J. A. McNab, B. Keil, M. D. Tisdall, P. Hoecht, P. Dietz, S. F. Cauley, V. Tountcheva, V. Matschl, V. H. Lenz, K. Heberlein, A. Potthast, H. Thein, J. Van Horn, A. Toga, F. Schmitt, D. Lehne, B. R. Rosen, V. Wedeen, and L. L. Wald, "Pushing the limits of in vivo diffusion MRI for the Human Connectome Project," *Neuroimage*, vol. 80, pp. 220–33, 2013.

[149] Q. Fan, T. Witzel, A. Nummenmaa, K. R. A. Van Dijk, J. D. Van Horn, M. K. Drews, L. H. Somerville, M. A. Sheridan, R. M. Santillana, J. Snyder, T. Hedden, E. E. Shaw, M. O.

Hollinshead, V. Renvall, R. Zanzonico, B. Keil, S. Cauley, J. R. Polimeni, D. Tisdall, R. L. Buckner, V. J. Wedeen, L. L. Wald, A. W. Toga, and B. R. Rosen, "MGH-USC Human Connectome Project datasets with ultra-high b-value diffusion MRI," *NeuroImage*, vol. 124, no. Pt B, pp. 1108–1114, 2016.

[150] T. Hope, L. T. Westlye, and A. Bjørnerud, "The effect of gradient sampling schemes on diffusion metrics derived from probabilistic analysis and tract-based spatial statistics," *Magnetic Resonance Imaging*, vol. 30, no. 3, pp. 402–412, 2012.

[151] D. C. Van Essen, S. M. Smith, D. M. Barch, T. E. J. Behrens, E. Yacoub, and K. Ugurbil, "The WU-Minn Human Connectome Project: An overview," *NeuroImage*, vol. 80, pp. 62–79, 2013.

[152] K. V. Haak, A. F. Marquand, and C. F. Beckmann, "Connectopic mapping with resting-state fMRI," *NeuroImage*, vol. 170, pp. 83–94, 2018.

[153] P. Jezzard and S. Clare, "Sources of distortion in functional MRI data," *Human Brain Mapping*, vol. 8, no. 2-3, pp. 80–85, 1999.

[154] C. A. Olman, L. Davachi, and S. Inati, "Distortion and signal loss in medial temporal lobe," *PLOS ONE*, vol. 4, no. 12, p. e8160, 2009.

[155] N. Weiskopf, C. Hutton, O. Josephs, and R. Deichmann, "Optimal EPI parameters for reduction of susceptibility-induced BOLD sensitivity losses: A whole-brain analysis at 3 T and 1.5 T," *NeuroImage*, vol. 33, no. 2, pp. 493–504, 2006.

[156] S. Clare, S. Francis, P. G. Morris, and R. Bowtell, "Single-shot T measurement to establish optimum echo time for fMRI: Studies of the visual, motor, and auditory cortices at 3.0 T," *Magnetic Resonance in Medicine*, vol. 45, no. 5, pp. 930–933, 2001.

[157] P. E. Yoo, S. E. John, S. Farquharson, J. O. Cleary, Y. T. Wong, A. Ng, C. B. Mulcahy, D. B. Grayden, R. J. Ordidge, N. L. Opie, T. J. O'Brien, T. J. Oxley, and B. A. Moffat, "7T-fMRI: Faster temporal resolution yields optimal BOLD sensitivity for functional network imaging specifically at high spatial resolution," *NeuroImage*, vol. 164, pp. 214–229, 2018.

[158] C. F. Schmidt, N. Degonda, R. Luechinger, K. Henke, and P. Boesiger, "Sensitivity-encoded (SENSE) echo planar fMRI at 3T in the medial temporal lobe," *NeuroImage*, vol. 25, no. 2, pp. 625–641, 2005.

[159] J. P. Stockmann and L. L. Wald, "In vivo B0 field shimming methods for MRI at 7T," *NeuroImage*, vol. 168, pp. 71–87, 2018.

[160] S. Ogawa, R. S. Menon, D. W. Tank, S. G. Kim, H. Merkle, J. M. Ellermann, and K. Ugurbil, "Functional brain mapping by blood oxygenation level-dependent contrast magnetic resonance imaging. a comparison of signal characteristics with a biophysical model," *Biophysical Journal*, vol. 64, no. 3, pp. 803–812, 1993.

[161] P. A. Bandettini, E. C. Wong, A. Jesmanowicz, R. S. Hinks, and J. S. Hyde, "Spin-echo and gradient-echo epi of human brain activation using bold contrast: A comparative study at 1.5 T," *NMR in Biomedicine*, vol. 7, no. 1-2, pp. 12–20, 1994.

[162] R. Weisskoff, C. S. Zuo, J. L. Boxerman, and B. R. Rosen, "Microscopic susceptibility variation and transverse relaxation: Theory and experiment," *Magnetic Resonance in Medicine*, vol. 31, no. 6, pp. 601–610, 1994.

[163] E. Yacoub, T. Q. Duong, P. F. Van De Moortele, M. Lindquist, G. Adriany, S. G. Kim, K. Uğurbil, and X. Hu, "Spin-echo fMRI in humans using high spatial resolutions and high magnetic fields," *Magn Reson Med*, vol. 49, no. 4, pp. 655–64, 2003.

[164] J. Budde, G. Shajan, M. Zaitsev, K. Scheffler, and R. Pohmann, "Functional MRI in human subjects with gradient-echo and spin-echo EPI at 9.4 T," *Magnetic Resonance in Medicine*, vol. 71, no. 1, pp. 209–218, 2014.

[165] D. G. Norris, "Spin-echo fMRI: The poor relation?" *Neuroimage*, vol. 62, no. 2, pp. 1109–15, 2012.

[166] F. De Martino, S. Schmitter, M. Moerel, J. Tian, K. Ugurbil, E. Formisano, E. Yacoub, and P.-F. v. de Moortele, "Spin echo functional MRI in bilateral auditory cortices at 7T: An application of B1 shimming," *NeuroImage*, vol. 63, no. 3, pp. 1313–1320, 2012.

[167] A. Barghoorn, B. Riemenschneider, J. Hennig, and P. LeVan, "Improving the sensitivity of spin-echo fMRI at 3T by highly accelerated acquisitions," *Magnetic Resonance in Medicine*, vol. 86, no. 1, pp. 245–257, 2021.

[168] D. Berron, P. Vieweg, A. Hochkeppler, J. B. Pluta, S. L. Ding, A. Maass, A. Luther, L. Xie, S. R. Das, D. A. Wolk, T. Wolbers, P. A. Yushkevich, E. Düzel, and L. E. M. Wisse, "A protocol for manual segmentation of medial temporal lobe subregions in 7Tesla MRI,"

NeuroImage: Clinical, vol. 15, pp. 466–482, 2017.

[169] D. Sederevičius, D. Vidal-Piñeiro, Sørensen, K. van Leemput, J. E. Iglesias, A. V. Dalca, D. N. Greve, B. Fischl, A. Bjørnerud, K. B. Walhovd, and A. M. Fjell, "Reliability and sensitivity of two whole-brain segmentation approaches included in FreeSurfer – ASEG and SAMSEG," *NeuroImage*, vol. 237, p. 118113, 2021.

[170] R. L. Brunsing, N. M. Schenker-Ahmed, N. S. White, J. K. Parsons, C. Kane, J. Kuperman, H. Bartsch, A. K. Kader, R. Rakow-Penner, T. M. Seibert, D. Margolis, S. S. Raman, C. R. McDonald, N. Farid, S. Kesari, D. Hansel, A. Shabaik, A. M. Dale, and D. S. Karow, "Restriction spectrum imaging: An evolving imaging biomarker in prostate MRI," *Journal of Magnetic Resonance Imaging*, vol. 45, no. 2, pp. 323–336, 2017.

[171] S. Suo, X. Chen, L. Wu, X. Zhang, Q. Yao, Y. Fan, H. Wang, and J. Xu, "Non-Gaussian water diffusion kurtosis imaging of prostate cancer," *Magnetic Resonance Imaging*, vol. 32, no. 5, pp. 421–427, 2014.

[172] L. J. Edens, K. H. White, P. Jevtic, X. Li, and D. L. Levy, "Nuclear size regulation: from single cells to development and disease," *Trends Cell Biol*, vol. 23, no. 4, pp. 151–9, 2013.

[173] N. S. White and A. M. Dale, "Distinct effects of nuclear volume fraction and cell diameter on high b-value diffusion MRI contrast in tumors," *Magn Reson Med*, vol. 72, no. 5, pp. 1435–43, 2014.

[174] J. L. Ulmer, C. V. Salvan, W. M. Mueller, H. G. Krouwer, G. O. Stroe, A. Aralasmak, and R. W. Prost, "The role of diffusion tensor imaging in establishing the proximity of tumor borders to functional brain systems: Implications for preoperative risk assessments and postoperative outcomes," *Technology in Cancer Research & Treatment*, vol. 3, no. 6, pp. 567–576, 2004.

[175] T. Schonberg, P. Pianka, T. Hendler, O. Pasternak, and Y. Assaf, "Characterization of displaced white matter by brain tumors using combined DTI and fMRI," *NeuroImage*, vol. 30, no. 4, pp. 1100–1111, 2006.

[176] D. J. Werring, C. A. Clark, G. J. Barker, D. H. Miller, G. J. M. Parker, M. J. Brammer, E. T. Bullmore, V. P. Giampietro, and A. J. Thompson, "The structural and functional

mechanisms of motor recovery: complementary use of diffusion tensor and functional magnetic resonance imaging in a traumatic injury of the internal capsule," *Journal of Neurology, Neurosurgery & Psychiatry*, vol. 65, no. 6, pp. 863–869, 1998.

[177] M. Bouts, C. Möller, A. Hafkemeijer, J. C. van Swieten, E. Dopper, W. M. van der Flier, H. Vrenken, A. M. Wink, Y. A. L. Pijnenburg, P. Scheltens, F. Barkhof, T. M. Schouten, F. de Vos, R. A. Feis, J. van der Grond, M. de Rooij, and S. Rombouts, "Single subject classification of Alzheimer's disease and behavioral variant frontotemporal dementia using anatomical, diffusion tensor, and resting-state functional magnetic resonance imaging," *J Alzheimers Dis*, vol. 62, no. 4, pp. 1827–1839, 2018.

[178] D. J. Werring, C. A. Clark, G. J. M. Parker, D. H. Miller, A. J. Thompson, and G. J. Barker, "A direct demonstration of both structure and function in the visual system: Combining diffusion tensor imaging with functional magnetic resonance imaging," *NeuroImage*, vol. 9, no. 3, pp. 352–361, 1999.

[179] P. Hagmann, L. Cammoun, X. Gigandet, R. Meuli, C. J. Honey, V. J. Wedeen, and O. Sporns, "Mapping the structural core of human cerebral cortex," *PLOS Biology*, vol. 6, no. 7, p. e159, 2008.

[180] S. J. Teipel, A. L. W. Bokde, T. Meindl, E. Amaro, J. Soldner, M. F. Reiser, S. C. Herpertz, H.-J. Möller, and H. Hampel, "White matter microstructure underlying default mode network connectivity in the human brain," *NeuroImage*, vol. 49, no. 3, pp. 2021–2032, 2010.

[181] M. A. Koch, D. G. Norris, and M. Hund-Georgiadis, "An investigation of functional and anatomical connectivity using magnetic resonance imaging," *NeuroImage*, vol. 16, no. 1, pp. 241–250, 2002.

[182] C. J. Honey, O. Sporns, L. Cammoun, X. Gigandet, J. P. Thiran, R. Meuli, and P. Hagmann, "Predicting human resting-state functional connectivity from structural connectivity," *Proceedings of the National Academy of Sciences*, vol. 106, no. 6, pp. 2035–2040, 2009.

[183] A. Messé, H. Benali, and G. Marrelec, "Relating structural and functional connectivity in MRI: a simple model for a complex brain," *IEEE Trans Med Imaging*, vol. 34, no. 1, pp. 27–37, 2015.

[184] H. Huang and M. Ding, "Linking functional connectivity and structural connectivity quantitatively: A comparison of methods," *Brain Connect*, vol. 6, no. 2, pp. 99–108, 2016.

[185] L. J. O'Donnell, L. Rigolo, I. Norton, W. M. Wells, C.-F. Westin, and A. J. Golby, "fMRI-DTI modeling via landmark distance atlases for prediction and detection of fiber tracts," *NeuroImage*, vol. 60, no. 1, pp. 456–470, 2012.

[186] F. D. Bowman, L. Zhang, G. Derado, and S. Chen, "Determining functional connectivity using fMRI data with diffusion-based anatomical weighting," *NeuroImage*, vol. 62, no. 3, pp. 1769–1779, 2012.

[187] F. Calamante, R. A. J. Masterton, J.-D. Tournier, R. E. Smith, L. Willats, D. Raffelt, and A. Connelly, "Track-weighted functional connectivity (TW-FC): A tool for characterizing the structural–functional connections in the brain," *NeuroImage*, vol. 70, pp. 199–210, 2013.

[188] D. Zhu, T. Zhang, X. Jiang, X. Hu, H. Chen, N. Yang, J. Lv, J. Han, L. Guo, and T. Liu, "Fusing DTI and fMRI data: A survey of methods and applications," *NeuroImage*, vol. 102, pp. 184–191, 2014.

[189] P. J. Broser, S. Groeschel, T.-K. Hauser, K. Lidzba, and M. Wilke, "Functional MRI-guided probabilistic tractography of cortico-cortical and cortico-subcortical language networks in children," *NeuroImage*, vol. 63, no. 3, pp. 1561–1570, 2012.

[190] G. Douaud, N. Filippini, S. Knight, K. Talbot, and M. R. Turner, "Integration of structural and functional magnetic resonance imaging in amyotrophic lateral sclerosis," *Brain*, vol. 134, no. 12, pp. 3470–3479, 2011.

[191] A. A. Fingelkurts, A. A. Fingelkurts, and S. Kähkönen, "Functional connectivity in the brain—is it an elusive concept?" *Neuroscience & Biobehavioral Reviews*, vol. 28, no. 8, pp. 827–836, 2005.

[192] K. J. Friston, "Functional and effective connectivity in neuroimaging: A synthesis," *Human Brain Mapping*, vol. 2, no. 1-2, pp. 56–78, 1994.

[193] M. Gilson, R. Moreno-Bote, A. Ponce-Alvarez, P. Ritter, and G. Deco, "Estimation of directed effective connectivity from fMRI functional connectivity hints at asymme-

tries of cortical connectome," *PLOS Computational Biology*, vol. 12, no. 3, p. e1004762, 2016.

[194] C. Li, M. Chen, S. Li, X. Zhao, C. Zhang, M. Liu, and C. Zhou, "Diffusion tensor imaging of prostate at 3.0 Tesla," *Acta Radiologica*, vol. 52, no. 7, pp. 813–817, 2011.

[195] W. Tian, J. Zhang, F. Tian, J. Shen, T. Niu, G. He, and H. Yu, "Correlation of diffusion tensor imaging parameters and Gleason scores of prostate cancer," *Experimental and therapeutic medicine*, vol. 15, no. 1, pp. 351–356, 2018.

[196] N. Gholizadeh, P. B. Greer, J. Simpson, J. Denham, P. Lau, J. Dowling, H. Hondermarck, and S. Ramadan, "Characterization of prostate cancer using diffusion tensor imaging: A new perspective," *European Journal of Radiology*, vol. 110, pp. 112–120, 2019.

[197] C. Magnon, S. J. Hall, J. Lin, X. Xue, L. Gerber, S. J. Freedland, and P. S. Frenette, "Autonomic nerve development contributes to prostate cancer progression," *Science*, vol. 341, no. 6142, p. 1236361, 2013.

[198] A. Olar, D. He, D. Florentin, Y. Ding, and G. Ayala, "Biologic correlates and significance of axonogenesis in prostate cancer," *Human Pathology*, vol. 45, no. 7, pp. 1358–1364, 2014.

[199] I. F. Syversen, K. M. Bakke, E. Grøvik, A. Negård, S. H. Holmedal, L. G. Lyckander, K. I. Gjesdal, S. Meltzer, and K. Røe Redalen, "PO-0983: Prediction of chemoradiotherapy response in rectal cancer using static and dynamic R2* MRI," *Radiotherapy and Oncology*, vol. 127, p. S545, 2018.

[200] K. M. Bakke, S. Meltzer, E. Grøvik, A. Negård, S. H. Holmedal, K. I. Gjesdal, A. Bjørnerud, A. H. Ree, and K. R. Redalen, "Sex differences and tumor blood flow from dynamic susceptibility contrast MRI are associated with treatment response after chemoradiation and long-term survival in rectal cancer," *Radiology*, vol. 297, no. 2, pp. 352–360, 2020.

[201] F. Sardanelli, C. Boetes, B. Borisch, T. Decker, M. Federico, F. J. Gilbert, T. Helbich, S. H. Heywang-Köbrunner, W. A. Kaiser, M. J. Kerin, R. E. Mansel, L. Marotti, L. Martincich, L. Mauriac, H. Meijers-Heijboer, R. Orecchia, P. Panizza, A. Ponti, A. D. Purushotham, P. Regitnig, M. R. Del Turco, F. Thibault, and R. Wilson, "Magnetic resonance imaging of the breast: Recommendations from the EUSOMA working group," *European Journal of Cancer*, vol. 46, no. 8, pp. 1296–1316, 2010.

[202] I. Vidić, L. Egnell, N. P. Jerome, N. S. White, R. Karunamuni, R. Rakow-Penner, A. M. Dale, T. F. Bathen, and P. E. Goa, "Modeling the diffusion-weighted imaging signal for breast lesions in the b = 200 to 3000 s/mm2 range: quality of fit and classification accuracy for different representations," *Magnetic Resonance in Medicine*, vol. 84, no. 2, pp. 1011–1023, 2020.

[203] M. M. S. Andreassen, A. E. Rodríguez-Soto, C. C. Conlin, I. Vidić, T. M. Seibert, A. M. Wallace, S. Zare, J. Kuperman, B. Abudu, G. S. Ahn, M. Hahn, N. P. Jerome, A. Østlie, T. F. Bathen, H. Ojeda-Fournier, P. E. Goa, R. Rakow-Penner, and A. M. Dale, "Discrimination of breast cancer from healthy breast tissue using a three-component diffusion-weighted MRI model," *Clinical Cancer Research*, vol. 27, no. 4, pp. 1094–1104, 2021.

[204] J. Oudeman, A. J. Nederveen, G. J. Strijkers, M. Maas, P. R. Luijten, and M. Froeling, "Techniques and applications of skeletal muscle diffusion tensor imaging: A review," *Journal of Magnetic Resonance Imaging*, vol. 43, no. 4, pp. 773–788, 2016.

[205] L. S. Krimer, T. M. Hyde, M. M. Herman, and R. C. Saunders, "The entorhinal cortex: an examination of cyto- and myeloarchitectonic organization in humans," *Cerebral Cortex*, vol. 7, no. 8, pp. 722–731, 1997.

[206] B. Mädler, S. A. Drabycz, S. H. Kolind, K. P. Whittall, and A. L. MacKay, "Is diffusion anisotropy an accurate monitor of myelination?: Correlation of multicomponent T2 relaxation and diffusion tensor anisotropy in human brain," *Magnetic Resonance Imaging*, vol. 26, no. 7, pp. 874–888, 2008.

Papers

Paper I

PLOS ONE

RESEARCH ARTICLE

Exploring the diagnostic potential of adding T2 dependence in diffusion-weighted MR imaging of the prostate

Ingrid Framås Syversen[1]*, Mattijs Elschot[2,3], Elise Sandsmark[3], Helena Bertilsson[4,5], Tone Frost Bathen[2], Pål Erik Goa[6]

1 Kavli Institute for Systems Neuroscience, NTNU, Norwegian University of Science and Technology, Trondheim, Norway, **2** Department of Circulation and Medical Imaging, NTNU, Norwegian University of Science and Technology, Trondheim, Norway, **3** Department of Radiology and Nuclear Medicine, St. Olavs Hospital, Trondheim University Hospital, Trondheim, Norway, **4** Department of Urology, St. Olavs Hospital, Trondheim University Hospital, Trondheim, Norway, **5** Department of Clinical and Molecular Medicine, NTNU, Norwegian University of Science and Technology, Trondheim, Norway, **6** Department of Physics, NTNU, Norwegian University of Science and Technology, Trondheim, Norway

* ingrid.f.syversen@ntnu.no

Citation: Syversen IF, Elschot M, Sandsmark E, Bertilsson H, Bathen TF, Goa PE (2021) Exploring the diagnostic potential of adding T2 dependence in diffusion-weighted MR imaging of the prostate. PLoS ONE 16(5): e0252387. https://doi.org/10.1371/journal.pone.0252387

Editor: Pascal A. T. Baltzer, Medical University of Vienna, AUSTRIA

Received: March 1, 2021

Accepted: May 14, 2021

Published: May 27, 2021

Peer Review History: PLOS recognizes the benefits of transparency in the peer review process; therefore, we enable the publication of all of the content of peer review and author responses alongside final, published articles. The editorial history of this article is available here: https://doi.org/10.1371/journal.pone.0252387

Data Availability Statement: The minimal dataset underlying this study is available in the paper and its Supporting Information. Imaging data cannot be shared publicly because the data contain potentially

Abstract

Background

Magnetic resonance imaging (MRI) is essential in the detection and staging of prostate cancer. However, improved tools to distinguish between low-risk and high-risk cancer are needed in order to select the appropriate treatment.

Purpose

To investigate the diagnostic potential of signal fractions estimated from a two-component model using combined T2- and diffusion-weighted imaging (T2-DWI).

Material and methods

62 patients with prostate cancer and 14 patients with benign prostatic hyperplasia (BPH) underwent combined T2-DWI (TE = 55 and 73 ms, b-values = 50 and 700 s/mm^2) following clinical suspicion of cancer, providing a set of 4 measurements per voxel. Cancer was confirmed in post-MRI biopsy, and regions of interest (ROIs) were delineated based on radiology reporting. Signal fractions of the slow component (SF_{slow}) of the proposed two-component model were calculated from a model fit with 2 free parameters, and compared to conventional bi- and mono-exponential apparent diffusion coefficient (ADC) models.

Results

All three models showed a significant difference (p<0.0001) between peripheral zone (PZ) tumor and normal tissue ROIs, but not between non-PZ tumor and BPH ROIs. The area under the receiver operating characteristics curve distinguishing tumor from prostate voxels was 0.956, 0.949 and 0.949 for the two-component, bi-exponential and mono-exponential

identifying or sensitive patient information. Access to experimental data are available through the research administration manager at NTNU (Norwegian University of Science and Technology), kontakt@isb.ntnu.no.

Funding: - IFS: Norwegian University of Science and Technology, https://www.ntnu.no/ (project number 81850040). - ME: The liaison Committee between the Central Norway Regional Health Authority and the Norwegian University of Science and Technology, https://helse-midt.no/samarbeidsorganet (grant number 90265300). - TFB: The Research Council of Norway, https://www.forskningsradet.no/ (grant number 295013). The funders had no role in study design, data collection and analysis, decision to publish, or preparation of the manuscript.

Competing interests: The authors have declared that no competing interests exist.

models, respectively. The corresponding Spearman correlation coefficients between tumor values and Gleason Grade Group were fair (0.370, 0.499 and -0.490), but not significant.

Conclusion

Signal fraction estimates from a two-component model based on combined T2-DWI can differentiate between tumor and normal prostate tissue and show potential for prostate cancer diagnosis. The model performed similarly to conventional diffusion models.

Introduction

Magnetic resonance imaging (MRI) has been essential in the detection and staging of prostate cancer for several years [1, 2]. Different sequences are performed, where T2-weighted and diffusion-weighted imaging (DWI) constitute the basis of such a diagnostic protocol [3]. Prostate cancer is usually detected as homogeneous moderately hypointense focal areas on T2-weighted images, with a relatively low apparent diffusion coefficient (ADC). The Prostate Imaging-Reporting and Data System (PI-RADS) guidelines are used to detect clinically significant cancer, based on a combination of DWI, T2-weighted imaging and also dynamic contrast-enhanced (DCE) MRI [3]. For peripheral zone (PZ) cancers, DWI is the dominant factor for determining the PI-RADS score, while for non-PZ cancers, T2-weighted images are predominantly used. However, despite these standardized guidelines, the accuracy of detecting and staging clinically significant cancer is still variable, and overtreatment is a major problem [4–6]. Improved diagnostic tools are needed in order to better stratify patients to active surveillance or radical treatment. In addition, it can be challenging to separate between non-PZ cancers and benign prostatic hyperplasia (BPH) with low ADC, as these have similar imaging characteristics [7].

Low ADC in the prostate is commonly interpreted as restricted diffusion due to densely packed cells in tumor tissue [8]. However, this simplification does not consider the different mechanisms of the underlying tissue microstructure. One suggested extension to this is the bi-exponential model, which consists of a slow diffusion component representing the restricted diffusion within cells, and a fast diffusion component representing extracellular water [9]. This model has shown promising results in previous studies [10, 11].

Another common assumption is that T2 values and ADCs are independent of each other. However, studies have shown an interdependence of these parameters which appears to differ between tumor, normal prostate tissue and BPH [12–14], which could potentially be exploited for diagnosis. By performing DWI at different echo times (TE), it is possible to isolate the signal from subvoxel populations of water molecules with specific paired T2 values and ADCs associated with different components of the prostate. A three-component model using this principle has been suggested [15]. However, for such a model to be clinically feasible, it needs to have a relatively short acquisition time and a low computational cost. A simpler two-component model fulfills these requirements and would be consistent with a simple representation of the prostate: Water in the glandular lumen with long T2 and a high ADC, and water inside the cells with a shorter T2 and lower ADC [12].

In this work, we estimate signal fractions in a slow and a fast diffusion component using combined T2- and diffusion-weighted imaging (T2-DWI), and compare these between tumor, normal tissue and BPH in order to investigate the diagnostic potential of the model.

Materials and methods

Patients

76 patients underwent an extended MRI exam as part of the integrated cancer care pathway following prostate cancer suspicion. Of these, 62 patients had post-MRI biopsy-confirmed cancer and were assigned randomly to a training and a test set (see Table 1 for details). The inclusion criteria were tumor in any prostate zone that both had a PI-RADS and a location-matched Gleason score. The 14 included patients without detected cancer had BPH lesions, characterized by visually low ADC and a negative biopsy. An overview of the patient and case selection process can be found in the S1 Fig. The study was approved by the Regional Committee for Medical and Health Research Ethics Central Norway (identifier REK 2017/520), and all participants provided written informed consent before enrollment.

MRI protocol

Imaging was performed on a 3T MRI scanner (Magnetom Skyra, Siemens Medical Systems, Erlangen, Germany) using body surface coils. The combined T2-DWI was added at the end of a clinical protocol.

Table 1. Summary of patient characteristics for the 62 included patients with biopsy-confirmed cancer.

Parameter	Training set	Test set
Number of patients	31	31
PSA level (ng/mL)	11.0 ± 8.6	11.4 ± 15.7
PI-RADS score		
2	2	2
3	7	5
4	8	6
5	14	18
Gleason Grade Group		
1	6	4
2	7	15
3	10	5
4	4	3
5	4	4
Cancer location		
PZ	25	24
TZ	3	4
CZ	1	0
AFMS	2	3
Treatment		
RARP	15	14
Radiation therapy	8	7
Hormone therapy	2	1
Active surveillance	6	9

PSA = prostate-specific antigen, PI-RADS = Prostate Imaging-Reporting and Data System, PZ = peripheral zone, TZ = transition zone, CZ = central zone, AFMS = anterior fibromuscular stroma, RARP = robotic assisted radical prostatectomy.

Note—Data are numbers of patients, except for PSA level which is given as mean ± standard deviation. There were 2 and 7 missing PSA values in the training and test set, respectively. The Gleason Grade Group is based on biopsy scores after MRI, except for the patients who underwent RARP, where the histopathological Gleason Grade Group was used. Note that the tumors might extend over multiple prostatic zones, and that the cancer location denoted is the primary tumor location.

https://doi.org/10.1371/journal.pone.0252387.t001

The transversal combined T2-DWI acquisition consisted of two fat-suppressed, single-shot, monopolar spin-echo echo-planar imaging (EPI) sequences with TE = 55 and 73 ms, respectively. Each of these sequences had repetition time (TR) = 4200 ms, b-values = 50 and 700 s/mm^2 (three directions; number of excitations (NEX) = 2 and 4, respectively), resolution = 2.0×2.0×3.0 mm^3, field of view = 256×256 mm^2, imaging and reconstruction matrix = 128×128, 26 slices, generalized autocalibrating partial parallel acquisition (GRAPPA) factor 2 and acquisition time 1:38 minutes. The only differences between the sequences at the two TEs were the diffusion times and gradient amplitudes: at TE = 55 ms, δ = 11.6 ms and Δ = 23.9 ms, while at TE = 73 ms, δ = 20.6 ms and Δ = 32.9 ms. This protocol provides a 2×2 matrix of trace-weighted diffusion measurements for each voxel, where each measurement is associated with a different combination of TE and b-values.

Preprocessing

All analyses were performed using MATLAB (version R2019b, MathWorks, Natick, MA, USA) unless stated otherwise. Code used for model fitting is available on GitHub at https://github.com/ntnu-mr-cancer/T2-DWI.

The trace-weighted images at each TE and b-value were co-registered to the image with the lowest TE and b-value with Elastix, using a multiresolution rigid registration scheme [16, 17]. The scanner's autogenerated ADC map for TE = 73 ms was also co-registered to the same image because the regions of interest (ROIs) were to be delineated on this map. To only correct for potential motion of the prostate and not of other internal structures, a box-shaped ROI covering the prostate was defined for each patient and used as a mask for the co-registration.

ROI delineation. For each cancer patient, one tumor ROI was manually delineated using ITK-SNAP (www.itksnap.org) [18] on the scanner's autogenerated ADC map for TE = 73 ms, with corresponding T2-weighted images used for support. The delineation was performed based on the clinical radiologist's PI-RADS annotation and the tumor ROI was characterized by focal low ADC under (or around) 1000 μm^2/ms. All tumor ROI locations were confirmed to be cancer by matching with biopsy reports in the patient journal, and cross-checked with histology slides if available (n = 29). For the PZ tumor patients, one normal tissue ROI was also delineated, characterized by visually high ADC in the PZ (around 2000 μm^2/ms). For both the tumor and normal tissue ROIs, respectively, only one tumor lesion or normal area were considered per ROI. For each BPH patient, one ROI was manually delineated of one or more proliferative BPH nodule(s) with visually low ADC (under/around 1000 μm^2/ms) in the non-PZ, also visible as a nodule on T2-weighted images. All ROIs were delineated by a basic scientist (IFS, 1 year of experience in prostate MRI) and validated by a radiology resident (ES, 1 year of experience in prostate MRI, supervised by an experienced radiologist).

Two-component model

We modeled the MR signal as water in two separate components: a slow diffusion component with low ADC and short T2, and a fast component with high ADC and long T2. Thus, the 2×2 matrix of signal intensities SI from the combined T2-DWI were fitted to the following equation:

$$\frac{SI}{SI_0} = SF_{slow}\ exp\left(-\frac{TE}{T2_{slow}}\right) exp(-b * ADC_{slow}) + SF_{fast}\ exp\left(-\frac{TE}{T2_{fast}}\right) exp(-b * ADC_{fast}), \quad (1)$$

where the subscripts "slow" and "fast" denote the values of slow and fast components, respectively. SI_0 is the signal intensity at TE = 0 and b = 0, SF is the signal fraction of the components, and

SF_{slow}+SF_{fast} = 1. In order to reduce the number of free parameters in the model, ADC_{slow} = 0.3 μm^2/ms and ADC_{fast} = 2.6 μm^2/ms globally optimized for a biophysically similar bi-exponential model were used [19]. This results in four free parameters (SI_0, SF_{slow}, $T2_{slow}$, $T2_{fast}$) to the four measurements.

$T2_{slow}$ and $T2_{fast}$ were then globally optimized for the entire population of voxels across all patients in the training set by minimizing a global cost function while fitting the 2×2 signal to Eq 1 using a range of T2 values determined from a previous preliminary study [20]. The cost function was defined as the sum of the root-mean-square error (RMSE) of the fit of all included voxels. By keeping $T2_{slow}$ and $T2_{fast}$ fixed for each iteration, only two parameters were fitted for each voxel in this process. The optimal T2 values were then used for further analysis, where the two remaining free parameters SI_0 and SF_{slow} were determined on a voxel-by-voxel basis by fitting the 2×2 signal to the two-component model for all included patients.

All voxels inside the box-shaped ROIs were analyzed. The average size of the box ROIs was approximately 167,000 voxels. However, to reduce noise effects, voxels were excluded that had a value equal to or below three times the noise floor, defined as the average signal intensity of background voxels. Voxels with an apparent negative ADC or T2 value were also excluded. On average, approximately 10% of the voxels in the tumor, normal and BPH ROIs were excluded.

Bi-exponential model

For comparison, we also investigated a purely ADC-dependent bi-exponential model:

$$\frac{SI}{SI_0} = SF_{slow}\ exp(-b * ADC_{slow}) + SF_{fast}\ exp(-b * ADC_{fast}), \quad (2)$$

where SF_{slow}+SF_{fast} = 1, ADC_{slow} = 0.3 μm^2/ms and ADC_{fast} = 2.6 μm^2/ms as in the two-component model [19]. SI_0 and SF_{slow} were fitted to the two b-value measurements at TE = 73 ms.

Mono-exponential ADC

Using

$$\frac{SI}{SI_0} = exp(-b * ADC), \quad (3)$$

SI_0 and ADC were fitted to the two b-value measurements at TE = 73 ms.

An extended analysis with even more model comparisons can be found in the S1 Appendix.

Statistical analysis

The first part of the statistical analysis was divided into PZ and non-PZ tumors. Note that all PZ analyses were performed on the test set only, while the non-PZ analyses were carried out on all available patients due to the low sample size. For the PZ analyses, the Wilcoxon signed-rank test was used to test for statistical significance between mean SF_{slow} (for both the two-component and bi-exponential models) and ADC of the tumor and normal tissue ROIs (n = 24). For the non-PZ analyses, BPH ROIs from the BPH patients (n = 14) were used for comparison with the non-PZ tumor ROIs (n = 13), and the Mann-Whitney U test was used to test for statistical significance between these. All tests were two-sided. After a Bonferroni correction for 9 multiple comparisons (including the correlation described in the following paragraph), $p<0.006$ was considered statistically significant.

The remainder of the statistical analyses were carried out on the whole test set with both PZ and non-PZ tumors together. Voxel-wise receiver operating characteristics (ROC) analysis

was performed comparing the SF_{slow} and ADCs in the tumor ROIs with the rest of the area inside the box-shaped ROIs. Note that although the ROC analysis was performed only on the test set, the optimal threshold value was calculated from the training set and applied on the test set in the calculation of sensitivity and specificity. Furthermore, the Spearman correlation coefficient (ρ) was calculated between the mean SF_{slow} and ADC of the tumor ROIs and the Gleason Grade Group.

Results

The optimal T2 values for the two-component model were determined to be $T2_{slow}$ = 45 ms and $T2_{fast}$ = 180 ms (Fig 1).

Box plots of estimated SF_{slow} (for both the two-component and bi-exponential models) and ADC for different ROIs are shown in Fig 2. In the PZ analyses, all metrics show a significance between tumor and normal ROIs. In the non-PZ analyses, no metrics show a significant difference between the tumor and BPH ROIs, although the two-component model yields the lowest p-value.

Fig 3 shows examples of calculated SF_{slow} and ADC maps for PZ and non-PZ tumors and BPH, as well as corresponding histology slides for the PZ and non-PZ tumors and a T2-weighted image for the BPH case. SF_{slow} (for both the two-component and bi-exponential models) and ADC yield good tumor conspicuity for both tumor cases. In the BPH case, the lesion is visible both on the SF_{slow} maps and the ADC map, although with a slightly lower contrast than the tumors.

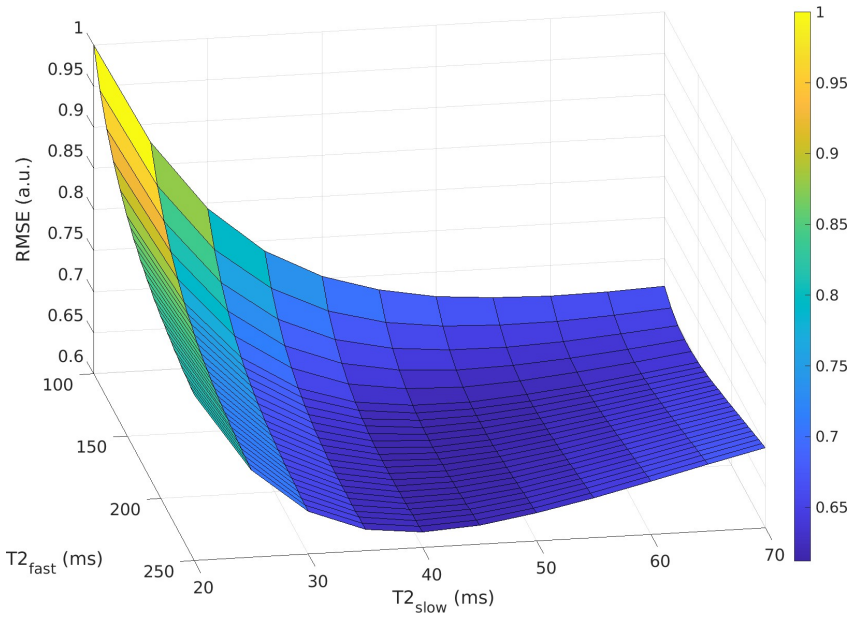

Fig 1. Surface curve showing the total root-mean-square error (RMSE) from fitting the two-component model with a range of $T2_{slow}$ and $T2_{fast}$ values for the training set, scaled so that the highest RMSE equals 1. The total RMSE is at a minimum for $T2_{slow}$ = 45 ms and $T2_{fast}$ = 180 ms.

https://doi.org/10.1371/journal.pone.0252387.g001

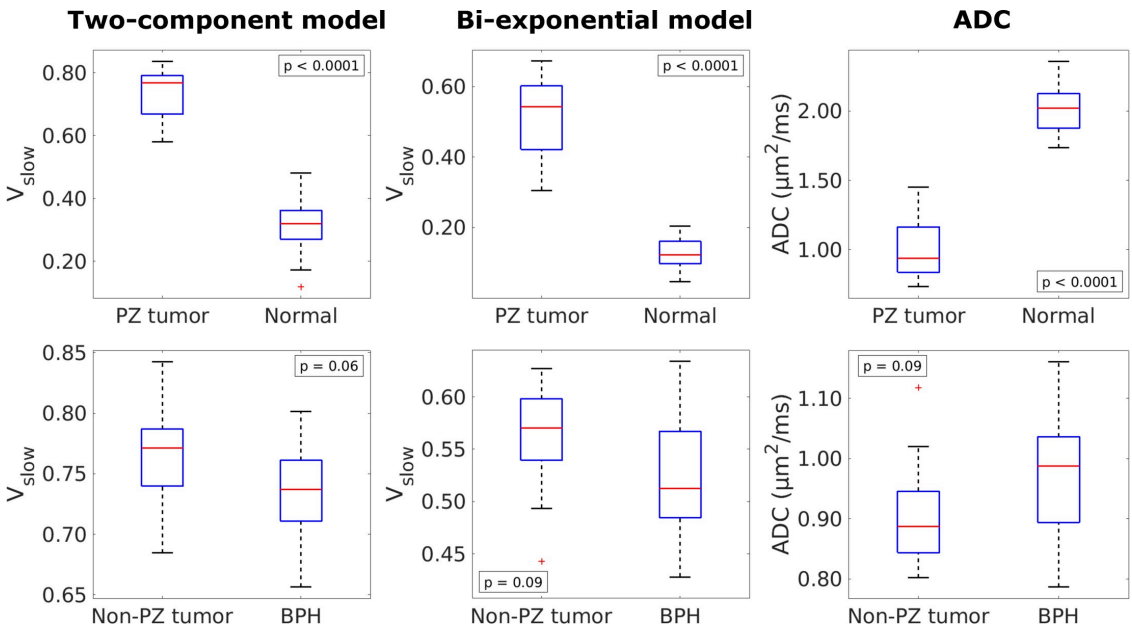

Fig 2. Box plots showing the distribution of mean SF_{slow} (from the two-component and bi-exponential models) and ADC of the different ROIs. Upper row: PZ tumors (n = 24) compared to normal tissue (n = 24). Bottom row: Non-PZ tumors (n = 13) compared to BPH (n = 14). $p<0.006$ was considered statistically significant.

https://doi.org/10.1371/journal.pone.0252387.g002

ROC curves and results from the ROC analysis are shown in Fig 4 and Table 2, respectively, and show that SF_{slow} (for both the two-component and bi-exponential model) and ADC have very good diagnostic performance. However, although the sensitivity, specificity and area under the ROC curve (AUC) are very similar for all metrics, SF_{slow} from the two-exponential model yields slightly higher values than the other two, which are nearly identical to each other. Note the very different optimal threshold values for SF_{slow} from the two-exponential and bi-exponential models of 0.67 and 0.42, respectively. This means that $\geq$67% and 42% of the voxels should be in the SF_{slow} components to be classified as tumor tissue. In the case of ADC, the value needs to be under the respective optimal threshold to be classified as tumor.

In Fig 5, the mean SF_{slow} and ADC from the tumor ROIs are plotted as a function of Gleason Grade Group. The Spearman correlation coefficient was found to be $\rho = 0.370$ ($p = 0.040$) and $\rho = 0.499$ ($p = 0.004$) for SF_{slow} for the two-component and bi-exponential model, respectively, and $\rho = -0.490$ ($p = 0.005$) for ADC.

Discussion

In this study, 62 patients with prostate cancer and 14 patients with BPH underwent combined T2-DWI. From this, signal fractions were estimated using a two-component model based on both T2 and ADC dependence. The purpose was to investigate the diagnostic potential of this model in comparison with results from conventional diffusion models. Our results show that SF_{slow} from the two-component model is higher in PZ tumors than in normal tissue, and in non-PZ tumors than in BPH, although only significant in the former case. SF_{slow} shows good diagnostic properties and a fair correlation with tumor aggressiveness.

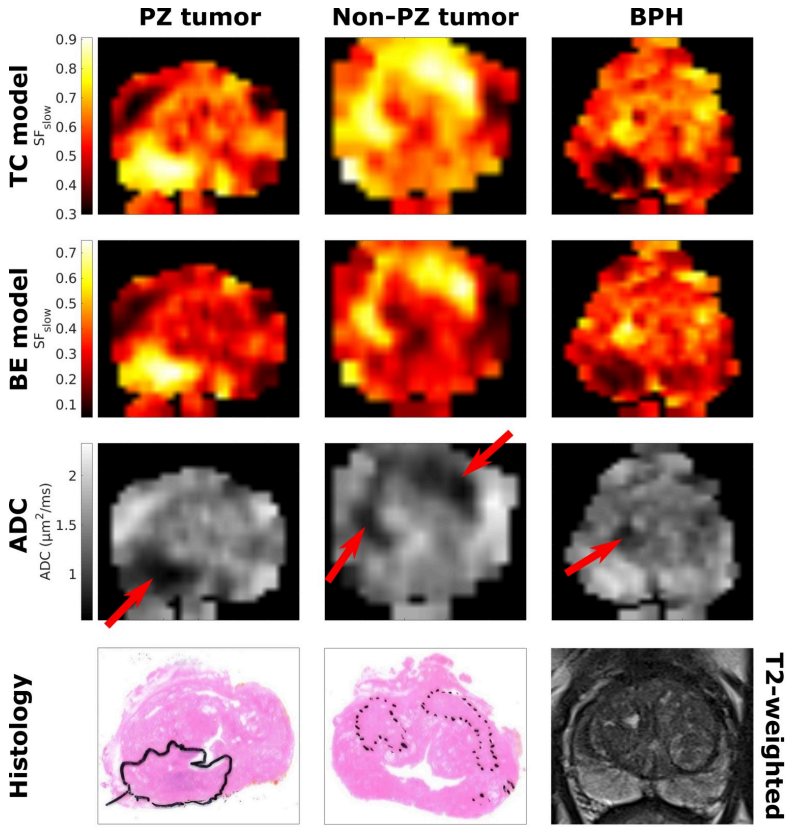

Fig 3. Examples of estimated value maps for three different patients. SF_{slow} (from the two-component (TC) and bi-exponential (BE) models) maps and corresponding ADC map are shown for a PZ tumor patient, a non-PZ tumor patient and a BPH patient, respectively. For the tumor patients, histology slides are also shown for comparison, while a corresponding T2-weighted image is shown in the BPH case as histology was not available for this patient. The lesions are denoted on the ADC maps with red arrows. On the histology slides, the PZ tumor is denoted with a solid line, while the non-PZ tumors are denoted with dotted lines. Example maps from more cases can be found in the S2 Fig.

https://doi.org/10.1371/journal.pone.0252387.g003

Global T2 optimization was performed both to reduce the number of free variables and to isolate components with distinct, paired ADC and T2 values. Comparing the results with a model fit with the T2 values as free variables (see S1 Table) showed the benefit of optimizing the T2 values in advance. To further reduce the number of free variables, the ADCs were adapted from a bi-exponential model [19]. The signal fraction estimates for the slow component in that paper were markedly lower than our SF_{slow} estimates from the two-component model, but closer to the values obtained with our bi-exponential model, indicating a dependence of SF_{slow} on T2. This implies that the two-component and bi-exponential models do not isolate identical subvoxel populations of water molecules, because the added T2 dependence actively tunes the diffusion signal from the prostate tissue, in agreement with other studies performed with combined T2-DWI [12–14]. A previous three-component model based on combined T2-DWI estimated the T2 values of the epithelium, stroma and lumen to be 50 ms, 80

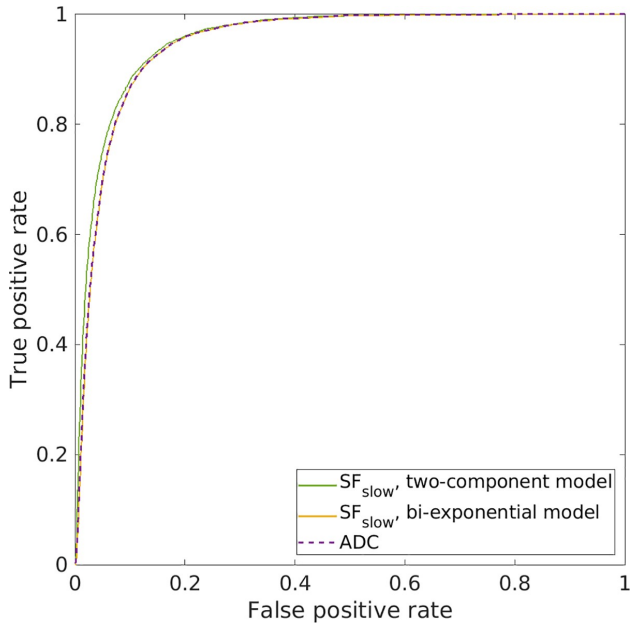

Fig 4. ROC curves for SF_{slow} (for the two-component model in green and for the bi-exponential model in yellow) and ADC (in dashed purple). Voxels within tumor ROIs (n = 6569) were compared with voxels outside (n = 254,112).

https://doi.org/10.1371/journal.pone.0252387.g004

ms and 665 ms, respectively [15], which would suggest that our slow component is approximately equivalent to the epithelium, whereas the fast component is a mixture of stroma and lumen.

The two-component model performed similarly to the bi-exponential model and the mono-exponential ADC. All three models showed a highly significant difference between PZ tumors and normal tissue, and while no significant differences were found between non-PZ tumors and BPH, the two-component model performed slightly better than the others in that case. In the ROC analysis, where all three models showed an excellent diagnostic performance, the two-component model also performed marginally better than the other two. However, the bi-exponential model and ADC showed a somewhat better correlation with tumor aggressiveness, although none of them significant. Interestingly, in all the analyses, the bi-exponential model and ADC both show very similar results that are slightly different from the two-component model, which could suggest that our model extracts additional information from the underlying tissue compared to the other models. Although our two-component model

Table 2. Summary of Receiver Operating Characteristics (ROC) results.

Model	AUC	Optimal threshold	Sensitivity (%)	Specificity (%)
SF_{slow}, two-component model	0.956	0.67	92.6	85.8
SF_{slow}, bi-exponential model	0.949	0.42	92.3	85.4
ADC (μm^2/ms)	0.949	1.17	92.3	85.4

AUC = area under curve, SF = signal fraction, ADC = apparent diffusion coefficient.

https://doi.org/10.1371/journal.pone.0252387.t002

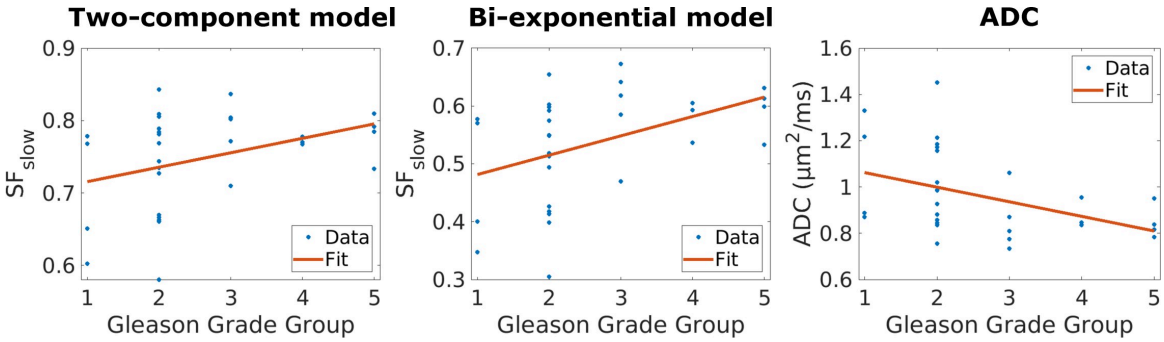

Fig 5. Mean tumor ROI values plotted as a function of Gleason Grade Group (blue dots) for SF_{slow} (from the two-component and bi-exponential models) and ADC. The red line represents the least-square fit to the data.

https://doi.org/10.1371/journal.pone.0252387.g005

performed similarly to conventional models, and not significantly better, the method shows diagnostic promise and should be further optimized and investigated in a larger number of patients, in order to more rigorously evaluate its ability to predict tumor aggressiveness.

One reason for the similar performance between the two-component and bi-exponential models and ADC could be that the tumor, normal tissue and BPH ROIs used in this study were all delineated on ADC maps. Delineating the ROIs based on MR images and not histopathology of prostatectomy specimens can give a bias in the results, such that it is more difficult to see improvements in other models if ADC is used as a reference. Nevertheless, we chose to use radiology for the delineation because including only prostatectomy patients would give a bias towards highly aggressive cancer, as well as reducing the number of patients available. Another reason that the models perform so similarly could be that the bi-exponential model and ADC are calculated at the longest TE. Therefore, they are also implicitly influenced by the T2 relaxation of the tissue to a higher degree than if the shorter TE was used. However, we chose to use TE = 73 ms since this was TE closest to the one used in [19]. A calculation with TE = 55 ms is carried out in the S1 Table for comparison.

We show that SF_{slow} from the two-component model has diagnostic potential in prostate cancer. Some might argue that a more complex model would give a better representation of the underlying tissue microstructure, but our focus was to apply a model that would be feasible in a clinical setting, where time is a limiting factor. Our T2-DWI protocol had a comparable acquisition time to that of a standard clinical prostate DWI sequence, and there are only two variables to be estimated, given fixed ADCs and T2 values of each signal component. However, these values should be further optimized by exploring a wider range of TEs and b-values, in order to potentially increase the diagnostic performance of the method. Furthermore, since the main focus of our work was to investigate clinical feasibility of the two-component model, we did not perform a thorough evaluation of repeatability and reproducibility, which should also be addressed in the future.

Our study had some limitations. Firstly, the images were not corrected for geometric distortions caused by the EPI sequence, although no severe distortions were noted during visual inspection of the images. Secondly, the sequence parameters of the combined T2-DWI were introduced to see whether there were any effects of varying the TE in DWI, and it was made as short as possible to fit in at the end of a clinical protocol, with TEs and b-values close to clinical DWI parameters. The low number and short range of these parameters limit the sensitivity of the T2 values and ADC of the components. At last, because a standard vendor DWI sequence

was used for the combined T2-DWI, the acquisition at the different TEs had different diffusion times (Δ and δ), which can also affect the apparent TE dependence of ADC [21]. This should be addressed when designing new combined T2-DWI protocols.

In conclusion, signal fraction estimates from a two-component model based on combined T2-DWI can differentiate between PZ tumors and normal prostate tissue and show potential for prostate cancer diagnosis. The model performed similarly to conventional diffusion models. However, the method should be further optimized for clinical purposes and investigated in a larger number of patients.

Supporting information

S1 File. Minimal underlying data. The values (for individual patients/ROIs/voxels) behind the tables and figures, and the statistical measures reported.
(XLSX)

S1 Fig. Patient and ROI selection.
(PDF)

S2 Fig. Examples of estimated value maps for three different patients. SF_{slow} (from the two-component (TC) and bi-exponential (BE) models) maps and corresponding ADC map are shown for a PZ tumor patient, a non-PZ tumor patient and a BPH patient, respectively. For the tumor patients, histology slides are also shown for comparison, while a corresponding T2-weighted image is shown in the BPH case as histology was not available for this patient. The lesions are denoted on the ADC maps with red arrows. On the histology slides, the tumors are denoted with dotted lines.
(DOCX)

S1 Appendix. Supplementary methods.
(DOCX)

S1 Table. Median [95% CI] of the mean region of interest (ROI) values calculated from the different models and parameters. CI = confidence interval, PZ = peripheral zone, BPH = benign prostatic hyperplasia, SF = signal fraction, ADC = apparent diffusion coefficient, TE = echo time. Note—For PZ tumors, tumor ROIs (n = 24) were compared with normal ROIs (n = 24), while for non-PZ tumors, tumor ROIs (n = 13) were compared with BPH ROIs (n = 14). Units are given in parentheses, except for SF_{slow} which is unitless. A p-value$<$0.0019 was considered statistically significant, and the significant results are highlighted in bold.
(DOCX)

Acknowledgments

We thank Sverre Langørgen for help with radiologic assessment. We also want to thank Kjerstin Olaussen, Torill E. Sjøbakk, Mohammed R. S. Sunoqrot and Daniel Chen Billdal for help with data collection and organization.

Author Contributions

Conceptualization: Ingrid Framås Syversen, Mattijs Elschot, Tone Frost Bathen, Pål Erik Goa.

Formal analysis: Ingrid Framås Syversen.

Funding acquisition: Mattijs Elschot, Tone Frost Bathen, Pål Erik Goa.

Investigation: Ingrid Framås Syversen, Elise Sandsmark.

Methodology: Ingrid Framås Syversen, Pål Erik Goa.

Project administration: Tone Frost Bathen, Pål Erik Goa.

Resources: Pål Erik Goa.

Software: Ingrid Framås Syversen.

Supervision: Pål Erik Goa.

Validation: Elise Sandsmark, Helena Bertilsson.

Visualization: Ingrid Framås Syversen.

Writing – original draft: Ingrid Framås Syversen.

Writing – review & editing: Ingrid Framås Syversen, Mattijs Elschot, Elise Sandsmark, Helena Bertilsson, Tone Frost Bathen, Pål Erik Goa.

References

1. Mazaheri Y, Shukla-Dave A, Muellner A, Hricak H. MRI of the prostate: clinical relevance and emerging applications. J Magn Reson Imaging. 2011; 33(2):258–74. https://doi.org/10.1002/jmri.22420 PMID: 21274967
2. Akin O, Gultekin DH, Vargas HA, Zheng J, Moskowitz C, Pei X, et al. Incremental value of diffusion weighted and dynamic contrast enhanced MRI in the detection of locally recurrent prostate cancer after radiation treatment: preliminary results. Eur Radiol. 2011; 21(9):1970–8. https://doi.org/10.1007/s00330-011-2130-6 PMID: 21533634
3. Barentsz JO, Weinreb JC, Verma S, Thoeny HC, Tempany CM, Shtern F, et al. Synopsis of the PI-RADS v2 guidelines for multiparametric prostate magnetic resonance imaging and recommendations for use. Eur Urol. 2016; 69(1):41–9. https://doi.org/10.1016/j.eururo.2015.08.038 PMID: 26361169
4. Fütterer JJ, Briganti A, De Visschere P, Emberton M, Giannarini G, Kirkham A, et al. Can clinically significant prostate cancer be detected with multiparametric magnetic resonance imaging? A systematic review of the literature. Eur Urol. 2015; 68(6):1045–53. https://doi.org/10.1016/j.eururo.2015.01.013 PMID: 25656808
5. Kobus T, Vos PC, Hambrock T, De Rooij M, Hulsbergen-Van de Kaa CA, Barentsz JO, et al. Prostate cancer aggressiveness: in vivo assessment of MR spectroscopy and diffusion-weighted imaging at 3 T. Radiology. 2012; 265(2):457–67. https://doi.org/10.1148/radiol.12111744 PMID: 22843767
6. Westphalen AC, McCulloch CE, Anaokar JM, Arora S, Barashi NS, Barentsz JO, et al. Variability of the positive predictive value of PI-RADS for prostate MRI across 26 centers: experience of the Society of Abdominal Radiology Prostate Cancer Disease-focused Panel. Radiology. 2020; 296(1):76–84. https://doi.org/10.1148/radiol.2020190646 PMID: 32315265
7. Hoeks CM, Hambrock T, Yakar D, Hulsbergen-van de Kaa CA, Feuth T, Witjes JA, et al. Transition zone prostate cancer: detection and localization with 3-T multiparametric MR imaging. Radiology. 2013; 266(1):207–17. https://doi.org/10.1148/radiol.12120281 PMID: 23143029
8. Issa B. In vivo measurement of the apparent diffusion coefficient in normal and malignant prostatic tissues using echo-planar imaging. J Magn Reson Imaging. 2002; 16(2):196–200. https://doi.org/10.1002/jmri.10139 PMID: 12203768
9. Mulkern RV, Barnes AS, Haker SJ, Hung YP, Rybicki FJ, Maier SE, et al. Biexponential characterization of prostate tissue water diffusion decay curves over an extended b-factor range. Magn Reson Imaging. 2006; 24(5):563–8. https://doi.org/10.1016/j.mri.2005.12.008 PMID: 16735177
10. Shinmoto H, Oshio K, Tanimoto A, Higuchi N, Okuda S, Kuribayashi S, et al. Biexponential apparent diffusion coefficients in prostate cancer. Magn Reson Imaging. 2009; 27(3):355–9. https://doi.org/10.1016/j.mri.2008.07.008 PMID: 18768281
11. Egnell L, Vidić I, Jerome NP, Bofin AM, Bathen TF, Goa PE. Stromal collagen content in breast tumors correlates with in vivo diffusion-weighted imaging: a comparison of multi b-value DWI with histologic specimen from benign and malignant breast lesions. J Magn Reson Imaging. 2020; 51(6):1868–78. https://doi.org/10.1002/jmri.27018 PMID: 31837076

12. Wang S, Peng Y, Medved M, Yousuf AN, Ivancevic MK, Karademir I, et al. Hybrid multidimensional T2 and diffusion-weighted MRI for prostate cancer detection. J Magn Reson Imaging. 2014; 39(4):781–8. https://doi.org/10.1002/jmri.24212 PMID: 23908146

13. Sadinski M, Karczmar G, Peng Y, Wang S, Jiang Y, Medved M, et al. Pilot study of the use of hybrid multidimensional T2-weighted imaging-DWI for the diagnosis of prostate cancer and evaluation of Gleason score. AJR Am J Roentgenol. 2016; 207(3):592–8. https://doi.org/10.2214/AJR.15.15626 PMID: 27352026

14. Ma X, Chen H, Peng Y. Hybrid T2-weighted and diffusion-weighted magnetic resonance imaging for differentiating prostate cancer from benign prostatic hyperplasia. 10th International Congress on Image and Signal Processing, BioMedical Engineering and Informatics; Oct. 14–16; Shanghai. Piscataway: IEEE; 2017. p. 1–5. https://doi.org/10.1109/CISP-BMEI.2017.8302193

15. Chatterjee A, Bourne RM, Wang S, Devaraj A, Gallan AJ, Antic T, et al. Diagnosis of prostate cancer with noninvasive estimation of prostate tissue composition by using hybrid multidimensional MR imaging: a feasibility study. Radiology. 2018; 287(3):864–73. https://doi.org/10.1148/radiol.2018171130 PMID: 29393821

16. Klein S, Staring M, Murphy K, Viergever MA, Pluim JPW. elastix: a toolbox for intensity-based medical image registration. IEEE Trans Med Imaging. 2010; 29(1):196–205. https://doi.org/10.1109/TMI.2009.2035616 PMID: 19923044

17. Shamonin D, Bron E, Lelieveldt B, Smits M, Klein S, Staring M. Fast parallel image registration on CPU and GPU for diagnostic classification of Alzheimer's disease. Front Neuroinform. 2014; 7(50):1–15. https://doi.org/10.3389/fninf.2013.00050 PMID: 24474917

18. Yushkevich PA, Piven J, Hazlett HC, Smith RG, Ho S, Gee JC, et al. User-guided 3D active contour segmentation of anatomical structures: Significantly improved efficiency and reliability. Neuroimage. 2006; 31(3):1116–28. https://doi.org/10.1016/j.neuroimage.2006.01.015 PMID: 16545965

19. Karunamuni RA, Kuperman J, Seibert TM, Schenker N, Rakow-Penner R, Sundar VS, et al. Relationship between kurtosis and bi-exponential characterization of high b-value diffusion-weighted imaging: application to prostate cancer. Acta Radiol. 2018; 59(12):1523–9. https://doi.org/10.1177/0284185118770889 PMID: 29665707

20. Syversen IF, Elschot M, Bathen TF, Goa PE. Two-component model of prostate tissue using hybrid multidimensional T2 and diffusion-weighted imaging. ISMRM & SMRT Virtual Conference & Exhibition; 2020 Aug 8–14: ISMRM.

21. Kim S, Chi-Fishman G, Barnett AS, Pierpaoli C. Dependence on diffusion time of apparent diffusion tensor of ex vivo calf tongue and heart. Magn Reson Med. 2005; 54(6):1387–96. https://doi.org/10.1002/mrm.20676 PMID: 16265644

S1 Fig. Patient and ROI selection

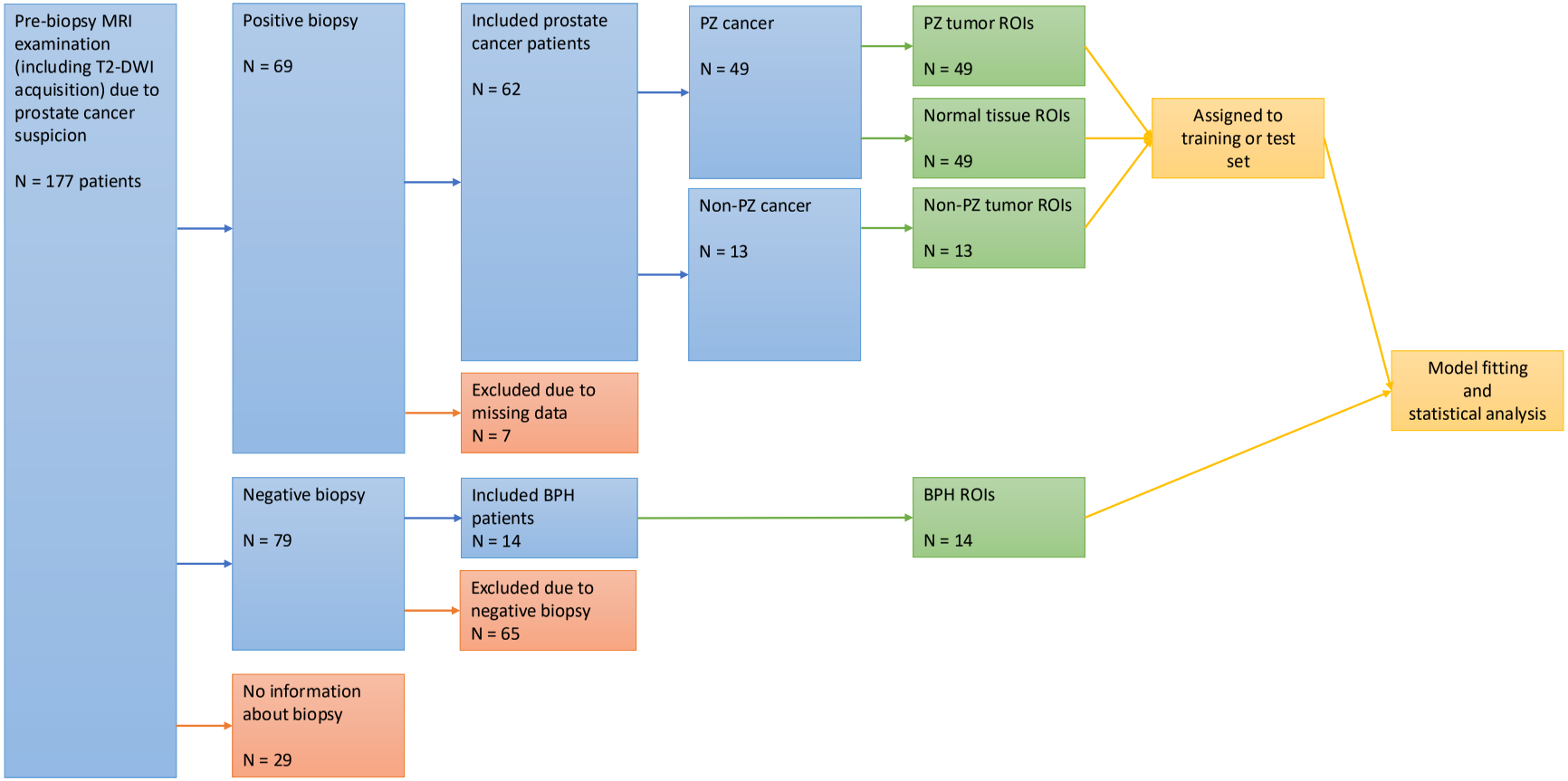

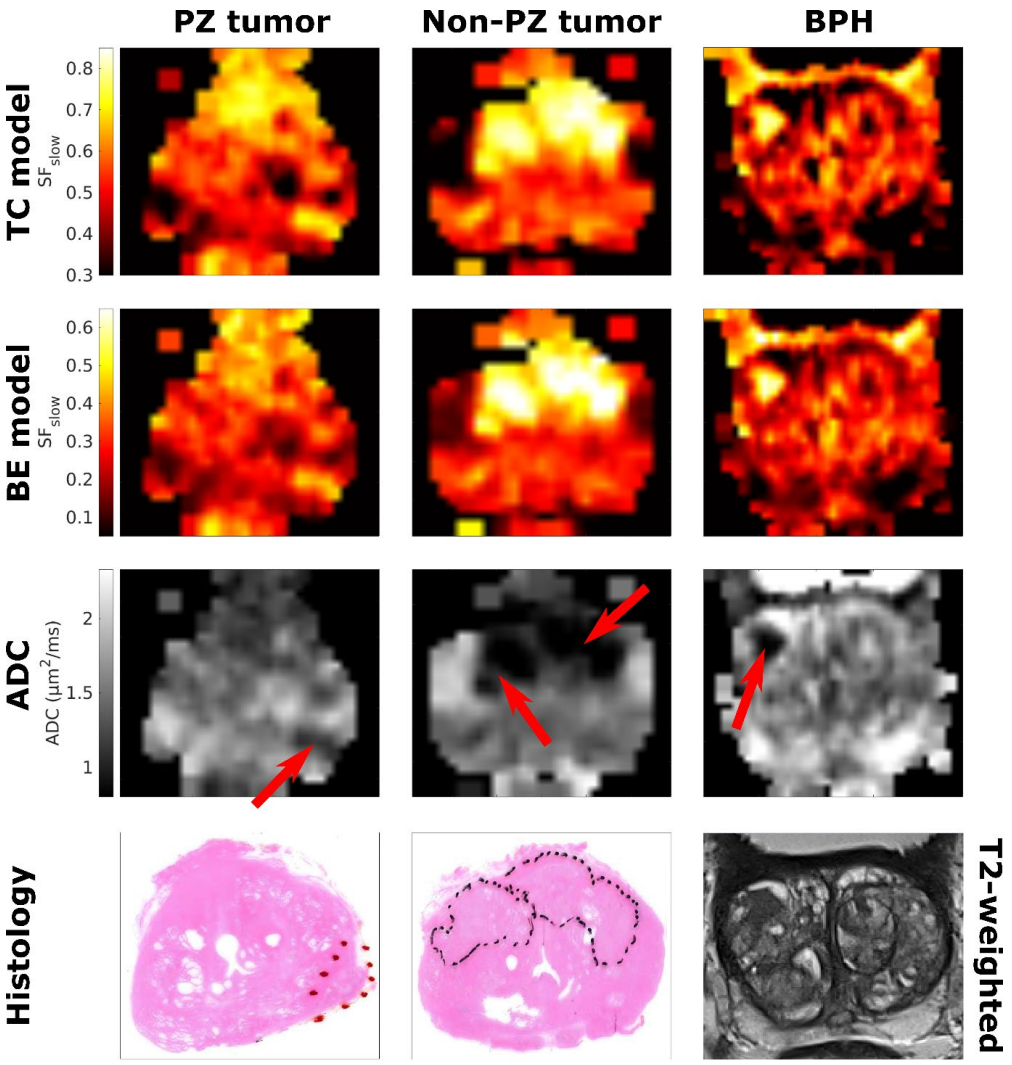

S2 Fig. Examples of estimated value maps for three different patients. SF_{slow} (from the two-component (TC) and bi-exponential (BE) models) maps and corresponding ADC map are shown for a PZ tumor patient, a non-PZ tumor patient and a BPH patient, respectively. For the tumor patients, histology slides are also shown for comparison, while a corresponding T2-weighted image is shown in the BPH case as histology was not available for this patient. The lesions are denoted on the ADC maps with red arrows. On the histology slides, the tumors are denoted with dotted lines.

S1 Appendix

Supplementary methods

Alternative models

To evaluate the individual effects of ADC and T2 on the two-component model, we extended the analysis and compared the results with signal fractions from three alternative models.

First, to investigate the effect of globally optimizing the T2 values, we fitted the two-component model,

$$\frac{SI}{SI_0} = SF_{slow}\, exp\left(-\frac{TE}{T2_{slow}}\right) exp(-b * ADC_{slow}) + SF_{fast}\, exp\left(-\frac{TE}{T2_{fast}}\right) exp\left(-b * ADC_{fast}\right), \quad (1)$$

with no constraints on the T2 values. Also here, we set SF_{slow}+SF_{fast}=1, ADC_{slow}=0.3 μm^2/ms and ADC_{fast}=2.6 μm^2/ms (19). This leaves four free parameters (SI_0, SF_{slow}, $T2_{slow}$, $T2_{fast}$) to be fitted to the four measurements.

The second one was an ADC-dependent bi-exponential model, but at TE=55 ms:

$$\frac{SI}{SI_0} = SF_{slow}\, exp(-b * ADC_{slow}) + SF_{fast}\, exp\left(-b * ADC_{fast}\right), \quad (2)$$

where SF_{slow}+SF_{fast}=1, ADC_{slow}=0.3 μm^2/ms and ADC_{fast}=2.6 μm^2/ms as in the two-component model (19). SI_0 and SF_{slow} were fitted to the two b-value measurements at TE=55 ms.

The third model was a T2-dependent bi-exponential model:

$$\frac{SI}{SI_0} = SF_{slow}\, exp\left(-\frac{TE}{T2_{slow}}\right) + SF_{fast}\, exp\left(-\frac{TE}{T2_{fast}}\right), \quad (3)$$

with SF_{slow}+SF_{fast}=1, where we used the globally optimized $T2_{slow}$ and $T2_{fast}$ from the two-component model. SI_0 and SF_{slow} were fitted to the two TE measurements at b=50 s/mm^2 and b=700 s/mm^2 separately.

ADC and T2

For comparison, we also calculated the ADC at TE=55 ms, and T2 values at both b-values. Using

$$\frac{SI}{SI_0} = exp(-b * ADC), \quad (4)$$

SI_0 and ADC were fitted to the two b-value measurements at TE=55 ms. Similarly, using

$$\frac{SI}{SI_0} = exp\left(-\frac{TE}{T2}\right), \quad (5)$$

SI_0 and T2 were fitted to the two TE measurements at b=50 s/mm^2 and b=70 s/mm^2 separately.

Furthermore, the changes in ADC and T2 as a function of TE and b-value, respectively, were also calculated to see how they affect each other.

Statistical analysis

The statistical analyses were divided into PZ and non-PZ tumors. Note that all PZ analyses were performed on the test set only, while the non-PZ analyses were carried out on all patients due to the low sample size.

The 9 metrics subject to statistical analyses were as following: SF_{slow} for the four alternative model calculations; ADC at TE=55 ms and T2 at both b-values; and the change in T2 values and ADCs as a function of b-value and TE, respectively. For the PZ analyses, the Wilcoxon signed-rank test was used to test for statistical significance between the tumor and normal tissue ROIs (n=24). For the non-PZ analyses, BPH ROIs from the BPH patients (n=14) were used for comparison with the non-PZ tumor ROIs (n=13), and the Mann-Whitney U test was used to test for statistical significance between these. All tests were two-sided. After a

Bonferroni correction for 27 multiple comparisons (including the analyses in the main manuscript), $p<0.0019$ was considered statistically significant.

All results (including the metrics from the main manuscript) are shown in S1 Table.

S1 Table. Median [95% CI] of the mean region of interest (ROI) values calculated from the different models and parameters

Model	PZ tumors			Non-PZ tumors		
	Tumor	Normal	p-value	Tumor	BPH	p-value
SF_{slow}, T2-ADC two-component model	0.77 [0.67, 0.79]	0.32 [0.28, 0.36]	**< 0.0001**	0.77 [0.73, 0.80]	0.74 [0.68, 0.78]	0.06
SF_{slow}, T2-ADC two-component model, no T2 constraints	0.48 [0.44, 0.53]	0.34 [0.29, 0.37]	**< 0.0001**	0.47 [0.36, 0.60]	0.47 [0.35, 0.56]	0.58
SF_{slow}, ADC-dependent bi-exponential model, TE=55 ms	0.54 [0.43, 0.58]	0.17 [0.13, 0.20]	**< 0.0001**	0.54 [0.46, 0.60]	0.49 [0.46, 0.56]	0.30
SF_{slow}, ADC-dependent bi-exponential model, TE=73 ms	0.54 [0.43, 0.60]	0.12 [0.10, 0.16]	**< 0.0001**	0.57 [0.51, 0.60]	0.51 [0.44, 0.59]	0.09
SF_{slow}, T2-dependent bi-exponential model, b=50 s/mm^2	0.68 [0.62, 0.73]	0.14 [0.09, 0.31]	**< 0.0001**	0.79 [0.45, 0.94]	0.68 [0.51, 0.84]	0.25
SF_{slow}, T2-dependent bi-exponential model, b=700 s/mm^2	0.66 [0.59, 0.73]	0.53 [0.47, 0.78]	0.0164	0.70 [0.55, 0.92]	0.66 [0.44, 0.76]	0.58
ADC, TE=55 ms (µm^2/ms)	0.94 [0.86, 1.14]	1.86 [1.75, 1.98]	**< 0.0001**	0.94 [0.85, 1.09]	1.03 [0.91, 1.09]	0.32
ADC, TE=73 ms (µm^2/ms)	0.94 [0.84, 1.16]	2.02 [1.88, 2.11]	**< 0.0001**	0.89 [0.83, 1.00]	0.99 [0.85, 1.12]	0.09
Change in ADC (%)	0.81 [-5.14, 2.96]	8.53 [5.47, 10.32]	**0.0002**	-6.17 [-8.53, 2.15]	-2.38 [-8.83, 3.35]	0.72
T2, b-value=50 s/mm^2 (ms)	81 [75, 90]	247 [154, 302]	**0.0002**	69 [48, 189]	81 [61, 113]	0.40
T2, b-value=700 s/mm^2 (ms)	86 [74, 106]	127 [72, 159]	0.0093	111 [51, 166]	85 [75, 148]	0.68
Change in T2 (%)	1 [-6, 30]	-50 [-53, -38]	**0.0001**	17 [1, 66]	13 [-6, 44]	0.58

CI = confidence interval, PZ = peripheral zone, BPH = benign prostatic hyperplasia, SF = signal fraction, ADC = apparent diffusion coefficient, TE = echo time.
Note—For PZ tumors, tumor ROIs (n=24) were compared with normal ROIs (n=24), while for non-PZ tumors, tumor ROIs (n=13) were compared with BPH ROIs (n=14). Units are given in parentheses, except for SF_{slow} which is unitless. A p-value<0.0019 was considered statistically significant, and the significant results are highlighted in bold.

Paper II

Structural connectivity-based segmentation of the human entorhinal cortex

Ingrid Framås Syversen[1]*, Menno P. Witter[1], Asgeir Kobro-Flatmoen[1], Pål Erik Goa[2], Tobias Navarro Schröder[1†], Christian F. Doeller[1,3†]

[1]Kavli Institute for Systems Neuroscience, NTNU – Norwegian University of Science and Technology, Trondheim, Norway

[2]Department of Physics, NTNU – Norwegian University of Science and Technology, Trondheim, Norway

[3]Max Planck Institute for Human Cognitive and Brain Sciences, Leipzig, Germany

*Corresponding author

[†]Senior authors

Abstract

The medial (MEC) and lateral entorhinal cortex (LEC), widely studied in rodents, are well defined and characterized. In humans, however, the exact locations of their homologues remain uncertain. Previous functional magnetic resonance imaging (fMRI) studies have subdivided the human EC into posteromedial (pmEC) and anterolateral (alEC) parts, but uncertainty remains about the choice of imaging modality and seed regions, in particular in light of a substantial revision of the classical model of EC connectivity based on novel insights from rodent anatomy. Here, we used structural, not functional imaging, namely diffusion tensor imaging (DTI) and probabilistic tractography to segment the human EC based on differential connectivity to other brain regions known to project selectively to MEC or LEC. We defined MEC as more strongly connected with presubiculum and retrosplenial cortex (RSC), and LEC as more strongly connected with distal CA1 and proximal subiculum (dCA1pSub) and orbitofrontal cortex (OFC). Although our DTI segmentation had a larger medial-lateral component than in the previous fMRI studies, our results show that the human MEC and LEC homologues have a border oriented both towards the posterior-anterior and medial-lateral axes, supporting the differentiation between pmEC and alEC.

Keywords: MRI, DTI, diffusion tensor imaging, structural connectivity, entorhinal cortex, MEC, LEC, segmentation, subregions

1 Introduction

The entorhinal cortex (EC) is a part of the medial temporal lobe, and a central structure for memory formation and navigation (Eichenbaum et al., 2007; Moser and Moser, 2013; Suzuki and Eichenbaum, 2000). It is classically viewed as a hub for processing and relaying information from the neocortex to the hippocampus, and vice versa (Buzsáki, 1996; Lavenex and Amaral, 2000). The EC can be divided into two main subregions – 'medial' entorhinal cortex (MEC) and 'lateral' entorhinal cortex (LEC) – which differ in both functional properties and connectivity with other regions (Canto et al., 2008; Kerr et al., 2007; van Strien et al., 2009). Both the function and anatomy of the EC subregions have been widely studied in rodents and non-human primates. Based mainly on research in rodents, the MEC is associated with spatial processing in a global, allocentric frame of reference, given the prevalence of spatially modulated cells such as grid and head direction cells (Fyhn et al., 2004; Hafting et al., 2005; Høydal et al., 2019; Knierim et al., 2014). In contrast, the LEC contains cells that are sensitive to the presence of objects in a local frame of reference or processing of time (Deshmukh and Knierim, 2011; Knierim et al., 2014; Tsao et al., 2013; Tsao et al., 2018). However, although recent years have seen a stark increase in functional imaging studies of the human EC (Bellmund et al., 2019; Chen et al., 2019; Montchal et al., 2019; Maass et al., 2015; Navarro Schröder et al., 2015; Reagh and Yassa, 2014; Schultz et al., 2012), the exact locations of the human homologues of MEC and LEC remain somewhat uncertain. This is an ongoing challenge for functional studies of the EC in humans and also makes it difficult to conduct translational research on the origins of neurodegenerative processes such as occurring in Alzheimer's disease, which starts in the EC and transentorhinal area (Braak and Braak, 1992).

In anatomical and functional studies of the human brain, magnetic resonance imaging (MRI) has become an invaluable tool. Functional MRI (fMRI) studies have shown that the properties of the rodent and non-human primate EC also apply to the human EC (Doeller et al., 2010; Reagh and Yassa, 2014; Schultz et al., 2012). Based on the subdivision of the rodent EC into MEC and LEC, studies have tried to localize their respective homologue regions in humans. Previous fMRI studies tested connectivity 'fingerprints' of EC subregions to other parts of the brain. Studies in rodents and non-human primates have demonstrated a largely similar organization of EC connectivity across species (Canto et al., 2008), thus predicting distinct fMRI connectivity fingerprints for the two subregions in humans as well. The resulting delineations of putative human homologue regions of the rodent MEC and LEC were labeled posteromedial EC (pmEC) and anterolateral EC (alEC), based on the outcome of two independent fMRI studies that tested local and global connectivity, respectively (Maass et al., 2015; Navarro Schröder et al., 2015). However, it remains unclear whether the

results were affected by the nature of the imaging modality (fMRI) or the choice of seed brain regions used to identify the subregions.

In addition to the neuroimaging modality, the second reason for a re-evaluation has gained additional importance since the assumption about EC connectivity on which parts of the previous fMRI studies (Maass et al., 2015; Navarro Schröder et al., 2015) were based has been recently revised. For years, the existence of two parallel cortical connectivity streams through the EC has been the accepted model (Nilssen et al., 2019; Ranganath and Ritchey, 2012; Witter et al., 2017). This comprises one pathway into the hippocampus via the parahippocampal/postrhinal cortex (PHC/POR) and MEC (the “where” pathway), and a parallel pathway via the perirhinal cortex (PRC) and LEC (the “what” pathway). However, recent evidence substantially challenged this view. Doan and colleagues found that POR in rats, which corresponds to the PHC in humans, does also project to LEC. These authors further argue that existing data in monkeys substantiate this notion (Doan et al., 2019). This is in line with new findings in humans indicating that the hippocampal-entorhinal-neocortical connections are far more complex than a pure segregation into “where” and “what” pathways (Huang et al., 2021).

In order to identify the human homologues of MEC and LEC, we should take advantage of known unique connections to each subregion. For example, in rodents the presubiculum projects almost exclusively to MEC, whereas distal CA1 and proximal subiculum (dCA1pSub, i.e. the border region between CA1 and subiculum) project most strongly to LEC (Caballero-Bleda and Witter, 1993; Honda and Ishizuka, 2004; Witter and Amaral, 1991; Witter and Amaral, 2021). Meanwhile, the retrosplenial cortex (RSC) and the posterolateral orbitofrontal cortex (OFC) are respectively selectively connected with MEC and LEC (Hoover and Vertes, 2007; Jones and Witter, 2007; Kondo and Witter, 2014; Saleem et al., 2008; Witter and Amaral, 2021; Wyss and Van Groen, 1992). To investigate the connectivity between these regions, there are several imaging modalities available. An alternative method to the widely used fMRI functional connectivity is to instead study structural connectivity using diffusion tensor imaging (DTI), another type of MRI (Powell et al., 2004; Zeineh et al., 2012). Here, one exploits the diffusion of water molecules inside white matter tracts and uses this to map the paths of these fibers – so-called tractography (Mori et al., 1999; Mori and Zhang, 2006). Mapping DTI connectivity from cortices that project selectively to either EC subregion could provide a novel line of evidence to identify MEC and LEC (Ezra et al., 2015; Máté et al., 2018; Saygin et al., 2011).

The objective of this study is therefore to identify the human homologues of the rodent MEC and LEC using DTI, incorporating the novel insights from rodent anatomy. To achieve this,

we performed probabilistic tractography on high-quality DTI data acquired by the Human Connectome Project (Fan et al., 2016). We identify the EC subregions by analyzing the connectivity from regions of interest (ROIs) that project selectively to either of them and compare these to the results from previous fMRI studies.

2 Materials and methods

2.1 MRI data

Publicly available structural and diffusion MRI data from 35 healthy adults were obtained from the MGH-USC Human Connectome Project database (https://ida.loni.usc.edu, http://db.humanconnectome.org), in line with the MGH-USC HCP Data Agreement. All participants provided written informed consent, and the experiments were approved by the institutional review board of Partners Healthcare (Fan et al., 2016). The data were acquired on a Siemens 3T Connectom scanner with maximum gradient strength of 300 mT/m and slew rate 200 T/m/s (McNab et al., 2013; Setsompop et al., 2013). Structural T1-weighted images were acquired using a 3D magnetization-prepared rapid gradient-echo (MPRAGE) sequence at 1 mm isotropic resolution. Diffusion data were acquired using a spin-echo echo-planar imaging (EPI) sequence at 1.5 mm isotropic resolution, with b-values of 1000 s/mm^2 (64 directions), 3000 s/mm^2 (64 directions), 5000 s/mm^2 (128 directions) and 10,000 s/mm^2 (256 directions). One non-diffusion-weighted (b = 0) image was collected every 14 image volumes.

2.2 Preprocessing

The MRI data were minimally preprocessed by the Human Connectome Project as described in (Fan et al., 2014). In brief, this preprocessing pipeline included gradient nonlinearity correction, motion correction, Eddy current correction and b-vector correction.

2.2.1 Registration

Both structural and diffusion images were brain extracted using the brain mask from running the FreeSurfer (version 7.1.1, https://surfer.nmr.mgh.harvard.edu/) functions *recon-all* and *dt-recon* on the participant's structural and diffusion images, respectively (Fischl et al., 2002; Fischl et al., 2004), before refining the result using the FMRIB Software Library's (FSL; version 5.0.9, http://fsl.fmrib.ox.ac.uk/fsl/) function BET (Jenkinson et al., 2012; Smith, 2002). For the diffusion images, brain extraction and registration were performed on the participant's average b = 1000 image. The individual brain-extracted structural and diffusion images were registered to each other, as well as to the MNI152-09b standard brain template (Fonov et al., 2009), using symmetric non-linear registration in the Advanced Neuroimaging

Toolbox (ANTs; version 2.3.4, http://stnava.github.io/ANTs/) based on mutual information (Avants et al., 2011).

2.2.2 Regions of interest

Regions of interest (ROIs) including the EC, presubiculum, CA1 and subiculum were extracted from the automated cortical and subcortical parcellation obtained from running FreeSurfer's *recon-all* and *segmentHA_T1* functions on the MNI152-09b template (Fischl et al., 2002; Fischl et al., 2004; Iglesias et al., 2015). The EC ROI was further refined by masking it by a probabilistic EC ROI, thresholded at 0.25 from the Jülich-Brain Cytoarchitectonic Atlas (Amunts et al., 2020). Since the resulting EC ROI extended too far posteriorly towards the parahippocampal cortex and laterally beyond the collateral sulcus, we also performed a manual adjustment. We created ROIs of distal CA1/proximal subiculum by splitting each of the two hippocampal structures in half along its proximodistal axis. Of all voxels encompassing CA1, the half located distally was included, and of all the voxels encompassing subiculum, the half located proximally was included: these two halves thus make up what we here define and refer to as 'distal CA1/proximal subiculum' (dCA1pSub). To create RSC and OFC ROIs, respectively, the FreeSurfer parcellations named "isthmus cingulate" and "lateral orbitofrontal" were used as a starting point. The final RSC ROI was obtained by tailoring the isthmus cingulate and removing the excess superior areas, while the final OFC ROI was obtained by extracting the posterolateral quadrant of the lateral orbitofrontal area. All resulting ROIs are shown in Supplementary Figures 1-5. The ROIs were registered to the participants' individual spaces by applying the calculated transformations from ANTs. To increase the anatomical precision of the ROIs, the registered ROIs were then masked by respective participant-specific FreeSurfer parcellations.

2.3 DTI analysis

All DTI analyses were performed in the participant's native diffusion space. Voxel-wise fiber orientation distribution functions (fODFs) were computed by running the FSL function *bedpostx* on the diffusion data, using the zeppelin deconvolution model, a Rician noise model, and burn-in period 3000 (Sotiropoulos et al., 2016). Probabilistic tractography between the EC and presubiculum, dCA1pSub, RSC and OFC ROIs was then performed by running FSL's *probtrackx2* on the fODFs (Behrens et al., 2007; Behrens et al., 2003b). Tractography was performed both in ROI-by-ROI and voxel-by-ROI connectivity mode, with number of samples 250,000, minimal path length 5 mm, and a midline termination mask (Behrens et al., 2003a; Ezra et al., 2015; Johansen-Berg et al., 2004; Máté et al., 2018; Saygin et al., 2011). For tractography between EC and presubiculum, paths were excluded if they reached the dCA1pSub ROI, while for tractography between EC and dCA1pSub, paths were excluded if they reached the presubiculum ROI – and equivalently for tractography

between EC and RSC/OFC. For both *bedpostx* and *probtrackx2*, parameters were run with default values unless otherwise specified. ROI-by-ROI connectivity mode provides probability maps of the connectivity paths between the ROIs, while voxel-by-ROI connectivity mode provides probability maps of the voxel-wise connectivity of the EC ROI with the other ROIs, respectively. All tractography results were registered to MNI space and further analyses were performed there to facilitate inter-participant comparisons.

2.4 MEC and LEC segmentation

The voxel-wise connectivity maps were normalized to [0,1] by dividing them by the maximum probability for each hemisphere separately, and then thresholded by 0.01 to reduce false positive connections (Behrens et al., 2003a; Saygin et al., 2011). This threshold was determined empirically by testing a range of thresholds and choosing the one that in most cases removed connections outside the grey matter, because due to remaining distortions in the DTI images some of the EC ROIs slightly extended into air voxels. Crucially, we then define the MEC as the region that is most strongly connected with the presubiculum and/or RSC, while the LEC is the region that is most strongly connected with dCA1pSub and/or OFC (Caballero-Bleda and Witter, 1993; Honda and Ishizuka, 2004; Hoover and Vertes, 2007; Jones and Witter, 2007; Kondo and Witter, 2014; Saleem et al., 2008; Witter and Amaral, 1991; Witter and Amaral, 2021; Wyss and Van Groen, 1992). For each participant, a hard segmentation was performed on the normalized and thresholded voxel-wise connectivity maps using FSL's *find_the_biggest* (Behrens et al., 2003a; Johansen-Berg et al., 2004), where the voxels that had a stronger connection probability with the presubiculum/RSC than with dCA1pSub/OFC were classified as MEC, and vice versa for LEC.

2.5 Group analysis

Group probability maps of the connectivity paths between the ROIs, as well as group probability maps of voxel-wise connectivity, were created by summing and averaging all the individual maps. Inter-participant segmentation variability maps were created by adding together all the individual participants' MEC and LEC segmentations, respectively. Group MEC and LEC segmentation were performed similarly to the individual segmentation: The group voxel-wise connectivity maps were first smoothed with a Gaussian kernel of 1 mm and thresholded by 0.01, and then a hard segmentation was performed equivalently to the single-participant segmentation by comparing the connection probabilities of EC with presubiculum/RSC vs. dCA1pSub/OFC. Four different segmentations were performed with all the 2×2 combinations of seed regions, in addition to a combined segmentation approach

where the connectivity maps for presubiculum + RSC and for dCA1pSub + OFC, respectively, were combined and averaged before segmentation.

2.6 Segmentation comparisons

To assess the different segmentation approaches and compare the resulting locations of MEC and LEC, we calculated the orientation of the MEC-LEC border along the posterior-anterior (PA) and medial-lateral (ML) axes, respectively. This was performed by first calculating the centers of gravity of the differently defined MECs and LECs, and the vector between these centers of gravity. Next, the angle between this vector and a pure PA or ML vector was determined. We defined the PA axis as the long axis of the hippocampus. The degree of PA- or ML-oriented border was then defined between 0 and 100% such that an angle of 0° to the PA or ML vector means that the border is 100% oriented along the PA or ML vector, respectively. Correspondingly, an angle of 90° would mean that the border is 0% oriented along the respective axis, i.e. it is orthogonal to that axis. In addition, the different segmentations were compared with respect to the sizes of the resulting MECs and LECs, and the size ratios between these were calculated. All these segmentation comparisons were also carried out on the two fMRI-based segmentations of pmEC and alEC available for download from earlier studies (Maass et al., 2015; Navarro Schröder et al., 2015).

3 Results

To visualize the connectivity paths between the EC and the regions hypothesized to be connected with its subregions, we ran probabilistic tractography between the regions. By seeding paths from all voxels in the EC, presubiculum, dCA1pSub, RSC and OFC ROIs, maps of the connectivity paths between the EC and the other ROIs were created. The resulting group averaged paths are shown in Figure 1. In all figures, blue color schemes are used for MEC-related regions, i.e. presubiculum and RSC, while red color schemes are used for LEC-related regions, i.e. dCA1pSub and OFC. The maps show that all the regions exhibit clear connectivity with the EC. Connections with dCA1pSub extend further anteriorly in the EC than the connections with the presubiculum, and the connections with presubiculum and RSC seem to take a similar route to the EC. The paths between OFC and EC, however, stand out from the others as they take a more lateral route, but the inferior part seems to pass close to dCA1pSub. Note that the colormap intensity in these maps does not represent the actual number of white matter tracts, but instead scales with the probability that the true path between the ROIs lies in that point. Corresponding connectivity paths for one example participant are shown in Supplementary Figure 6.

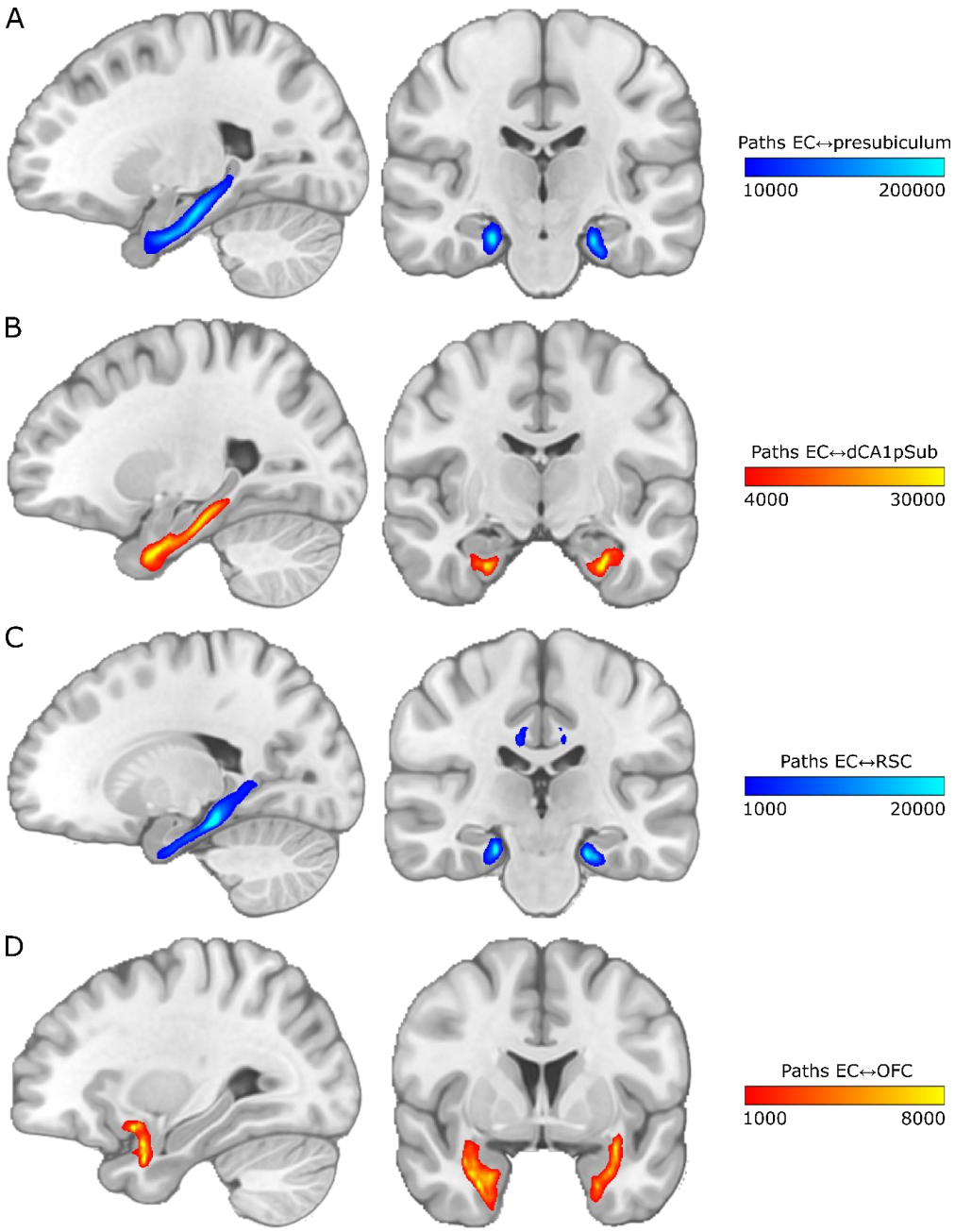

Figure 1: Group average connectivity paths between EC and presubiculum, dCA1pSub, RSC and OFC. *Connectivity patterns are shown on sagittal (left) and coronal (right) slices in MNI space. The colormap intensity represents the number of probabilistic paths running through that voxel.* ***A:*** *Paths between EC and presubiculum,* ***B:*** *Paths between EC and dCA1pSub,* ***C:*** *Paths between EC and RSC,* ***D:*** *Paths between EC and OFC.*

Because we wanted to segment the EC into the MEC and LEC homologues based on the connectivity with other regions, a voxel-by-voxel measure of connectivity probability was needed. We therefore also ran the tractography only seeding from the EC ROIs. Then, for each voxel in the ROI, we counted how many of the seeded paths reached the other ROIs. These connectivity counts were normalized to a probability, providing connectivity maps for the EC with the other four ROIs. The resulting smoothed and thresholded group averaged connectivity maps are shown in Figure 2. The sagittal slices show that the connectivity with presubiculum and RSC appears to be strongest in the posterior part of the EC, whereas the connectivity with dCA1pSub and OFC is strongest anteriorly in the EC. Further, the presubiculum connectivity does not show a clear medial-lateral gradient, but the connections with dCA1pSub, RSC and OFC are stronger laterally in the EC in the selected coronal slices. Corresponding connectivity maps for one example participant are shown in Supplementary Figure 7.

For segmentation into the MEC and LEC homologues, the main hypothesis was that these regions could be identified based on connectivity with presubiculum vs. dCA1pSub, respectively. The actual segmentation was performed on a voxel-by-voxel level in the EC determining with which of the other two regions the connection probability was highest, using the connectivity maps described in the previous paragraph. For comparison, the MEC-LEC segmentation was also performed based on connectivity with RSC vs. OFC, respectively. This was first performed individually for all participants, and inter-participant segmentation variability maps for the presubiculum vs. dCA1pSub and RSC vs. OFC segmentation approaches are shown in Figure 3. For most participants, MEC is clearly located more posteriorly and LEC is located more anteriorly for both segmentation approaches, and in addition they are located more medially and laterally with respect to each other for the presubiculum vs. dCA1pSub approach. The RSC vs. OFC approach also shows this medial-lateral trend of MEC and LEC across participants, although not as clear as for presubiculum vs. dCA1pSub. Corresponding MEC and LEC segmentations for one example participant are shown in Supplementary Figure 8.

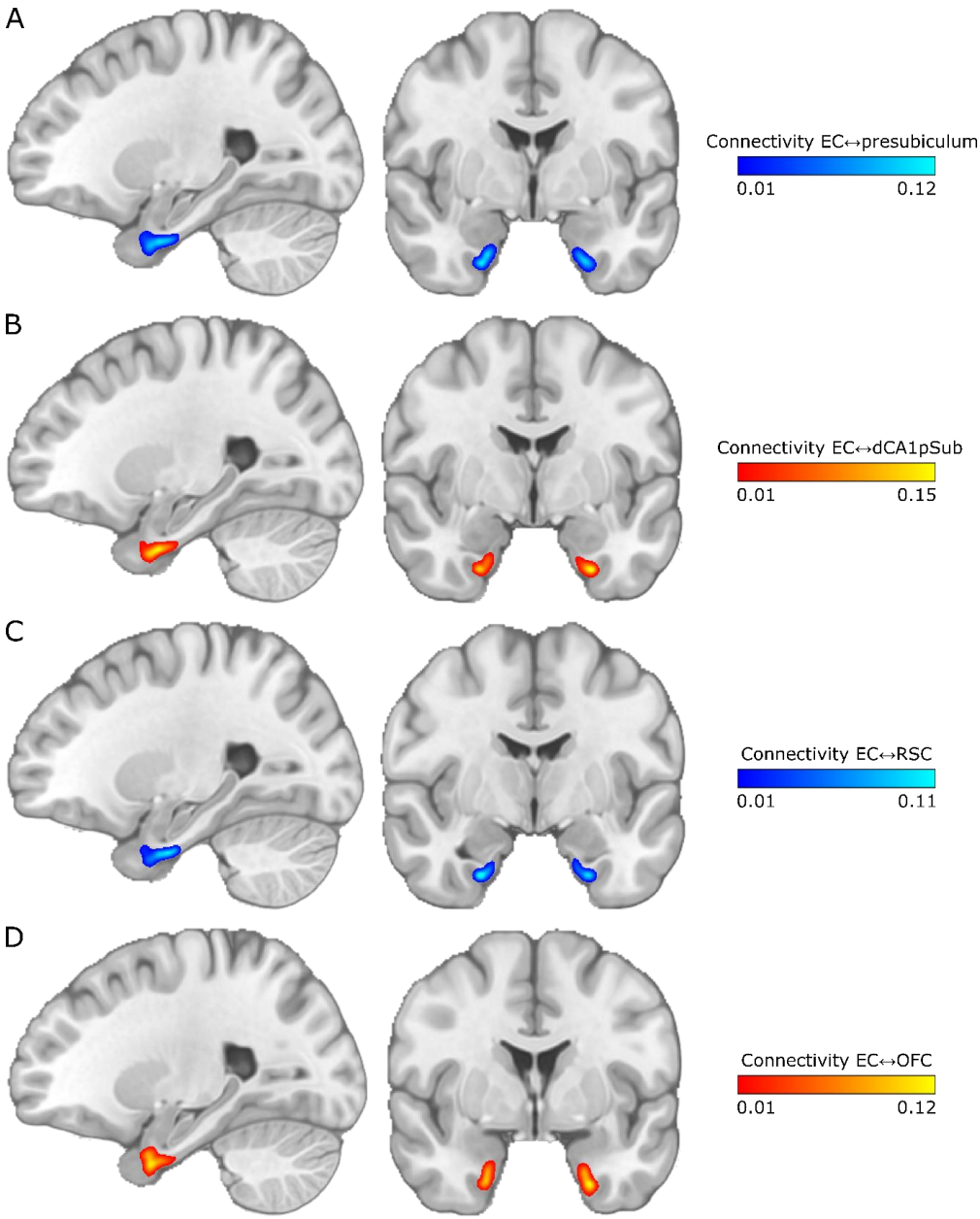

Figure 2: Group average maps of EC connectivity with presubiculum, dCA1pSub, RSC and OFC. *The maps are shown on sagittal (left) and coronal (right) slices in MNI space. The colormap intensity represents the fraction of paths seeded from that EC voxel that reached the other ROI.* ***A:*** *EC connectivity with presubiculum,* ***B:*** *EC connectivity with dCA1pSub,* ***C:*** *EC connectivity with RSC,* ***D:*** *EC connectivity with OFC.*

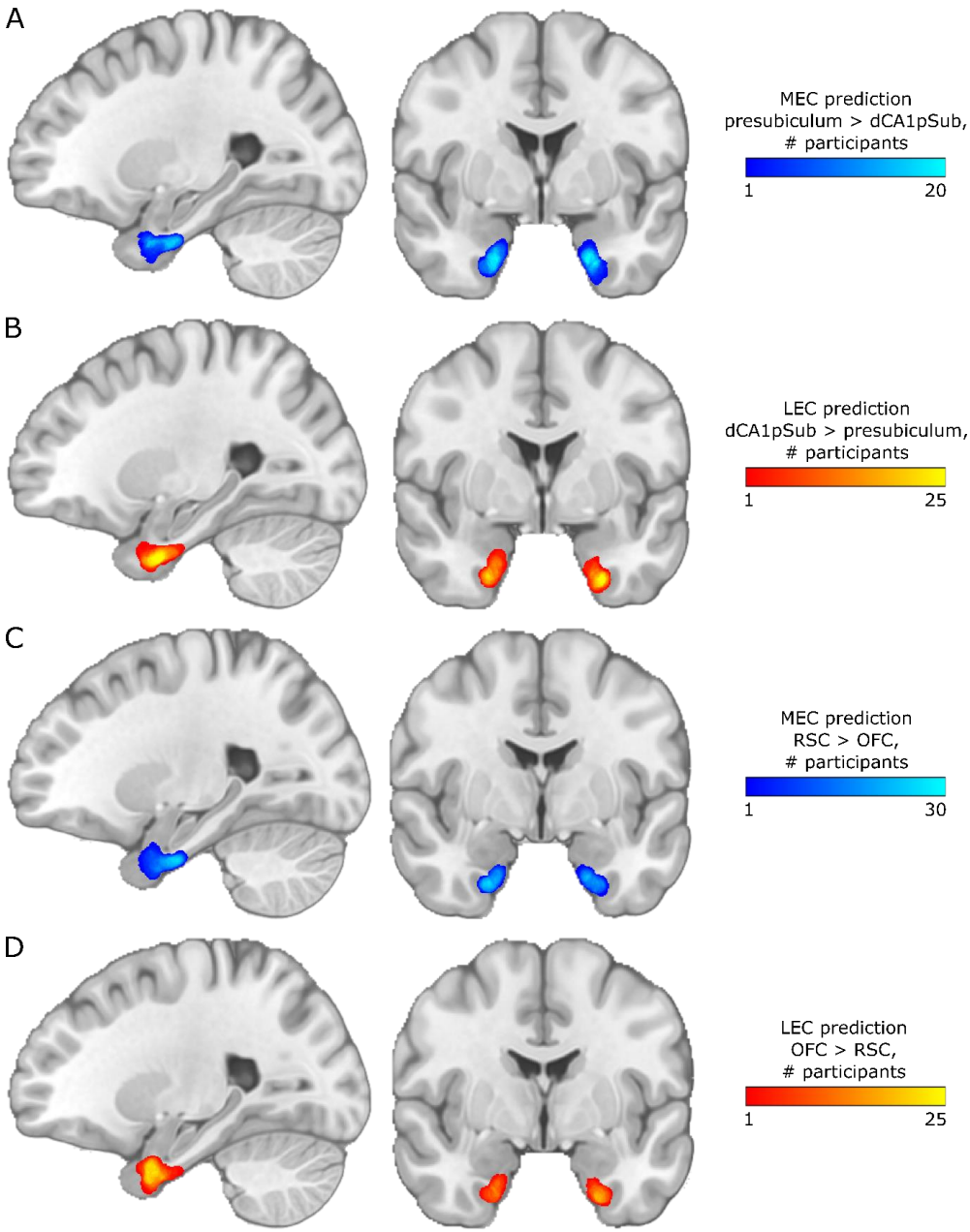

Figure 3: Inter-participant segmentation variability maps for different segmentation approaches. *Results are shown on sagittal (left) and coronal (right) slices in MNI space. The colormap intensities represents the number of participants for which that voxel was classified as MEC or LEC, respectively.* ***A:*** *MEC prediction based on higher connectivity with presubiculum than with dCA1pSub,* ***B:*** *LEC prediction based higher connectivity with dCA1pSub than with presubiculum,* ***C:*** *MEC prediction based on higher connectivity with RSC than with OFC,* ***D:*** *LEC prediction based on higher connectivity with OFC than with RSC.*

The same connectivity-based MEC-LEC segmentation was performed on a group level using the group averaged connectivity maps from Figure 2. As described above, the group segmentation was also performed using two different approaches – presubiculum vs. dCA1pSub, and RSC vs. OFC – and the resulting segmentations are shown in Figure 4. We see that for the MEC and LEC predictions from presubiculum vs. dCA1pSub, there is a clear medial-lateral (ML) and posterior-anterior (PA)-oriented border between the subregions. For RSC vs. OFC, however, the PA-oriented border is most prominent, but it is also slightly ML-oriented, most visible in the left EC. Because the results from the two approaches were slightly different, we also tried to interchange the ROI combinations, and MEC and LEC segmentations from using presubiculum vs. OFC and RSC vs. dCA1pSub can be seen in Supplementary Figure 9. Furthermore, to include all the information from the 2×2 combinations of seed regions into one final segmentation, we performed another approach where we averaged the connectivity maps for presubiculum and RSC, and the maps for dCA1pSub and OFC (Figure 5A and B). Figure 5C shows the resulting MEC and LEC homologues from this combined segmentation approach. With this approach, as with separate combinations of seed regions, we find both a PA- and ML-oriented (although most visible in the left hemisphere) border between MEC and LEC. These final MEC and LEC masks are also available in the Supplementary files.

In a next step, since the borders of the segmentations from different approaches showed slightly different orientations along the posterior-anterior (PA) and medial-lateral (ML) axes, we wanted to quantify this directional difference by calculating the “degree” of PA- and ML-orientation of the borders. This was defined as a percentage from 0 to 100%, dependent on the angle between the MEC-LEC center of gravity vector and a pure PA or ML vector. Table 1 shows the resulting degrees of PA- vs. ML- oriented borders for the different segmentation approaches including the fMRI segmentations from previous studies (Maass et al., 2015; Navarro Schröder et al., 2015). The center of gravity vectors are also plotted in a common reference frame in Supplementary Figure 10. All DTI segmentation approaches have a border with a PA-orientation of around 50-60%, and a varying degree of ML-orientation from 6% for RSC vs. OFC up to 67% for presubiculum vs. dCA1pSub. The borders between the segmentations from fMRI have a high PA-orientation of around 92%, and a lower degree of ML-orientation than all of the DTI approaches. Interestingly, when comparing the different combinations of DTI approaches, using dCA1pSub as the defining region for LEC yields a higher degree of ML-orientation than using OFC. Similarly, using RSC as the defining region for MEC yields a slightly higher degree of PA-orientation of the border than using presubiculum, but this is less prominent.

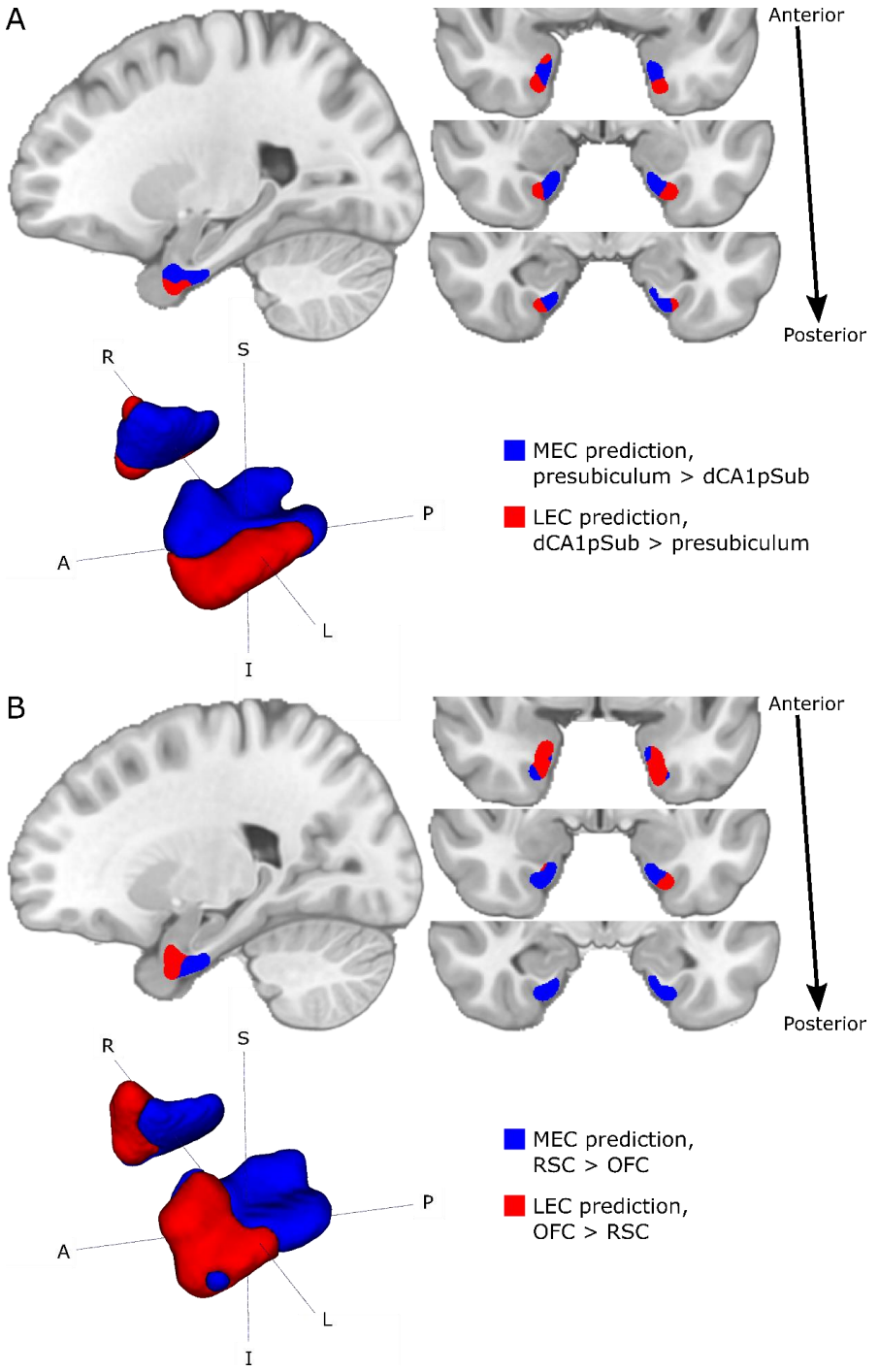

Figure 4: Group segmentations of MEC and LEC from different approaches. *Results are shown on sagittal (top left) and coronal (top right) slices and 3D-rendered (bottom left) in MNI space. The MEC and LEC predictions are shown in blue and red, respectively.* ***A:*** *MEC and LEC prediction based on connectivity with presubiculum vs. dCA1pSub,* ***B:*** *MEC and LEC prediction based on connectivity with RSC vs. OFC. S = superior, I = inferior, A = anterior, P = posterior, R = right, L = left.*

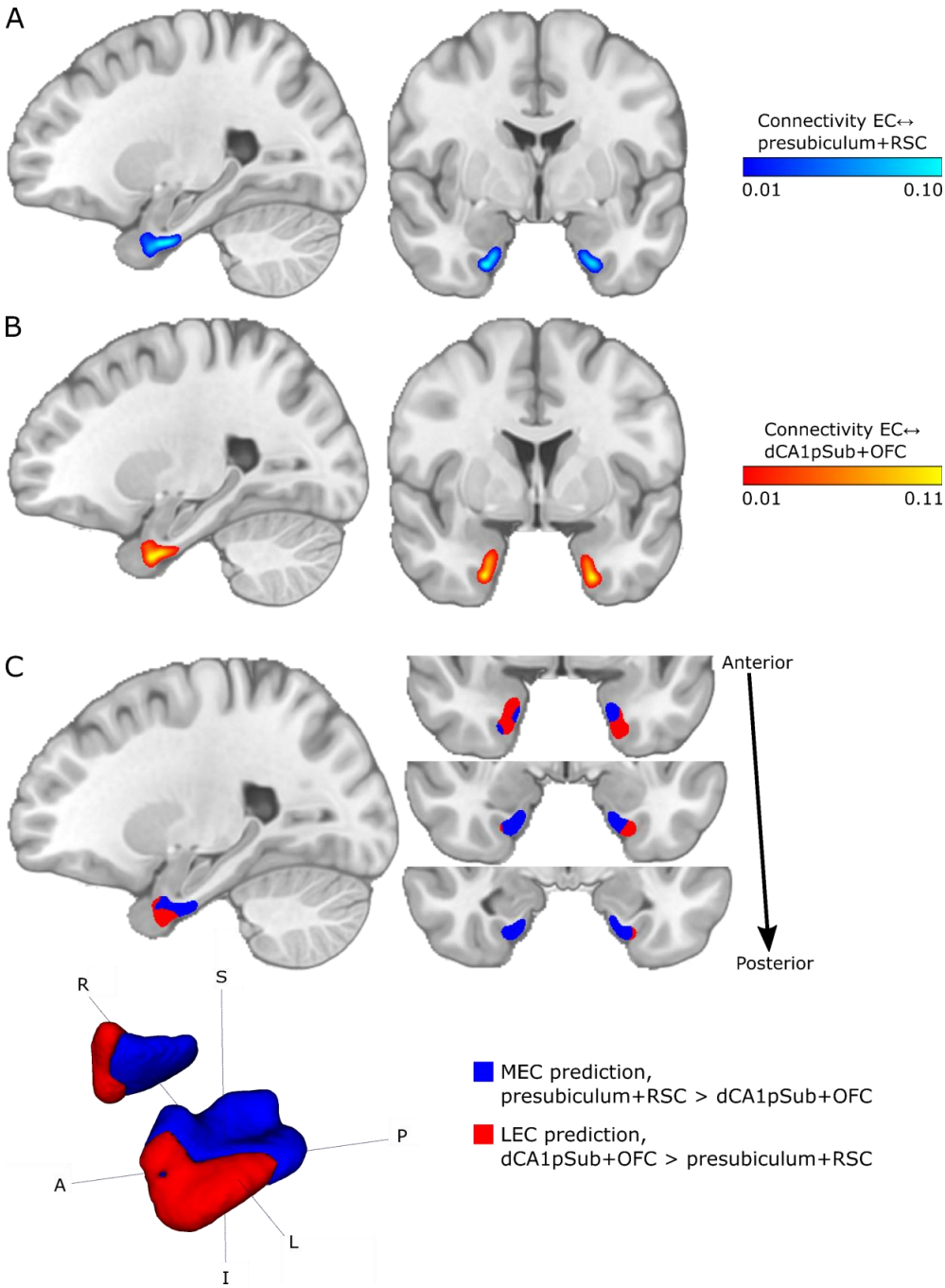

Figure 5: Group connectivity maps and segmentation using a combined approach with presubiculum + RSC vs. dCA1pSub + OFC. ***A:*** *EC connectivity with presubiculum + RSC combined.* ***B:*** *EC connectivity with dCA1pSub + OFC combined.* ***C:*** *MEC and LEC prediction based on connectivity with presubiculum + RSC vs. dCA1pSub + OFC combined.*

Table 1: Degree of posterior-anterior (PA) or medial-lateral (ML)-orientation of the border between MEC and LEC for different segmentation approaches*. The degree of PA- or ML-orientation is given as a percentage between 0 and 100%, dependent on the angle between the MEC-LEC center of gravity vector and the pure PA or ML vector, respectively. All numbers are given as the mean of both hemispheres ± mean absolute deviation.*

Segmentation approach		Posterior-anterior (PA) axis		Medial-lateral (ML) axis	
		Angle (°)	% PA	Angle (°)	% ML
DTI	Presubiculum/dCA1pSub	45.1 ± 3.0	49.9 ± 3.3	29.8 ± 1.9	66.9 ± 2.1
	RSC/OFC	39.7 ± 15.3	55.9 ± 17.0	84.5 ± 11.1	6.1 ± 12.3
	Presubiculum/OFC	41.3 ± 17.3	54.1 ± 19.3	81.2 ± 10.3	9.8 ± 11.5
	RSC/dCA1pSub	33.9 ± 1.2	62.3 ± 1.3	64.9 ± 18.8	27.9 ± 20.9
	Presubiculum+RSC/dCA1pSub+OFC	37.5 ± 10.6	58.3 ± 11.8	73.1 ± 17.4	18.7 ± 19.3
fMRI	Navarro Schröder et al.	6.8 ± 1.8	92.4 ± 2.0	85.5 ± 0.7	5.0 ± 0.8
	Maass et al.	6.6 ± 0.5	92.7 ± 0.6	87.9 ± 0.9	2.4 ± 1.0

Finally, we wanted to compare the resulting sizes of the MEC and LEC homologues from all the different segmentation approaches, and these are shown in Table 2. For all DTI approaches, the MEC is larger than LEC, while fMRI on the other hand yields a larger LEC than MEC. The subregions are most equally sized when using the RSC vs. dCA1pSub approach.

Table 2: Resulting sizes of MEC and LEC for different segmentation approaches, and the size ratio between MEC and LEC. *The numbers of voxels are given for the ROIs in MNI space with 0.5 mm isotropic resolution.*

Segmentation approach		Size (# voxels)		MEC/LEC size ratio
		MEC	LEC	
DTI	Presubiculum/dCA1pSub	12759	7763	1.64
	RSC/OFC	12971	8727	1.49
	Presubiculum/OFC	13614	6979	1.95
	RSC/dCA1pSub	11045	10282	1.07
	Presubiculum+RSC/dCA1pSub+OFC	13571	7379	1.84
fMRI	Navarro Schröder et al.	12802	16028	0.80
	Maass et al.	3776	11008	0.34

4 Discussion

In this study, we used DTI and probabilistic tractography in 35 healthy adults to segment the human EC into homologues of what in other mammals have been functionally and cytoarchitectonically defined as MEC and LEC. We based the segmentation on EC connectivity with four brain regions known to selectively project to either of the EC subregions in multiple species. Different combinations of these four regions all showed both

a posterior-anterior (PA) and a medial-lateral (ML)-oriented border between the human homologues of MEC and LEC. This orientation of the thus defined border is similar to that defined in previous fMRI studies resulting in the definition of the two subregions as pmEC and alEC (Maass et al., 2015; Navarro Schröder et al., 2015). Note however that our DTI results show a larger degree of ML-orientation, and a correspondingly lower degree of PA-orientation of the border between the subregions compared to the previous fMRI results.

The results from our study substantiate the pmEC and alEC subdivision of the human EC suggested in previous fMRI studies (Maass et al., 2015; Navarro Schröder et al., 2015). Although some earlier fMRI studies on mnemonic processing in the EC found a dissociation primarily along the medial-lateral axis (Reagh and Yassa, 2014; Schultz et al., 2012), it is important to realize that even the orientation of the cytoarchitectonically defined border between MEC and LEC in rodents does not align along a pure medial-to-lateral axis. Rather, the MEC in rodents is actually located in the posterior-medial EC, and the LEC is located in the anterior-lateral EC (van Strien et al., 2009). Also, in macaque monkeys, tracing studies show differential connectivity in caudal vs. rostral portions (Witter and Amaral, 2021). A pure medial-lateral subdivision of human EC is thus not to be expected. Nevertheless, the somewhat different orientations of the border between the human homologues of MEC vs. LEC subdivisions found using DTI vs. fMRI studies raises the question of which of the two imaging modalities should be preferred to define the position and orientation of this border.

There are several possible explanations as to why our DTI study showed slightly different segmentation results than the fMRI studies. First, DTI and fMRI are two different imaging modalities with inherently different mechanisms of connectivity. While DTI exploits the diffusion of water molecules in order to trace the structural paths of connectivity between brain regions (Mori et al., 1999; Mori and Zhang, 2006; Powell et al., 2004; Zeineh et al., 2012), fMRI identifies functional connectivity by correlating blood-oxygen-level-dependent (BOLD) signals across time (Van Dijk et al., 2010). Although structural and functional connectivity in theory should be closely linked, they are in reality quantitatively difficult to compare because of the complexity of the connectivity mechanisms of the brain (Huang and Ding, 2016; Messé et al., 2015). Another reason for the different results between this and the previous studies could be the use of different seed regions to identify the MEC and LEC homologues. While we used presubiculum and RSC to define MEC, and dCA1pSub and OFC to define LEC (Caballero-Bleda and Witter, 1993; Honda and Ishizuka, 2004; Hoover and Vertes, 2007; Jones and Witter, 2007; Kondo and Witter, 2014; Saleem et al., 2008; Witter and Amaral, 1991; Witter and Amaral, 2021; Wyss and Van Groen, 1992), one of the fMRI studies investigated differential connectivity of PHC vs. PRC and distal vs. proximal subiculum (Maass et al., 2015), whereas the other used regions in a posterior-medial vs. an

anterior-temporal cortical system (Navarro Schröder et al., 2015). The new insights from rodent anatomy indicate that while PHC area TH is connected with the MEC, PHC area TF is connected with the LEC (Witter and Amaral, 2021). As area TF is located more laterally than TH, this might in part explain why the previous fMRI study where they used connectivity with the whole PHC to define the pmEC (Maass et al., 2015) showed a lower medial-lateral component of their pmEC-alEC segmentation than our results. In order to determine to which extent each of these reasons contributed to the different subdivision results across studies, both imaging modalities and different seed regions should be investigated more rigorously in one single, larger cohort of participants.

Interestingly, using different seed regions to identify MEC and LEC resulted in varying degrees of PA- and ML-orientation of the border between them. It is unclear whether this is inherently linked to the DTI method, or due to an actual connectivity difference between the regions. Using presubiculum and dCA1pSub as the seed regions, which are situated medially and laterally with respect to each other, respectively, resulted in a border with higher degree of ML- than PA-orientation. On the other hand, using RSC and OFC, which are situated posteriorly and anteriorly in the brain, respectively, resulted in a border with higher degree of PA- than ML-orientation. Although it is not unnatural to assume that the brain is organized such that connected regions are situated more closely to each other, this could also be an effect of using probabilistic tractography, where the apparent connectivity probability depends on e.g. the length of the path and the size of the ROIs (Behrens et al., 2007). In other species, including rodents and monkeys, the presubiculum and RSC show inputs to the EC with a similar spatial distribution (Witter and Amaral, 2021), aligning with our maps of connectivity paths with these two seed regions. However, comparing the different MEC and LEC segmentations from the different seed region combinations shows that while interchanging presubiculum and RSC yields only slightly different orientation of the border along the PA and ML axes, the difference when interchanging dCA1pSub and OFC is more substantial. In other species, dCA1pSub are known to project to both rostral and dorsolateral parts of EC, whereas posterolateral OFC mainly projects dorsolaterally in the EC (Kondo and Witter, 2014; Saleem et al., 2008; Witter and Amaral, 1991; Witter and Amaral, 2021). Whether these regions in humans project to different parts of the homologue of LEC, or whether our results are affected by using DTI and probabilistic tractography, should be further investigated by also comparing EC functional connectivity to these areas using fMRI. Note also that the topography of projections from dCA1pSub along the medial-lateral axis of the EC depends on where the seed is placed along the posterior-anterior axis of the dCA1pSub (Witter and Amaral, 2021), which emphasizes the importance of carefully defined seed ROIs.

In order to determine and compare the connectivities between the EC and the other ROIs, we normalized the connectivity maps by dividing them by the maximum probability of each map. This could introduce a bias in the results. By doing this, we intrinsically assume that the maximum connectivity strength to each of the other ROIs are equal, and the segmentation process does not take into account that the MEC connections might be stronger than the LEC connections, or vice versa. However, little is known about the strength of connectivities at this level of detail, particularly since it is not straightforward to examine or even define connectivity strength. Connectivity strength surely depends on axonal density, but other factors like synaptic density and efficacy are other important variables. Nevertheless, even if we were to know that some of the connections are stronger than the others, probabilistic tractography provides a relative instead of an absolute measure of connectivity and is also dependent on path lengths, ROI sizes and the number of possible path directions in a voxel. Normalizing the connectivity maps based on different connectivity strengths would therefore be a highly complex task. Therefore, we did not impose any further assumptions about connectivity strengths in our analyses.

Our study has some limitations. To define our ROIs, we chose to use regions from automatic cortical segmentation protocols. This could have influenced the anatomical precision of our analysis. Manual segmentation would be labor-intensive and requires high skills in neuroanatomy, possibly limiting the number of participants that could be included in the study. However, we manually adjusted some of the automatically segmented ROIs, and also intersected the registered ROIs from MNI space with the participants' individual automatic segmentations in order to increase the anatomical accuracy. Another limitation is that there are inherent challenges to the EPI sequence used for diffusion imaging. This results in a generally low signal-to-noise ratio in the EC and the whole medial temporal lobe. In addition, these regions appear geometrically distorted in the EPI images, and although this has been corrected for, it is not possible to recover all of the lost signal. Imperfect correction can also affect the accuracy of the ROIs. Because of the probabilistic nature of the tractography technique it is unlikely that noise will introduce false connections, but it can leave some connections undetected. At last, a relatively low number of participants were included in our study, which might have influenced the statistical power of the results.

5 Conclusions

Our DTI results support the definition of pmEC and alEC as the human homologues of MEC and LEC. Also inspired by novel insights coming from rodent anatomy, we present a segmentation based on a combination of differential presubiculum/RSC and dCA1pSub/OFC structural connectivity which indicates a border between the two subdivisions of EC with an

orientation that is angled both towards the posterior-anterior axis, as well as to the medial-lateral axis. The fact that there are some differences in the orientation of the border based on DTI and fMRI data in addition to the seed regions used, indicates the need for investigation in a larger number of participants across both modalities.

Acknowledgements

This study was supported by the Norwegian University of Science and Technology.

Data were provided by the Human Connectome Project, MGH-USC Consortium (Principal Investigators: Bruce R. Rosen, Arthur W. Toga and Van Wedeen; U01MH093765) funded by the NIH Blueprint Initiative for Neuroscience Research grant; the National Institutes of Health grant P41EB015896; and the Instrumentation Grants S10RR023043, 1S10RR023401, 1S10RR019307.

Competing interests

The authors declare no competing interests.

Supplementary files

- MEC and LEC homologue masks in MNI152-09b space, defined from the combined presubiculum+RSC vs. dCA1pSub+OFC approach (MEC_LEC_segmentations.zip).

References

Amunts, K., Mohlberg, H., Bludau, S., Zilles, K., 2020. Julich-Brain: A 3D probabilistic atlas of the human brain's cytoarchitecture. Science 369, 988-992. doi:10.1126/science.abb4588

Avants, B.B., Tustison, N.J., Song, G., Cook, P.A., Klein, A., Gee, J.C., 2011. A reproducible evaluation of ANTs similarity metric performance in brain image registration. Neuroimage 54, 2033-2044. doi:10.1016/j.neuroimage.2010.09.025

Behrens, T.E., Johansen-Berg, H., Jbabdi, S., Rushworth, M.F., Woolrich, M.W., 2007. Probabilistic diffusion tractography with multiple fibre orientations: What can we gain? Neuroimage 34, 144-155. doi:10.1016/j.neuroimage.2006.09.018

Behrens, T.E., Johansen-Berg, H., Woolrich, M.W., Smith, S.M., Wheeler-Kingshott, C.A., Boulby, P.A., Barker, G.J., Sillery, E.L., Sheehan, K., Ciccarelli, O., Thompson, A.J., Brady, J.M., Matthews, P.M., 2003a. Non-invasive mapping of connections between human thalamus and cortex using diffusion imaging. Nature Neuroscience 6, 750-757. doi:10.1038/nn1075

Behrens, T.E., Woolrich, M.W., Jenkinson, M., Johansen-Berg, H., Nunes, R.G., Clare, S., Matthews, P.M., Brady, J.M., Smith, S.M., 2003b. Characterization and propagation of uncertainty in diffusion-weighted MR imaging. Magnetic Resonance in Medicine 50, 1077-1088. doi:10.1002/mrm.10609

Bellmund, J.L., Deuker, L., Doeller, C.F., 2019. Mapping sequence structure in the human lateral entorhinal cortex. eLife 8. doi:10.7554/eLife.45333

Braak, H., Braak, E., 1992. The human entorhinal cortex: normal morphology and lamina-specific pathology in various diseases. Neuroscience Research 15, 6-31. doi:10.1016/0168-0102(92)90014-4

Buzsáki, G., 1996. The Hippocampo-Neocortical Dialogue. Cerebral Cortex 6, 81-92. doi:10.1093/cercor/6.2.81

Caballero-Bleda, M., Witter, M.P., 1993. Regional and laminar organization of projections from the presubiculum and parasubiculum to the entorhinal cortex: an anterograde tracing study in the rat. Journal of Comparative Neurology 328, 115-129. doi:10.1002/cne.903280109

Canto, C.B., Wouterlood, F.G., Witter, M.P., 2008. What Does the Anatomical Organization of the Entorhinal Cortex Tell Us? Neural Plasticity 2008, 381243. doi:10.1155/2008/381243

Chen, X., Vieweg, P., Wolbers, T., 2019. Computing distance information from landmarks and self-motion cues - Differential contributions of anterior-lateral vs. posterior-medial entorhinal cortex in humans. Neuroimage 202, 116074. doi:10.1016/j.neuroimage.2019.116074

Deshmukh, S.S., Knierim, J.J., 2011. Representation of non-spatial and spatial information in the lateral entorhinal cortex. Frontiers in Behavioral Neuroscience 5, 69. doi:10.3389/fnbeh.2011.00069

Doan, T.P., Lagartos-Donate, M.J., Nilssen, E.S., Ohara, S., Witter, M.P., 2019. Convergent Projections from Perirhinal and Postrhinal Cortices Suggest a Multisensory Nature of Lateral, but Not Medial, Entorhinal Cortex. Cell Reports 29, 617-627.e617. doi:10.1016/j.celrep.2019.09.005

Doeller, C.F., Barry, C., Burgess, N., 2010. Evidence for grid cells in a human memory network. Nature 463, 657-661. doi:10.1038/nature08704

Eichenbaum, H., Yonelinas, A.P., Ranganath, C., 2007. The Medial Temporal Lobe and Recognition Memory. Annual Review of Neuroscience 30, 123-152. doi:10.1146/annurev.neuro.30.051606.094328

Ezra, M., Faull, O.K., Jbabdi, S., Pattinson, K.T., 2015. Connectivity-based segmentation of the periaqueductal gray matter in human with brainstem optimized diffusion MRI. Human Brain Mapping 36, 3459-3471. doi:10.1002/hbm.22855

Fan, Q., Nummenmaa, A., Witzel, T., Zanzonico, R., Keil, B., Cauley, S., Polimeni, J.R., Tisdall, D., Van Dijk, K.R., Buckner, R.L., Wedeen, V.J., Rosen, B.R., Wald, L.L., 2014. Investigating the capability to resolve complex white matter structures with high b-value diffusion magnetic resonance imaging on the MGH-USC Connectom scanner. Brain Connectivity 4, 718-726. doi:10.1089/brain.2014.0305

Fan, Q., Witzel, T., Nummenmaa, A., Van Dijk, K.R.A., Van Horn, J.D., Drews, M.K., Somerville, L.H., Sheridan, M.A., Santillana, R.M., Snyder, J., Hedden, T., Shaw, E.E., Hollinshead, M.O., Renvall, V., Zanzonico, R., Keil, B., Cauley, S., Polimeni, J.R., Tisdall, D., Buckner, R.L., Wedeen, V.J., Wald, L.L., Toga, A.W., Rosen, B.R., 2016. MGH-USC Human Connectome Project datasets with ultra-high b-value diffusion MRI. Neuroimage 124, 1108-1114. doi:10.1016/j.neuroimage.2015.08.075

Fischl, B., Salat, D.H., Busa, E., Albert, M., Dieterich, M., Haselgrove, C., van der Kouwe, A., Killiany, R., Kennedy, D., Klaveness, S., Montillo, A., Makris, N., Rosen, B., Dale, A.M., 2002. Whole brain segmentation: automated labeling of neuroanatomical structures in the human brain. Neuron 33, 341-355. doi:10.1016/s0896-6273(02)00569-x

Fischl, B., van der Kouwe, A., Destrieux, C., Halgren, E., Ségonne, F., Salat, D.H., Busa, E., Seidman, L.J., Goldstein, J., Kennedy, D., Caviness, V., Makris, N., Rosen, B., Dale, A.M., 2004. Automatically parcellating the human cerebral cortex. Cerebral Cortex 14, 11-22. doi:10.1093/cercor/bhg087

Fonov, V.S., Evans, A.C., McKinstry, R.C., Almli, C.R., Collins, D.L., 2009. Unbiased nonlinear average age-appropriate brain templates from birth to adulthood. Neuroimage 47, S102. doi:10.1016/S1053-8119(09)70884-5

Fyhn, M., Molden, S., Witter, M.P., Moser, E.I., Moser, M.-B., 2004. Spatial Representation in the Entorhinal Cortex. Science 305, 1258-1264. doi:10.1126/science.1099901

Hafting, T., Fyhn, M., Molden, S., Moser, M.B., Moser, E.I., 2005. Microstructure of a spatial map in the entorhinal cortex. Nature 436, 801-806. doi:10.1038/nature03721

Honda, Y., Ishizuka, N., 2004. Organization of connectivity of the rat presubiculum: I. Efferent projections to the medial entorhinal cortex. Journal of Comparative Neurology 473, 463-484. doi:10.1002/cne.20093

Hoover, W.B., Vertes, R.P., 2007. Anatomical analysis of afferent projections to the medial prefrontal cortex in the rat. Brain Structure & Function 212, 149-179. doi:10.1007/s00429-007-0150-4

Huang, C.-C., Rolls, E.T., Hsu, C.-C.H., Feng, J., Lin, C.-P., 2021. Extensive Cortical Connectivity of the Human Hippocampal Memory System: Beyond the “What” and “Where” Dual Stream Model. Cerebral Cortex. doi:10.1093/cercor/bhab113

Huang, H., Ding, M., 2016. Linking Functional Connectivity and Structural Connectivity Quantitatively: A Comparison of Methods. Brain Connectivity 6, 99-108. doi:10.1089/brain.2015.0382

Høydal, Ø.A., Skytøen, E.R., Andersson, S.O., Moser, M.B., Moser, E.I., 2019. Object-vector coding in the medial entorhinal cortex. Nature 568, 400-404. doi:10.1038/s41586-019-1077-7

Iglesias, J.E., Augustinack, J.C., Nguyen, K., Player, C.M., Player, A., Wright, M., Roy, N., Frosch, M.P., McKee, A.C., Wald, L.L., Fischl, B., Van Leemput, K., 2015. A computational atlas of the hippocampal formation using ex vivo, ultra-high resolution MRI: Application to adaptive segmentation of in vivo MRI. Neuroimage 115, 117-137. doi:10.1016/j.neuroimage.2015.04.042

Jenkinson, M., Beckmann, C.F., Behrens, T.E., Woolrich, M.W., Smith, S.M., 2012. FSL. Neuroimage 62, 782-790. doi:10.1016/j.neuroimage.2011.09.015

Johansen-Berg, H., Behrens, T.E., Robson, M.D., Drobnjak, I., Rushworth, M.F., Brady, J.M., Smith, S.M., Higham, D.J., Matthews, P.M., 2004. Changes in connectivity profiles define functionally distinct regions in human medial frontal cortex. Proceedings of the National Academy of Sciences of the United States of America 101, 13335-13340. doi:10.1073/pnas.0403743101

Jones, B.F., Witter, M.P., 2007. Cingulate cortex projections to the parahippocampal region and hippocampal formation in the rat. Hippocampus 17, 957-976. doi:10.1002/hipo.20330

Kerr, K.M., Agster, K.L., Furtak, S.C., Burwell, R.D., 2007. Functional neuroanatomy of the parahippocampal region: The lateral and medial entorhinal areas. Hippocampus 17, 697-708. doi:10.1002/hipo.20315

Knierim, J.J., Neunuebel, J.P., Deshmukh, S.S., 2014. Functional correlates of the lateral and medial entorhinal cortex: objects, path integration and local-global reference frames. Philosophical Transactions of the Royal Society of London. Series B: Biological Sciences 369, 20130369. doi:10.1098/rstb.2013.0369

Kondo, H., Witter, M.P., 2014. Topographic organization of orbitofrontal projections to the parahippocampal region in rats. Journal of Comparative Neurology 522, 772-793. doi:10.1002/cne.23442

Lavenex, P., Amaral, D.G., 2000. Hippocampal-neocortical interaction: A hierarchy of associativity. Hippocampus 10, 420-430. doi:10.1002/1098-1063(2000)10:4<420::Aid-hipo8>3.0.Co;2-5

Máté, A., Kis, D., Czigner, A., Fischer, T., Halász, L., Barzó, P., 2018. Connectivity-based segmentation of the brainstem by probabilistic tractography. Brain Research 1690, 74-88. doi:10.1016/j.brainres.2018.03.010

McNab, J.A., Edlow, B.L., Witzel, T., Huang, S.Y., Bhat, H., Heberlein, K., Feiweier, T., Liu, K., Keil, B., Cohen-Adad, J., Tisdall, M.D., Folkerth, R.D., Kinney, H.C., Wald, L.L., 2013. The Human Connectome Project and beyond: initial applications of 300 mT/m gradients. Neuroimage 80, 234-245. doi:10.1016/j.neuroimage.2013.05.074

Messé, A., Benali, H., Marrelec, G., 2015. Relating structural and functional connectivity in MRI: a simple model for a complex brain. IEEE Transactions on Medical Imaging 34, 27-37. doi:10.1109/tmi.2014.2341732

Montchal, M.E., Reagh, Z.M., Yassa, M.A., 2019. Precise temporal memories are supported by the lateral entorhinal cortex in humans. Nature Neuroscience 22, 284-288. doi:10.1038/s41593-018-0303-1

Mori, S., Crain, B.J., Chacko, V.P., van Zijl, P.C., 1999. Three-dimensional tracking of axonal projections in the brain by magnetic resonance imaging. Annals of Neurology 45, 265-269. doi:10.1002/1531-8249(199902)45:2<265::aid-ana21>3.0.co;2-3

Mori, S., Zhang, J., 2006. Principles of diffusion tensor imaging and its applications to basic neuroscience research. Neuron 51, 527-539. doi:10.1016/j.neuron.2006.08.012

Moser, Edvard I., Moser, M.-B., 2013. Grid Cells and Neural Coding in High-End Cortices. Neuron 80, 765-774. doi:10.1016/j.neuron.2013.09.043

Maass, A., Berron, D., Libby, L.A., Ranganath, C., Düzel, E., 2015. Functional subregions of the human entorhinal cortex. eLife 4, e06426. doi:10.7554/eLife.06426

Navarro Schröder, T., Haak, K.V., Zaragoza Jimenez, N.I., Beckmann, C.F., Doeller, C.F., 2015. Functional topography of the human entorhinal cortex. eLife 4, e06738. doi:10.7554/eLife.06738

Nilssen, E.S., Doan, T.P., Nigro, M.J., Ohara, S., Witter, M.P., 2019. Neurons and networks in the entorhinal cortex: A reappraisal of the lateral and medial entorhinal subdivisions mediating parallel cortical pathways. Hippocampus 29, 1238-1254. doi:10.1002/hipo.23145

Powell, H.W., Guye, M., Parker, G.J., Symms, M.R., Boulby, P., Koepp, M.J., Barker, G.J., Duncan, J.S., 2004. Noninvasive in vivo demonstration of the connections of the human parahippocampal gyrus. Neuroimage 22, 740-747. doi:10.1016/j.neuroimage.2004.01.011

Ranganath, C., Ritchey, M., 2012. Two cortical systems for memory-guided behaviour. Nature Reviews: Neuroscience 13, 713-726. doi:10.1038/nrn3338

Reagh, Z.M., Yassa, M.A., 2014. Object and spatial mnemonic interference differentially engage lateral and medial entorhinal cortex in humans. Proceedings of the National Academy of Sciences 111, E4264-E4273. doi:10.1073/pnas.1411250111

Saleem, K.S., Kondo, H., Price, J.L., 2008. Complementary circuits connecting the orbital and medial prefrontal networks with the temporal, insular, and opercular cortex in the macaque monkey. Journal of Comparative Neurology 506, 659-693. doi:10.1002/cne.21577

Saygin, Z.M., Osher, D.E., Augustinack, J., Fischl, B., Gabrieli, J.D., 2011. Connectivity-based segmentation of human amygdala nuclei using probabilistic tractography. Neuroimage 56, 1353-1361. doi:10.1016/j.neuroimage.2011.03.006

Schultz, H., Sommer, T., Peters, J., 2012. Direct Evidence for Domain-Sensitive Functional Subregions in Human Entorhinal Cortex. The Journal of Neuroscience 32, 4716-4723. doi:10.1523/jneurosci.5126-11.2012

Setsompop, K., Kimmlingen, R., Eberlein, E., Witzel, T., Cohen-Adad, J., McNab, J.A., Keil, B., Tisdall, M.D., Hoecht, P., Dietz, P., Cauley, S.F., Tountcheva, V., Matschl, V., Lenz, V.H., Heberlein, K., Potthast, A., Thein, H., Van Horn, J., Toga, A., Schmitt, F., Lehne, D., Rosen, B.R., Wedeen, V., Wald, L.L., 2013. Pushing the limits of in vivo diffusion MRI for the Human Connectome Project. Neuroimage 80, 220-233. doi:10.1016/j.neuroimage.2013.05.078

Smith, S.M., 2002. Fast robust automated brain extraction. Human Brain Mapping 17, 143-155. doi:10.1002/hbm.10062

Sotiropoulos, S.N., Hernández-Fernández, M., Vu, A.T., Andersson, J.L., Moeller, S., Yacoub, E., Lenglet, C., Ugurbil, K., Behrens, T.E.J., Jbabdi, S., 2016. Fusion in diffusion

MRI for improved fibre orientation estimation: An application to the 3T and 7T data of the Human Connectome Project. Neuroimage 134, 396-409. doi:10.1016/j.neuroimage.2016.04.014

Suzuki, W.A., Eichenbaum, H., 2000. The Neurophysiology of Memory. Annals of the New York Academy of Sciences 911, 175-191. doi:10.1111/j.1749-6632.2000.tb06726.x

Tsao, A., Moser, M.B., Moser, E.I., 2013. Traces of experience in the lateral entorhinal cortex. Current Biology 23, 399-405. doi:10.1016/j.cub.2013.01.036

Tsao, A., Sugar, J., Lu, L., Wang, C., Knierim, J.J., Moser, M.-B., Moser, E.I., 2018. Integrating time from experience in the lateral entorhinal cortex. Nature 561, 57-62. doi:10.1038/s41586-018-0459-6

Van Dijk, K.R., Hedden, T., Venkataraman, A., Evans, K.C., Lazar, S.W., Buckner, R.L., 2010. Intrinsic functional connectivity as a tool for human connectomics: theory, properties, and optimization. Journal of Neurophysiology 103, 297-321. doi:10.1152/jn.00783.2009

van Strien, N.M., Cappaert, N.L.M., Witter, M.P., 2009. The anatomy of memory: an interactive overview of the parahippocampal–hippocampal network. Nature Reviews Neuroscience 10, 272-282. doi:10.1038/nrn2614

Witter, M.P., Amaral, D.G., 1991. Entorhinal cortex of the monkey: V. Projections to the dentate gyrus, hippocampus, and subicular complex. Journal of Comparative Neurology 307, 437-459. doi:10.1002/cne.903070308

Witter, M.P., Amaral, D.G., 2021. The entorhinal cortex of the monkey: VI. Organization of projections from the hippocampus, subiculum, presubiculum, and parasubiculum. Journal of Comparative Neurology 529, 828-852. doi:10.1002/cne.24983

Witter, M.P., Doan, T.P., Jacobsen, B., Nilssen, E.S., Ohara, S., 2017. Architecture of the Entorhinal Cortex A Review of Entorhinal Anatomy in Rodents with Some Comparative Notes. Frontiers in Systems Neuroscience 11. doi:10.3389/fnsys.2017.00046

Wyss, J.M., Van Groen, T., 1992. Connections between the retrosplenial cortex and the hippocampal formation in the rat: a review. Hippocampus 2, 1-11. doi:10.1002/hipo.450020102

Zeineh, M.M., Holdsworth, S., Skare, S., Atlas, S.W., Bammer, R., 2012. Ultra-high resolution diffusion tensor imaging of the microscopic pathways of the medial temporal lobe. Neuroimage 62, 2065-2082. doi:10.1016/j.neuroimage.2012.05.065

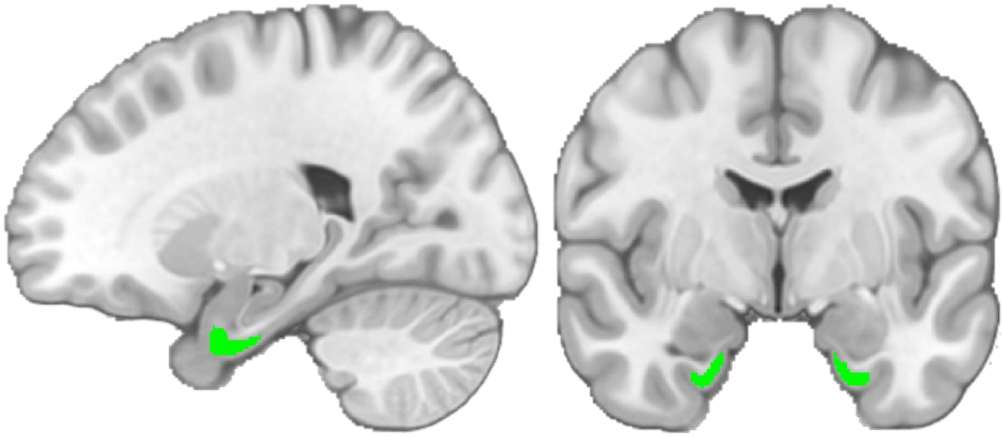

Supplementary Figure 1: EC ROI. *The ROI is shown in green on a sagittal (left) and a coronal (right) slice in MNI space.*

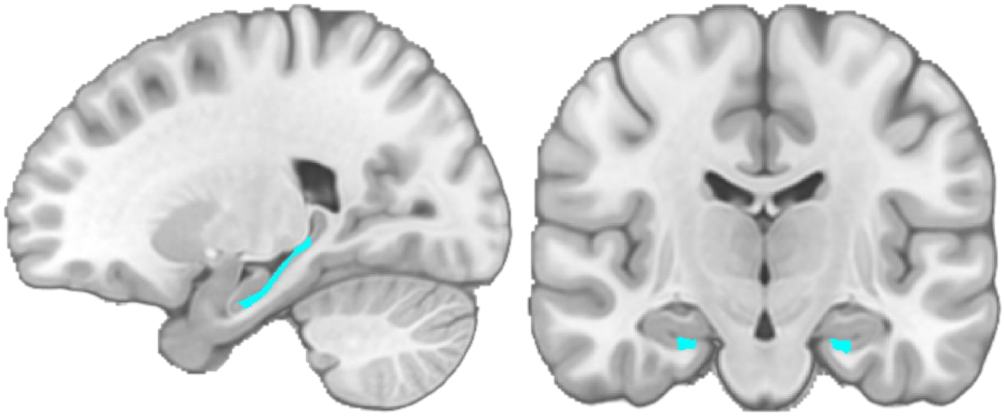

Supplementary Figure 2: Presubiculum ROI. *The ROI is shown in light blue on a sagittal (left) and a coronal (right) slice in MNI space.*

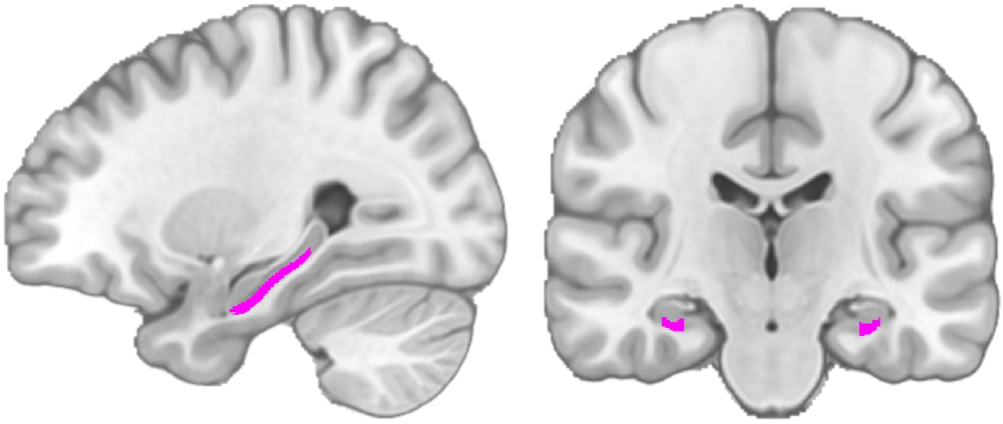

Supplementary Figure 3: dCA1pSub ROI. *The ROI is shown in pink on a sagittal (left) and a coronal (right) slice in MNI space.*

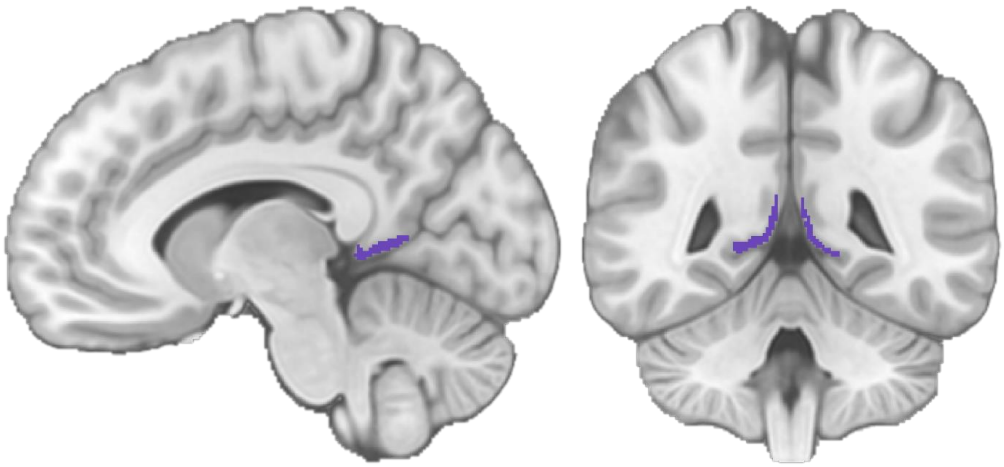

Supplementary Figure 4: RSC ROI. *The ROI is shown in purple on a sagittal (left) and a coronal (right) slice in MNI space.*

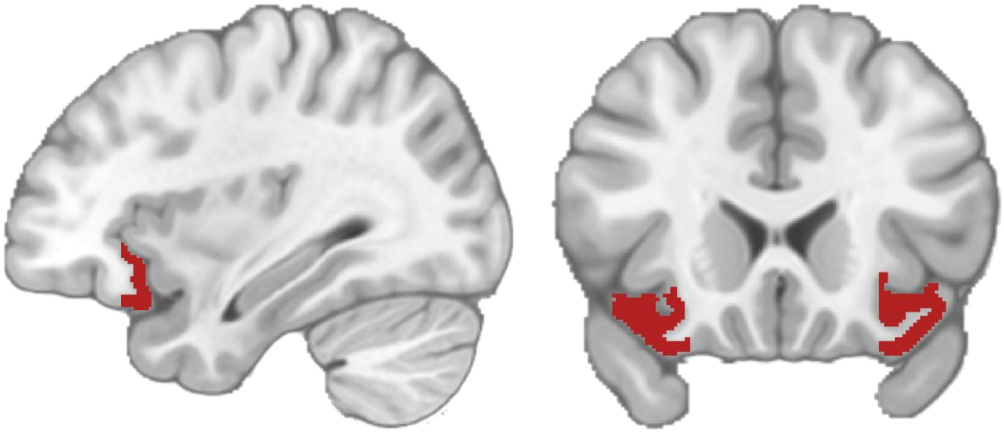

Supplementary Figure 5: OFC ROI. *The ROI is shown in dark red on a sagittal (left) and a coronal (right) slice in MNI space.*

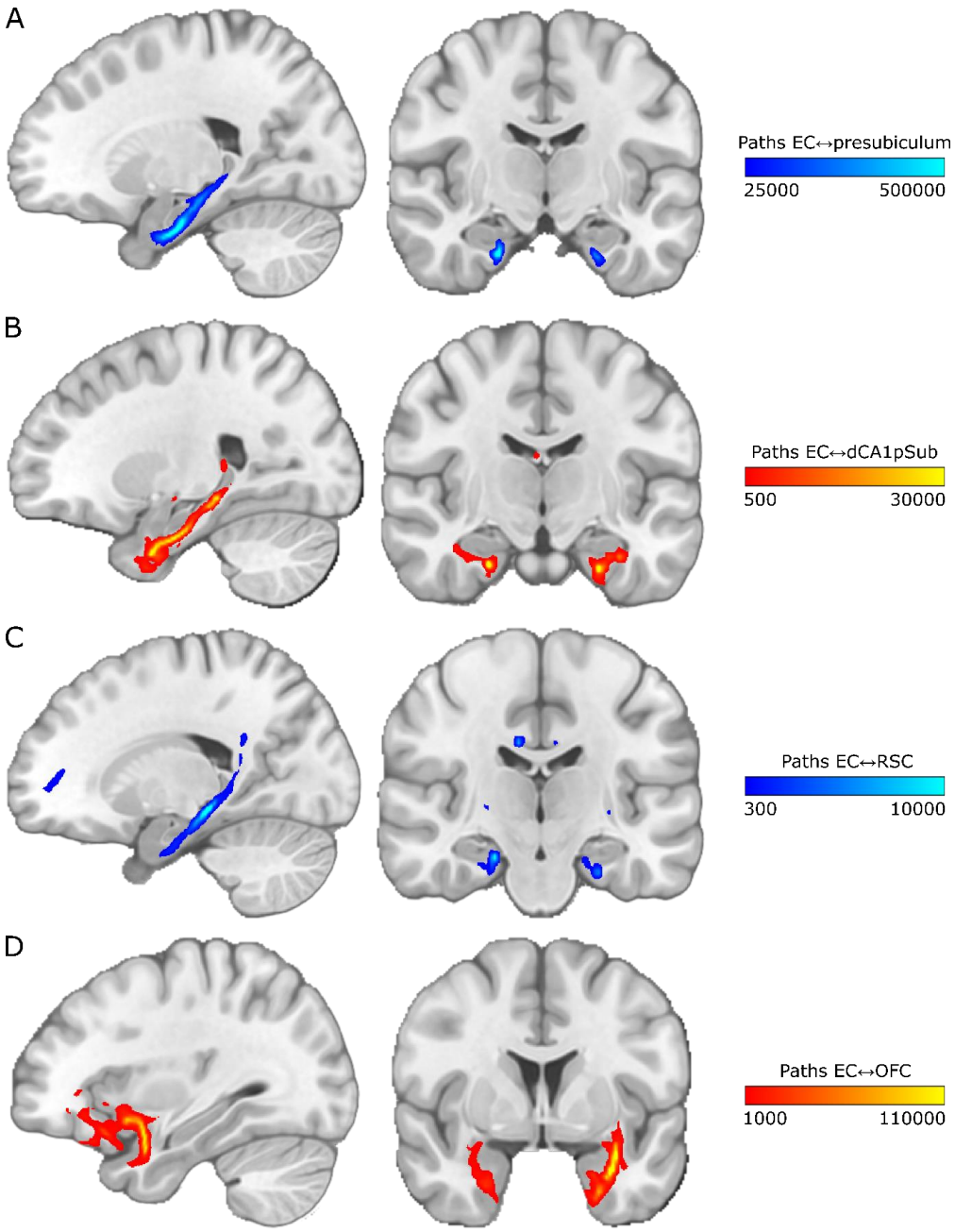

Supplementary Figure 6: Connectivity paths between EC and presubiculum, dCA1pSub, RSC and OFC for one example participant. *The paths are shown on sagittal (left) and coronal (right) slices in MNI space. The colormap intensity represents the number of probabilistic paths running through that voxel.* ***A:*** *Paths between EC and presubiculum,* ***B:*** *Paths between EC and dCA1pSub,* ***C:*** *Paths between EC and RSC,* ***D:*** *Paths between EC and OFC.*

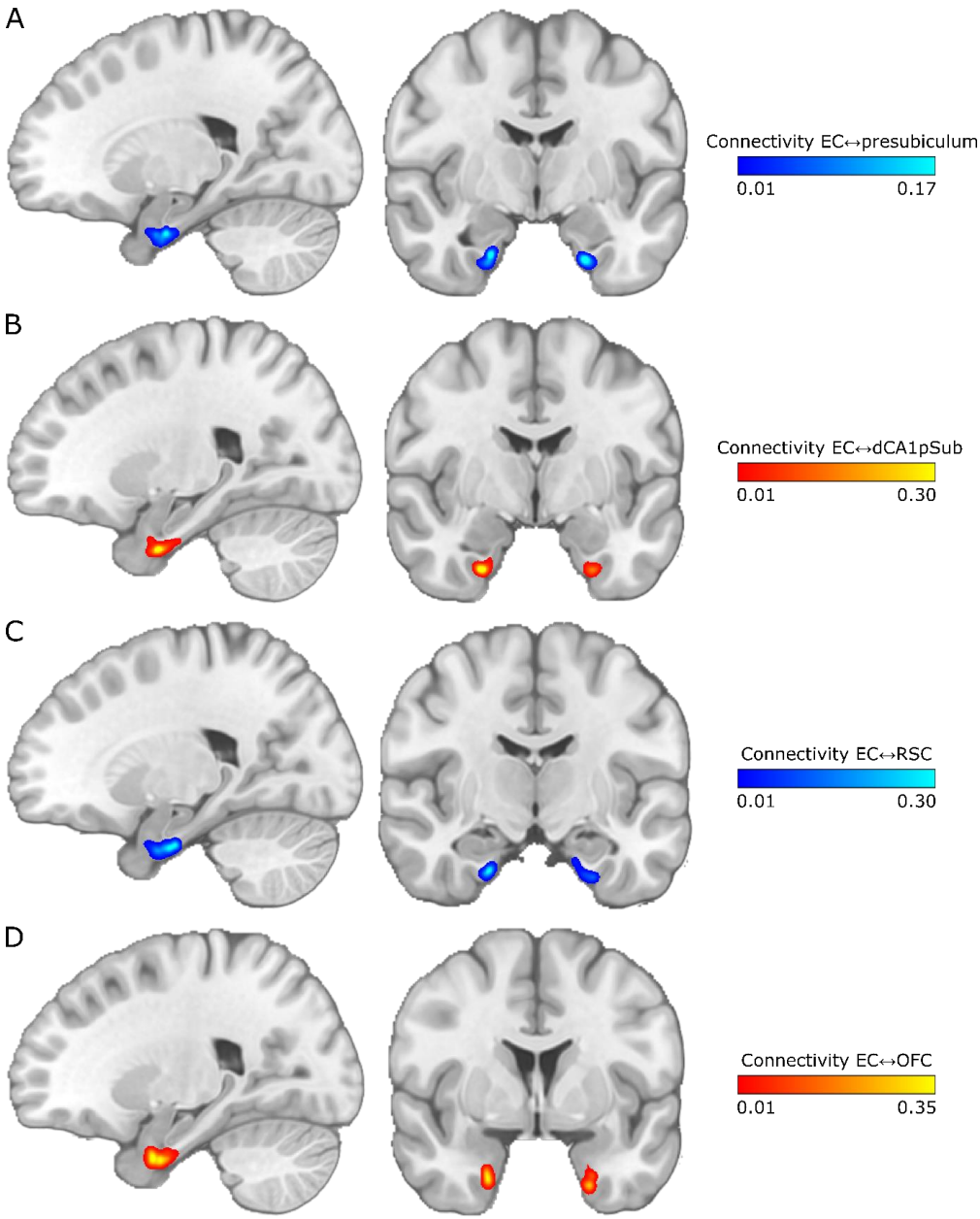

Supplementary Figure 7: Maps of EC connectivity with presubiculum, dCA1pSub, RSC and OFC for one example participant. *The maps are shown on sagittal (left) and coronal (right) slices in MNI space. The colormap intensity represents the fraction of paths seeded from that EC voxel that reached the other ROI.* ***A:*** *EC connectivity with presubiculum,* ***B:*** *EC connectivity with dCA1pSub,* ***C:*** *EC connectivity with RSC,* ***D:*** *EC connectivity with OFC.*

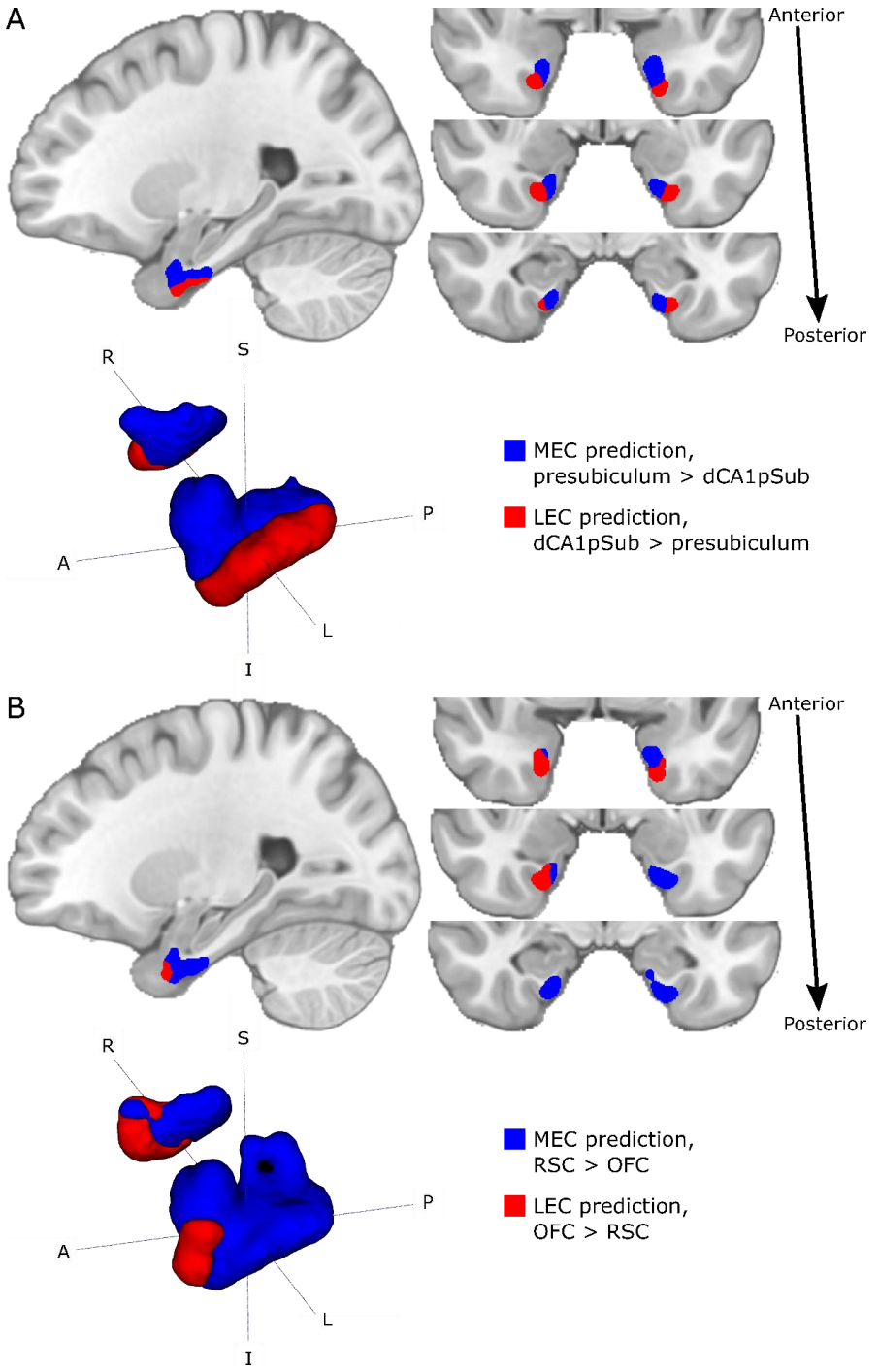

Supplementary Figure 8: Segmentations of MEC and LEC from different approaches for one example participant. *The results are shown on sagittal (top left) and coronal (top right) slices and 3D-rendered (bottom left) in MNI space. The MEC and LEC predictions are shown in blue and red, respectively.* ***A:*** *MEC and LEC prediction based on connectivity with presubiculum vs. dCA1pSub,* ***B:*** *MEC and LEC prediction based on connectivity with RSC vs. OFC. S = superior, I = inferior, A = anterior, P = posterior, R = right, L = left.*

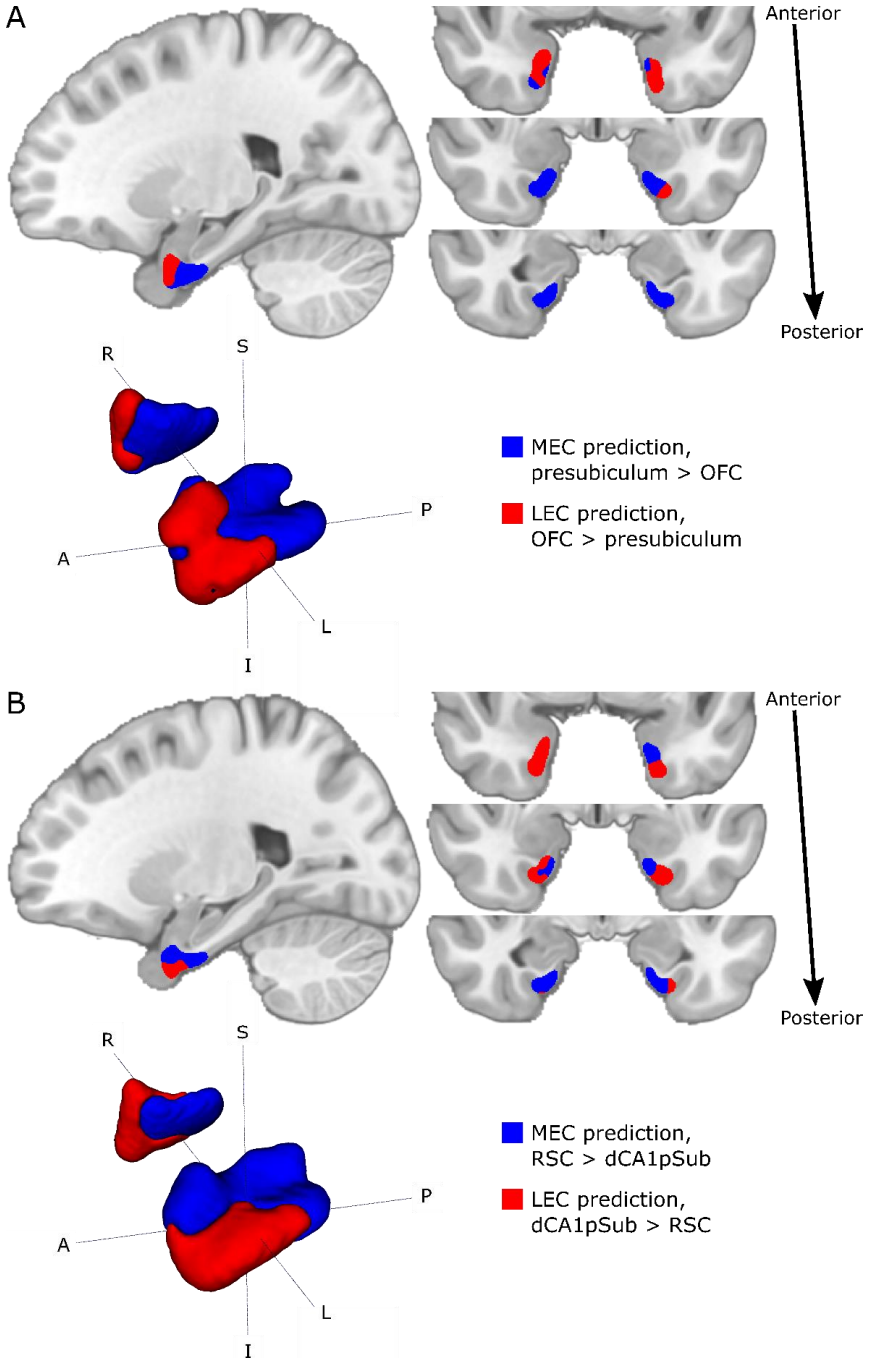

Supplementary Figure 9: Group segmentations of MEC and LEC from different approaches. *The results are shown on sagittal (top left) and coronal (top right) slices and 3D-rendered (bottom left) in MNI space. The MEC and LEC predictions are shown in blue and red, respectively.* ***A:*** *MEC and LEC prediction based on connectivity with presubiculum vs. OFC,* ***B:*** *MEC and LEC prediction based on connectivity with RSC vs. dCA1pSub. S = superior, I = inferior, A = anterior, P = posterior, R = right, L = left.*

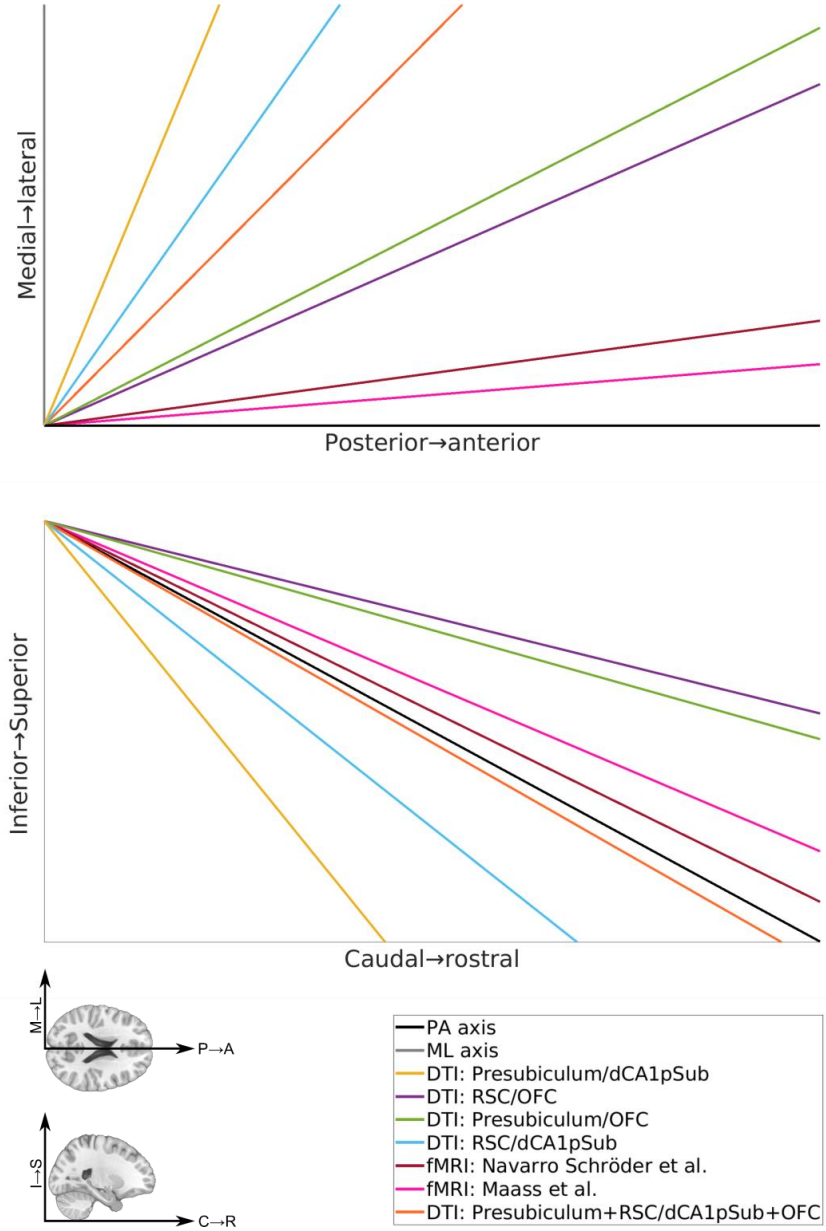

Supplementary Figure 10: Center of gravity vectors between MEC-LEC segmentations in the axial (top) and sagittal (bottom) planes, showing the angles between the orientation of the MEC-LEC border and the pure PA and ML axes in the left hemisphere. *The PA axis vector is shown in black, the ML axis vector is shown in grey (visible in the axial view only), and the colors of the MEC-LEC vectors for all the different segmentation approaches are explained in the legend box on the bottom right. On the bottom left, illustrations of the anatomical directions of the vector plots are shown (M = medial, L = lateral, P = posterior, A = anterior, I = inferior, S = superior, C = caudal, R = rostral). The posterior-anterior axis is defined along the long axis of the hippocampus in the sagittal plane. Note that the length of the vectors shown here does not correspond to the real distance between the MEC and LEC centers of gravity. The origin of the vectors corresponds to the MEC center of gravity, which are not the true MEC locations for the different segmentation approaches, but shifted in space so that all vectors originate in the same point.*

Paper III

This paper is awaiting publication and is not included in NTNU Open

ISBN 978-82-326-5507-6 (printed ver.)
ISBN 978-82-326-6923-3 (electronic ver.)
ISSN 1503-8181 (printed ver.)
ISSN 2703-8084 (online ver.)

NTNU
Norwegian University of
Science and Technology